Fracture mechanics investigation of interacting defects in composite materials

Fan Mu

2015

Fan Mu. (2015). Fracture mechanics investigation of interacting defects in composite materials. Doctoral thesis, Nanyang Technological University, Singapore.

https://hdl.handle.net/10356/65446

https://doi.org/10.32657/10356/65446

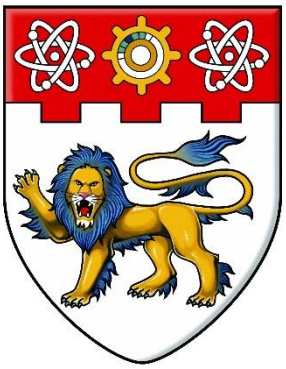

NANYANG TECHNOLOGICAL UNIVERSITY

FRACTURE MECHANICS INVESTIGATION OF INTERACTING DEFECTS IN COMPOSITE MATERIALS

FAN MU

SCHOOL OF MECHANICAL AND AEROSPACE ENGINEERING

2015

FRACTURE MECHANICS INVESTIGATION OF INTERACTING DEFECTS IN COMPOSITE MATERIALS

FAN MU

2015

FAN MU

FRACTURE MECHANICS INVESTIGATION OF INTERACTING DEFECTS IN COMPOSITE MATERIALS

FAN MU

SCHOOL OF MECHANICAL AND AEROSPACE ENGINEERING

A thesis submitted to the Nanyang Technological University in fulfillment of the requirements for the Degree of Doctor of Philosophy

Singapore

2015

Acknowledgements

I would like to express my deepest gratitude and appreciation to my supervisor, Dr. Xiao Zhongmin for his guidance, encouragement and patient assistance, without whom this work may never have been completed.

I would like to express my sincere gratitude to Dr. Yi Dake, my senior. His tremendous support and assistance especially in the early stage of this PhD study has guided the author to quickly and successfully get familiar with the research work of fracture mechanics.

Last but not least, I would like to thank my dearest parents, my wife and brother. Their support is the most important gift I have ever got in life and accompanies me every day and night. I would also like to thank those who have ever been together with me, studying and working during the past four years, without them my life could not be so wonderful.

Contents

List of Figures

List of Tables

List of Symbols

$\mu_i \left(i=1,2,3\right)$	Shear modulus of material number i
$\nu_i \left(i=1,2,3\right)$	Poison's ratio of material number i
$\kappa_i \left(i=1,2,3\right)$	Muskhelishvili material constant of material number i
$E_i \left(i=1,2,3\right)$	Young's modulus of material number i
$\lambda_i \left(i=1,2,3\right)$	Lame's constants of material number i
A, B, C, D, M, N	Bi-material constants
$\sigma_{ij}, \varepsilon_{ij}, \sigma_{ys}$	Stress and strain components, material yield stress
u	Displacement component
$\Phi\left(z\right), \Psi\left(z\right)$	Complex potential functions
K_I, K_{II}	Stress intensity factors (SIF)
r_y, r_p, δ	Plastic zone size and crack tip opening displacement
t_1, t_2, a_c	Left and right crack tips, half crack length
b_x, b_y	Glide and climb Burgers vectors
b_x^T, b_y^T	Total sum of Burgers vectors of Zener-Stroh crack
B_x, B_y	Glide and climb dislocation densities
r_0	Radius of inclusion for bi-material problem
a, b	Radius of phase 1 and phase 2 for three-material system
ξ	Distance from the dislocation to the core of the fiber
α, β	Dundurs' constants for bi-material system

Summary

With the increasing applications of composite materials in various engineering structures, failure analysis on crack induced fracture problems for composite materials has attracted more and more attention among researchers. Fracture behavior studies based on the linear elastic fracture mechanics theory are not accurate enough when yielding occurs around crack tips. In the current PhD study, with the plastic zone corrections, the elastic-plastic fracture behavior investigations on various crack problems in fiber-reinforced composite materials have been carried out.

The first physical problem solved is a curved interfacial crack along a circular inclusion/matrix interface. A curved area is proposed as plastic zone ahead each crack tip. In this case, both normal and shear stresses exist and are coupled, resulting in complicated fracture behaviors in the plastic zone area of the crack. For the first time we proposed a mixed model Dugdale model to estimate the plastic zone size and crack tip opening displacement for curved cracks. The problem on crack-coated inclusion interaction is then investigated with the introduction of plastic zones at both crack tips. Compared to the two-phase material structure, the coating phase can effectively reduce the material mismatches between the inclusion and matrix, reduce the stress concentration and increase the interface bonding. The influence of the coating phase parameters, such as the coating phase thickness and shear modulus, on the plastic zone size

and crack tip opening displacement are studied in detail.

Thereafter, the generalized Irwin plastic zone correction for the problem of a crack interacting with multiple inclusions is studied by using the three-phase cylindrical model. For the problem of multiple inclusions in fiber-reinforced composites, it is commonly understood that the stress and strain fields near the crack depend considerably on the microstructure around it. Hence, the three-phase model is proposed as a simplified model for the real multiple-inclusion composites: the crack and the nearest inclusion are embedded in their immediate surrounding pure matrix, while other inclusions and matrix are replaced by an equivalent homogeneous media (the composite material). It is different but more accurate than the two-phase model where a single inclusion is embedded in the infinitely extended pure matrix.

Two types of crack mechanisms are involved in the current work. The first one is the classical Griffith crack which is induced by external loading, and the total sum of Burger's vector within the crack equals to zero. The second is the Zener-Stroh crack induced by the pileup of dislocations, and the total Burger's vector within the crack is not equal to zero. The physical parameters that are symmetric for the Griffith crack are anti-symmetric for the Zener-Stroh crack and vice versa. For instance, a Griffith crack dislocation distribution along the crack plane is anti-symmetric and results in a symmetric crack plane traction stress. The Zener-Stroh crack has an anti-symmetric crack plane traction stress which

arises from a symmetric crack plane dislocation distribution. For a Zener-Stroh crack, the crack tip where the dislocations enter the crack is a blunt tip while the other tip is a sharp tip. The crack propagation always starts from the sharp tip. Hence, the fracture behavior in the plastic zone area for a Zener-Stroh crack could be quite different from that for a Griffith crack even under similar external conditions.

As the major contribution of the current thesis, two approaches of plastic zone correction are demonstrated in our study. The first one is the mixed-mode Dugdale model and the second one is the generalized Irwin model. The Dugdale model is suitable for all crack problems but the plastic zone size calculation is quite complex. The Irwin model is suitable for matrix cracking only (crack lies in the matrix material), as the plastic zone size and crack tip opening displacement for this model are based on the crack tip stress intensity factors directly. The introduction of plastic zone can greatly improve the accuracy of fracture prediction for fiber-reinforced composite materials with ductile matrix (such as metal matrix composites).

Chapter 1 Introduction

1.1. Background

Fibers-reinforced composites are composed of axial particulates embedded in a matrix material and has been increasingly used in various engineering structures. An appealing property of these composites is their high specific strength (strength per unit weight), which is credited to the reinforcing fibers (the inclusions) intentionally introduced into the matrix. However, the inclusions often cause stress concentration in their vicinities where cracks and dislocations may form, which has great effect on the application of the composite structures. One of such examples is shown in Fig. 1.1 [1], where a crack is initiated in the matrix and propagates among the inclusions of the composite.

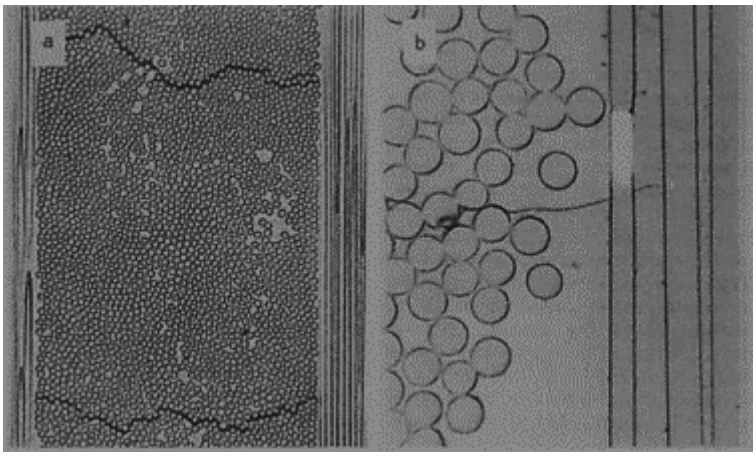

Fig. 1.1 A cross-plied FRP laminate, showing non-uniform fiber packing and micro-cracking.

Generally, two major patterns of crack in fibers-reinforced composites are inclusion/matrix debonding and matrix cracking, which can be induced under certain thermal or mechanical loading conditions. Attention has been taken for

years on how a crack (cracks) of various shapes propagates within varied fibers-reinforced composite (FRC) systems. Several applications of fracture mechanics of FRC include inclusion/matrix system (2-phase), coated-inclusion/matrix system (3-phase) and multiple inclusion/matrix system. To understand such inclusion/matrix debonding or matrix cracking problems more accurately, the interactions between the crack and the near-by inclusions (the fibers) should be considered.

Additionally, for failure analysis and prevention of engineering structures and materials, two basic forms of fracture failure should be considered: brittle and ductile fracture. Linear elastic stress analysis on sharp cracks predicts infinite stresses at the crack tips and works perfectly well in brittle materials. However, in ductile materials such as metal-matrix composite materials, plastic deformation leads to further relaxation of crack tip stresses and makes the elastic stress analysis less accurate. Plastic zone correction is thus required and important for fracture behavior analysis in ductile materials.

1.2. Objectives

The crack-inclusion interaction problems in FRC are simulated based on the distributed dislocation method in this work. Two different types of crack are looked into: the Griffith crack and the Zener-Stroh crack. The cracks may be formed by fiber-matrix debonding or matrix cracking. The elastic-plastic fracture behavior of the cracks is emphasized with the objectives of:

1. To understand the way how a pileup of dislocations form a crack (interface crack and matrix crack) in fibers-reinforced composite materials.
2. To develop a generalized approach to estimate the plastic zone size (PZS) and crack tip opening displacement (CTOD) for various crack problems, and to investigate the influence of material properties and crack geometry parameters on the fracture behavior of the crack.
3. To understand the physical mechanism of the mixed mode Dugdale model and the generalized Irwin model, and their advantages and limitations on plastic zone corrections in fiber-reinforced composite materials with cracks.

1.3. Overview

In the current work, a brief literature review is given in Chapter 2. The basic concepts of dislocation, modes of fracture, numerical solutions of singular integral equation with Cauchy kernel and the two models to predict the plastic deformation ahead crack tips are reviewed. The definitions of plastic zone size and crack tip opening displacement under different models are highlighted based on the type of crack.

Various physical problems with different configurations have been solved accordingly, which starts with an arc-shaped interface crack in Chapter 3. The stress field, stress intensity factor, plastic zone size and crack tip opening displacement are evaluated by a mixed-mode Dugdale model. After that, plastic zone corrections have been carried out for a matrix Griffith/Zener-Stroh crack

interacting with a coated circular inclusion based on the generalized Irwin model. This work is presented in Chapter 4 and 5 for the two types of crack respectively. Investigation on crack-inclusions interaction in three-phase composites with Irwin plastic zone correction is demonstrated in Chapter 6 for a Griffith crack by emphasizing the influence of fiber concentrations and other material parameters. A Zener-Stroh crack interacting with a nanosized inhomogeneity is investigated in Chapter 7 by considering the inhomogeneity size and interface effect. Conclusions have been made in Chapter 8 about the characteristics of each problem. Some topics of future work are recommended in this chapter as well.

Chapter 2 Literature Review

2.1. Dislocation

In fracture mechanics, the crack problems can be solved by viewing the crack as a continuous array of dislocations [2]. This method has been widely used to formulate plane crack problems between dissimilar materials [3-6]. In two dimensions, a dislocation is created by first making a slit in an infinite solid, from the core of the dislocation to any infinite point. The trajectory of that slit may take any form, and the dislocation is formed by imposing a constant displacement between adjacent points located at either side of the slit, by inserting or removing material as necessary, and then welding the material back together. This constant relative displacement imposed is known as Burgers vector [7-9]. There are two types of dislocations. For plane problems, we employ edge dislocations where the Burgers vector itself lies in the plane and the edge dislocations are used to model mode I or mode II crack loading; the second type is screw-type dislocation which can be used to model cracks subjected to mode III loading where the Burgers vector is in z-direction [10]. Dislocations found in actual materials are usually mixed. In our work, we mainly use edge dislocations for crack simulation.

2.1.1. Edge dislocation

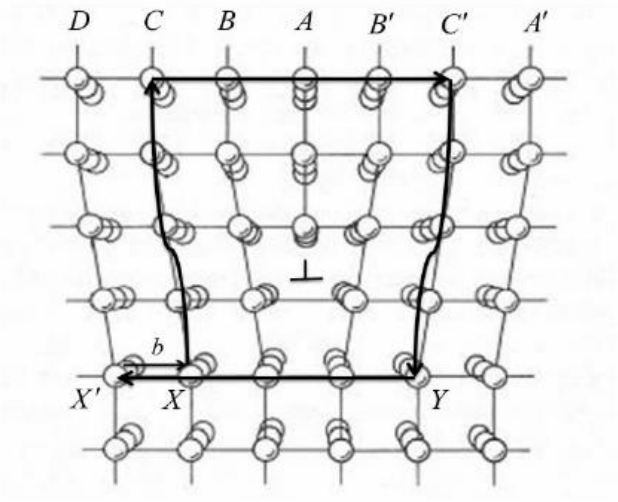

Fig. 2.1 An edge dislocation

An edge dislocation is a defect where an extra half-plane of atoms is introduced midway through the crystal, distorting nearby planes of atoms as shown in Fig 2.1[11]. When enough force is applied from one side of the crystal structure, this extra plane passes through planes of atoms breaking and joining bonds with them until it reaches the grain boundary. It can be seen that the upper part of the dislocation is under compression on both sides of the half plane, while the lower part displays considerable dilatation. By convention, the edge dislocation with the extra half plane at the bottom is defined as a positive edge dislocation and the extra half plane at the upper is a negative edge dislocation.

There are two means to produce an edge dislocation with the Burgers vector b_x as shown in Fig.2.2 [12]. In Fig. 2.2(a), a thin strip of thickness b_x is inserted into the material by making a cut along the positive y axis and pulling the material apart. In Fig.2.2 (b), a cut is made along the positive *x* axis, and then we slip the

materials below the cut in x direction by an amount b_x before re-joining. For both dislocated bodies, the induced stress field and displacements in y direction are the same which is determined by the relative displacement between material on either side of the cut (a constant, b_x, in x direction). Additionaly, to avoid any ambiguity in the sign of b_x, we adopt the convention that an observer starts at the core and walks along the cut, the positive (+) side is on the right, and the negative (–) side on the left.

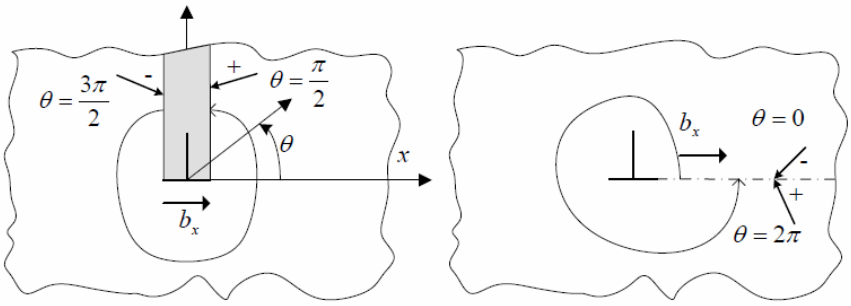

(a) The climb edge dislocation (b) The glide edge dislocation

Fig. 2.2 The creation of an edge dislocation

The jargon ‘climb’ and ‘glide’ dislocation as shown in Fig. 2.2 sometimes employed. They can be defined as follows: if the Burgers vector is perpendicular to the path cut, so that a strip is inserted as shown in Fig. 2.2(a) the dislocation is said to be ‘climb’; if the Burgers vector is parallel to the path cut, so that there are shear displacements as shown in Fig. 2.2(b), the dislocation is said to be ‘glide’, and the path cut defines the ‘glide plane’.

2.2. Modes of crack loading

There are three types of loading that a Griffith crack may experience. As

illustrated in Fig. 2.3 [13], Mode I loading (opening mode) is that the principle load is applied normal to the crack plane, tends to open the crack. Mode II (in-plane shear mode) corresponds to in-plane shear loading and tends to slide one crack face with respect to the other. Mode III refers to out-of-plane shear.

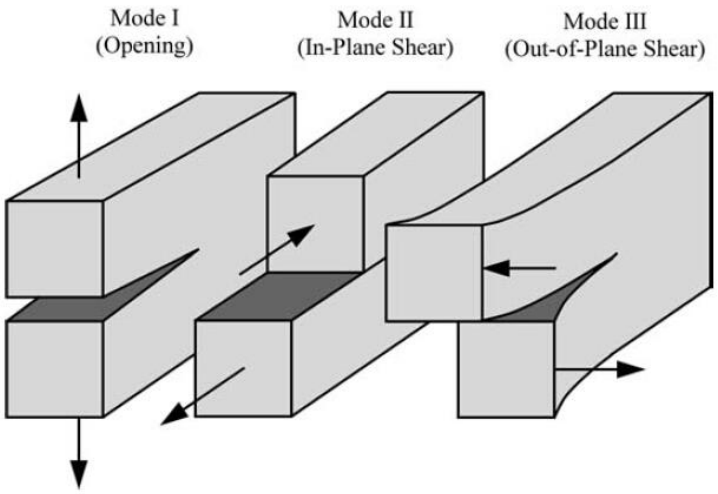

Fig. 2.3 The three modes of loading that can be applied to a crack

The stress field due to a Griffith crack can be simulated by continuously distributed dislocations [14]. When an array of single dislocations is located along the crack line, each with Burgers vector b_y, the infinitesimal Burgers vector is defined as $\delta b_y = B_y(\xi)\delta\xi$, where $B_y(\xi)$ is the density of the dislocations at point ξ.

The stress field can be obtained from the integration of the stress components $\sigma_{ij}(x, y)$ caused by the infinitesimal "discrete dislocation" $B(x)dx$ along the crack line [15]:

$$\sigma_{ij}(x,y) = \int_{-a_c}^{a_c} B(\xi)\sigma_{ij}(x-\xi, y)d\xi. \tag{2.1}$$

Here a_c is the half crack length.

To guarantee the crack faces remain traction free, the tractions along the crack-line generated by the distributed dislocations must be equal and opposite to those produced by the external load.

Then, the crack faces must physically come together at both ends for a Griffith crack. This is the no-net-dislocation condition which leads to

$$\int_{-a_c}^{a_c} B_y(\xi)d\xi = \int_{-1}^{1} B_y(s)ds = 0. \tag{2.2}$$

Equation (2.2) is for Mode I loading. For Mode II loading, we have:

$$\int_{-1}^{1} B_x(s)ds = 0. \tag{2.3}$$

2.2.1. Modelling a Crack with Dislocations

In the previous section, we introduced how stress field can be expressed by the distributed dislocation method. One of the most important advantages of distributed dislocation is that it gives a way to determine explicitly the state of stress induced by a dislocation in a range of different geometries, i.e. in an infinite place, a half-plane, strip, or adjacent to a circular inclusions. Hence, it is possible to distribute any number of dislocations within the body while preserving the boundary conditions on the surfaces of the object.

In the current work, two cases of crack problems are investigated based on this distributed dislocations method. The first case is that of a straight plane crack and the second one is a curved interface crack.

2.2.2. Straight plane cracks

For the problem of a straight plane crack as shown in Fig. 2.4, it is a mixed mode crack problem of a crack length $2a_c$. Two functions $g(x)$, $h(x)$ are introduced for the relative opening displacement and tangential shift between the upper and lower crack faces, respectively:

$$\begin{cases} g(x) = u_y(x,0^+) - u_y(x,0^-), \\ h(x) = u_x(x,0^+) - u_x(x,0^-), \end{cases} \tag{2.4}$$

where u_x and u_y are displacements over the crack.

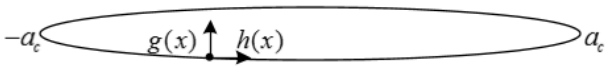

Fig. 2.4 Straight plane crack surface displacements

The relationship between the crack surface displacements and relevant Burgers vector densities are given by:

$$\begin{cases} B_y(\xi) = \dfrac{db_y(\xi)}{d\xi} = -\dfrac{dg(\xi)}{d\xi}, \\ B_x(\xi) = \dfrac{db_x(\xi)}{d\xi} = -\dfrac{dh(\xi)}{d\xi}. \end{cases} \tag{2.5}$$

2.2.3. Circular curved cracks

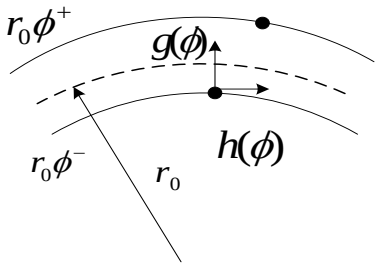

Fig. 2.5 The curved crack surface displacements

Curved cracks arise in a number of fracture problems in particle-reinforced

or fiber-reinforced composites. For example, a curved crack can be initiated along the boundary between a circular inclusion and matrix due to debonding.

The surface displacement of a circular curved crack is shown in Fig. 2.5. For a curved crack, the relationship between the crack surface displacements and dislocation densities are more complex. In polar coordinate, they can be expressed through [14]:

$$\begin{cases} B_\phi(\phi) = -\dfrac{dh(\phi)}{r_0 d\phi} - \dfrac{g(\phi)}{r_0}, \\ B_\rho(\phi) = -\dfrac{dh(\phi)}{r_0 d\phi} + \dfrac{g(\phi)}{r_0}, \end{cases} \tag{2.6}$$

where r_0 is the radius of the inclusion, $h(\phi)$ and $g(\phi)$ are the relative tangential shift and relative crack face displacement, respectively:

$$\begin{cases} h(\phi) = u_\phi(r_0^+, \phi) - u_\phi(r_0^-, \phi), \\ g(\phi) = u_\rho(r_0^+, \phi) - u_\rho(r_0^-, \phi). \end{cases} \tag{2.7}$$

The no-net-dislocation conditions in the global (x, y) set are

$$\begin{cases} \int_{-1}^{1} B_x(s)ds = \int_{-1}^{1} \left[B_\phi(s)\cos(s\omega) + B_\rho(s)\sin(s\omega) \right] ds = 0, \\ \int_{-1}^{1} B_y(s)ds = \int_{-1}^{1} \left[-B_\phi(s)\sin(s\omega) + B_\rho(s)\cos(s\omega) \right] ds = 0. \end{cases} \tag{2.8}$$

These equations are valid for open cracks, thus when a bulk load σ_{yy}^{∞} is applied, it is found that the crack remains fully open (and hence $K_I(\pm\omega) > 0$) for ω less than 70° (ω is the arc angle of half crack length). For ω greater than this value, crack closure occurs. Partially-closed curved cracks have been considered by Chao and Laws [16].

2.3. Crack-interface/inhomogeneity interaction

2.3.1. Cracks along the interface of dissimilar materials

As mentioned above, there are two major patterns of fracture damage in fiber reinforced composite materials. The first one is the interface crack, induced by defects such as micro-crack or debonding at the interface of dissimilar constituents in composites. The analysis of straight interface cracks between dissimilar materials is pioneered by Williams [17], then extended by Rice and Sih [18], Erdogan [19], and England [20]. Their work was based on the open model which assumed the tractions along the crack surfaces vanished and resulted to stress oscillation ahead of the crack tips and the physically impossible crack surface interpenetration [21]. Thereafter, the contact model [22-28] was proposed by assuming a contact zone behind the crack tip where the crack surfaces were compressed together and not permitted to interpenetrate. Based on the contact zone model, there are zones of bounded cohesive tensile and shear stresses near the crack tip.

However, for fiber-reinforced composites or any composite material with circular inclusions, cracks along the interface of fiber/matrix or inclusion/matrix due to de-bonding are usually curved (arc-shaped), for which the fracture behavior could be very different to the straight cracks. With the increasing applications of composites and alloys, more and more research attention has been paid on arc-shaped cracks along interfaces. Stippes et al. [29] reduced the problem of curved cracks to a singular integro-differential equation which can be

solved exactly when the crack is in a single homogeneous material. Wilson [30] extended this work and solved the integro-differential equation approximately for dissimilar materials. England [31], Perlman-Sih [32] and Toya [33] investigated the problem of a crack lying on the interface between a circular inclusion and an infinite plate, in which the problem was reduced to the solution of Hilbert problem with the complex function theory. Kelly et al. [34] presented the distributed dislocation method to formulate the plane problem of a crack between a circular elastic inclusion and an elastically dissimilar matrix, and some special cases solved by Gauss-Chebyschev quadrature were given as examples. Theotokoglou et al. [35] gave the analytical solution for a matrix containing a single partially de-bonded circular inclusion with non-uniform far field loading. The obtained solution was applied to study the problem of the interface crack (formed by de-bonding) interacting with a crack in the matrix. The problem of an interface arc crack around a circular elastic inclusion embedded in an elastic matrix was examined by Prasad and Simha [36] and a general approach for generating uniform/non-uniform stress fields inside a test region was demonstrated. Gorbatikh et al. [37] proposed a method to estimate the effect of partially de-bonding at matrix/inclusion interfaces on the overall elastic compliance, through studying the energy released during the de-bonding process. Using the boundary element method, Paris et al. [38] developed a micromechanical model to investigate the growing and kinking of an interface crack between fiber and matrix under loading transversal to the fiber. Analytical

methods for the arc-interface crack problems were developed by Mantic [39] and Kushch et al. [40, 41].

2.3.2. Matrix crack interacting with inclusions

The second major type of fracture damage in fiber reinforced composite materials is matrix cracking, among which crack-inclusion (2-phase) interaction problem is the most concerned problem in the open literature. This fracture model requires the strain-to-failure of the matrix to be less than that of the fibers, and the fibers still have sufficient strength to remain intact after a crack passes completely through the matrix [25]. In this damage model, the crack usually occurs near the fibers (inclusions), hence the properties of the nearby fibers have great effect on the fracture behaviors. The stress field of a radial crack interacting with a circular inclusion was investigated by Tamate [42], Atkinson [43] and Sendecky [44]. Marshall [45-49] and McCartney [50]. Hutchinson [51, 52] examined the mechanism of matrix cracking in brittle-matrix fiber composite. The interaction problem between an isolated circular inclusion and a line crack embedded in an infinite matrix was first considered by Erdogan et al. [53]. One feature of this model was its applicability to the composite materials which contain sparsely distributed inclusions. Matrix cracking and stiffness reduction during the fatigue in a glass fiber reinforced plastic (GFRP) laminate was researched by Ogin et al. [54]. A theory for progressive matrix cracking subjected to uniaxial tensile loading or shear loading in composite laminates was developed

by Tan and Nuismer [55] under elasticity theory. Kunin and Gommerstadt [56] studied the problem of a crack near an inclusion by using the projection integral equation method.

For the matrix cracking in the coated-inclusion/matrix system (3 material phases involved), the material properties of coating phase have great influence on the fracture behaviors. Walpole [57] investigated the problem of a coated inclusion in an elastic medium and showed how to take account of the pronounced influence. Theocaris and Demakos [58] proved that the fracture toughness of hard plates, reinforced with brittle inclusions, can be altered by introducing an intermediate thin layer made of a deformable phase in these composite materials. A micromechanical model using simultaneously Green's function techniques and interfacial operators was proposed to solve the elastic inhomogeneous inclusion problem by Cherkaoui et al. [59]. More research work on coated-inclusion problem can be found in [60-67] and provided a deep investigation of the mechanism of such kind of structure under different loading conditions.

To effectively study how the fracture behavior of a crack is influenced by the near-by multiple inclusions in fiber-reinforced composite materials, the three-phase cylindrical model was introduced by Hashin and Rosen [68]. It is the multiple-inclusion/matrix system studied in the current work. In this model, it assumes that the crack and the nearest inclusion are embedded in their immediate surrounding pure matrix, while other inclusions and matrix parts are replaced by

an equivalent homogeneous media (the composite material), hence three dissimilar material phases are involved in this model, the fiber (the inclusion nearest to the crack), the matrix and the composite. Based on this model, many problems in such composites have been solved. To name a few, Christensen and Lo [69] obtained the solutions of effective shear properties in three-phase sphere and cylinder model. Luo and Weng [70] derived the elastic field in a three-phase cylindrically concentric, transversely isotropic solid due to a uniform stress-free transformation strain in the central fiber. Luo and Chen [71, 72] found an exact solution for the stress field due to an edge dislocation embedded in a three-phase composite. Even more works can be found in [73-79], most of which focus on the elastic fracture behavior analysis in composite materials.

2.4. Numerical solutions of singular integral equations

2.4.1. Guass-Chebyshev quadrature

There are a number of effective numerical procedures for handling singular integral equations with Cauchy kernels. Among them, the most widely used one is the Gauss-Chebyshev quadrature developed by Erdogan and Gupta [80]. To show how this quadrature works, an example of the singular integral equation is given in the following equation

$$F(t)=\frac{1}{\pi}\int_{-1}^{1}B_y(s)\frac{1}{t-s}ds, \qquad |t|<1. \tag{2.9}$$

It arises in a two-dimensional treatment of crack where the kernel of the integral is formed from a dislocation solution, $F(t)$ is an unknown function of traction

and $B_y(s)$ is the dislocation density.

There are four available cases of unknown function $B_y(s)$ based on the end-point behavior of the crack as illustrated in Table 2.1.

-1 \ 1	Singular	Bounded
Singular	I	II
Bounded	III	IV

Table 2.1 The four cases of end-point behaviour[14]

case	$\omega(s)$	s_i	t_k	n	W_i
I	$(1-s^2)^{-1/2}$	$\cos(\pi\frac{2i-1}{2N})$	$\cos(\pi\frac{k}{N})$	1	$\frac{1}{N}$
II	$(1-s)^{1/2}(1+s)^{-1/2}$	$\cos(\pi\frac{2i}{2N+1})$	$\cos(\pi\frac{2k-1}{2N+1})$	0	$\frac{2(1-s_i)}{2N+1}$
III	$(1-s)^{-1/2}(1+s)^{1/2}$	$\cos(\pi\frac{2i-1}{2N+1})$	$\cos(\pi\frac{2k}{2N+1})$	0	$\frac{2(1+s_i)}{2N+1}$
IV	$(1-s^2)^{+1/2}$	$\cos(\pi\frac{i}{N+1})$	$\cos(\pi\frac{2k-1}{2N+2})$	-1	$\frac{(1-s_i^2)}{N+1}$

Table 2.2 Gauss-Chebyshev quadrature formulae for Cauchy kernels[14]

In the current work only the case I, “singular-at-both-ends” are investigated. The Burgers vector density could be written as

$$B(s)=\omega(s)\phi(s), \tag{2.10}$$

where $\phi(s)$ is the bounded function and $\omega(s)$ is the corresponding fundamental function, listed in Table. 2.2.

Substituting Eq. (2.10) into (2.9), using Gauss-Chebyshev numerical quadrature formulae, the singular integral equation (2.9) can be reduced to a set of $N-n$ algebraic equations having the form:

$$F(t_k)=\sum_{i=1}^{N} W_i \frac{\phi(s_i)}{t_k-s_i} \qquad k=1,2,...,N-n, \tag{2.11}$$

where the integer n depends on the combination of end–point behavior included in Table 2.2. W_i are the weight functions appropriate to the quadrature formulae. The coordinates of the integrations points, s_i, and the collocation points, t_k, are also given in Table 2.2.

In Eq. (2.11), for the case of "singular-at-both-ends", $F(t_k)$ are known functions of tractions, whilst W_i is $\frac{1}{N}$, we get:

$$F(t_k) = \frac{1}{N}\sum_{i=1}^{N}\frac{\phi_y(s_i)}{t_k - s_i} \qquad k = 1...N-1. \tag{2.12}$$

Combining with the no-net-dislocation requirement

$$\frac{\pi}{N}\sum_{i=1}^{N}\phi_y(s_i) = 0, \tag{2.13}$$

the unknowns $\phi_y(s_1), \phi_y(s_2), ..., \phi_y(s_N)$ can be obtained.

After solving the system of linear equations, the values of the function $\phi_y(s)$ are known at the discrete set of points s_i, given by Krenk [81]:

$$\begin{cases} \phi(+1) = \dfrac{1}{N}\displaystyle\sum_{i=1}^{N}\frac{\sin\left[\dfrac{2i-1}{4N}\pi(2N-1)\right]}{\sin\left[\dfrac{2i-1}{4N}\pi\right]}\phi(s_i), \\ \phi(-1) = \dfrac{1}{N}\displaystyle\sum_{i=1}^{N}\frac{\sin\left[\dfrac{2i-1}{4N}\pi(2N-1)\right]}{\sin\left[\dfrac{2i-1}{4N}\pi\right]}\phi\left(N+1-i\right), \end{cases} \tag{2.14}$$

and

$$\phi(s) = \frac{2}{N}\sum_{i=1}^{N}\left[\frac{1}{2} + \sum_{i=1}^{N}\cos\left[\frac{2i-1}{2N}j\pi\right]\cos\left[j\gamma\right]\right]\phi(s_i). \tag{2.15}$$

2.4.2. Gauss-Jacobi quadrature

To illustrate the difference between Gauss-Chebyshev quadrature and Guass-Jacobi quadrature, the same singular integral equation is used.

$$F(t)=\frac{1}{\pi}\int_{-1}^{1}B_y(s)\frac{1}{t-s}ds, \qquad |t|<1,$$

$$B(s)=\omega(s)\phi(s)$$

For Jacobi quadrature, we assume that the corresponding fundamental function $\omega(s)$ is same as shown in Table 2.2. The bounded function $\phi(s)$ is assumed to be an infinite series of Jacobi polynomials $P_n^{(a,b)}$,

$$\phi(s)=\sum_{n=0}^{\infty}c_nP_n^{(a,b)}(s). \tag{2.16}$$

Substituting Eqs. (2.16), (2.10) into (2.9), the original SIE becomes:

$$F(t)=\frac{1}{\pi}\sum_{n=0}^{\infty}c_n\int_{-1}^{1}\frac{\omega(s)P_n^{(a,b)}(s)}{t-s}ds, \qquad |t|<1. \tag{2.17}$$

Now the unknowns become the series of c_n since both $\omega(s)$ and $P_n^{(a,b)}(s)$ are already known. We will use the numerical technique for solving singular integral equations in the following chapters.

2.5. Small-scale yielding and the Dugdale Model

The investigation of elastic-plastic fracture behaviors started from late 1960s, Arthur and Blackbur [82, 83] considered a single crack in a non-work hardening elastic-plastic material under antiplane strain due to a normal shear stress at infinity. By analyzing a crack with steady growth under anti-plane shear, Chitaley and McClinto [84] found that a primary plastic zone included in an angle

of $\pm 19.7^\circ$ ahead of the crack tip, and two very thin secondary (reverse) plastic zones along the crack flanks, each included in an angle of 0.37°. The application of elastic-plastic fracture analysis for an interfacial crack began to emerge in 1980s. Shih and Asaro [85-87] provided numerical solutions for a crack which lies along the interface of an elastic-plastic medium and a rigid substrate under small-scale yielding and large-scale yielding. An exact asymptotic analysis for a crack lying on the interface of an elastic-plastic material and a linear elastic material was presented by Wang [88], in which the results obtained were free of oscillatory singularity and had the HRR type singularity in the plastic angular zone. Zhang et al. [89] solved a particular case of interface crack problem by assuming the materials at each side of the interface to have different yield strength and plastic strain hardening exponent, while the elastic properties were identical. Lee and Kim [90] investigated the J-integral and the stress fields near the tip of a crack at an interface between dissimilar materials with plastic hardening mismatches.

However, even so much work can be found on studying the elastic-plastic fracture behaviors of cracks, it may still be difficult to apply these complicated elastic-plastic analyses to engineering practice. Since for crack problems in composite materials, the fracture behavior could be influenced by a lot of factors. In our current study, two plastic zone correction models are provided to solve elastic-plastic fracture problems in fiber-reinforced composite materials. The inaccuracy of linear elastic fracture mechanics can be improved by simple plastic

zone correction ahead of the crack tips where the elastic stress analysis can be used to estimate the elastic-plastic boundary, and thus avoid the complex full elastic-plastic fracture mechanics analysis.

As plastic zone correction technique deals primarily with small-scale yielding, the inelastic region will be referred to as the plastic region. The sizes of these small plastic regions can be estimated by two methods: the Irwin approach [91], where the elastic stress analysis is used to estimate the elastic-plastic boundary, and the strip-yield model also known as the Dugdale model [92].

The Dugdale model, which is illustrated in Fig. 2.6, was first proposed by Dugdale [92] and Barenblatt [93]. They assumed a long, slender plastic zone at the crack tip and only considered a through crack in an infinite plate. The strip-yield plastic zone is modelled by assuming a crack of length $2a_c + 2\rho$, where ρ is the length of the plastic zone, carrying on a closure normal stress equal to σ_{ys} applied at each crack tip.

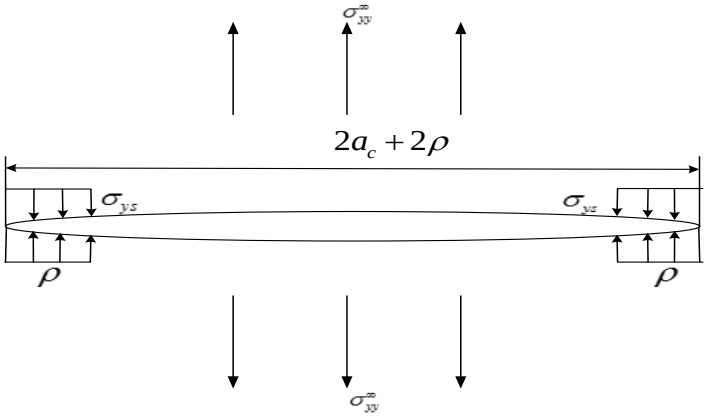

Fig. 2.6 The Dugdale model

The theory of the Dugdale model was later fully developed by Bilby et al. [10, 94] and Hays and Williams [95]. Following them, Theocari and Gdoutos [96]

extended the model to encompass the influence of strain hardening on the plastic enclaves developed at the tips of a crack in a plate subjected to tension at infinity. Galatenko [97] proposed a generalized model of a Dugdale crack which allows for different yield criteria. The Dugdale crack in a bi-material interface was studied by Wang and Shen [98]. Unger [99] compared the results of the Dugdale model to an elastic-perfectly plastic crack under the Tresca yield condition.

The plastic zone size ρ shown in Fig. 2.6 for a Dugdale model must be chosen such that the stress intensity factors from the remote tension and closure stress cancel each other:

$$K_{\sigma} + K_{closure} = 0. \tag{2.18}$$

Here K_{σ} is the stress intensity factor induced by external loading, $K_{closure}$ for stress intensity factor induced by closure stress. The Dugdale model can be extended to the mixed mode Dugdale model [100] when a crack is under combined mode I and mode II loadings.

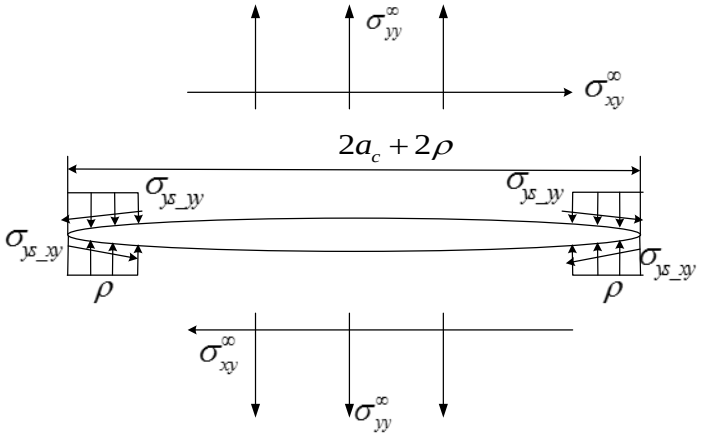

Fig. 2.7 Mixed mode Dugdale model

As shown in Fig. 2.7, the crack is subjected to both mode I and mode II loadings, the relationship between the SIFs from the remote loading and those from the closure stresses are:

$$\begin{cases} K_{I\sigma} + K_{I\,clsoure} = 0, \\ K_{II\,\sigma} + K_{II\,clsoure} = 0. \end{cases} \tag{2.19}$$

Equation (2.19) can be rewritten into complex form so that the format can be similar to Eq. (2.18). In the above equations, $K_{I\sigma}$ and $K_{II\,\sigma}$ represent the mode I and mode II stress intensity factor induced by external load, $K_{I\,clsoure}$ and $K_{II\,clsoure}$ are the SIFs induced by closure stresses.

2.6. Crack tip opening displacement

The crack tip opening displacement (CTOD) is the displacement at the original crack tip. It is an important parameter to judge whether a fracture will occur in ductile materials. One of the earliest researchers investigated the crack opening displacement is Wells [101]. While examining fractured test specimens, Wells noticed that the crack faces had moved apart prior to fracture. Plastic deformation had blunted an initially sharp crack as illustrated in Fig. 2.8.

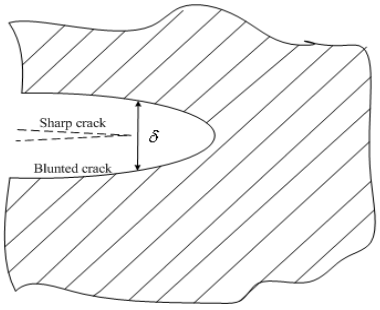

Fig. 2.8 Crack opening displacement. An initially sharp crack blunts with plastic deformation, resulting in a finite displacement δ at the crack tip [13].

During his research, he realized that the degree of crack blunting increased in proportion to the toughness of the material. This observation led Wells to propose the opening at the crack tip as a measure of fracture toughness. This parameter is known as crack tip opening displacement (CTOD). The Dugdale model provides an alternate means for analyzing CTOD [102]. One of the most widely used definitions is shown in Fig. 2.9, where the CTOD can be defined as the relative displacement between crack faces at the end of the strip-yield zone.

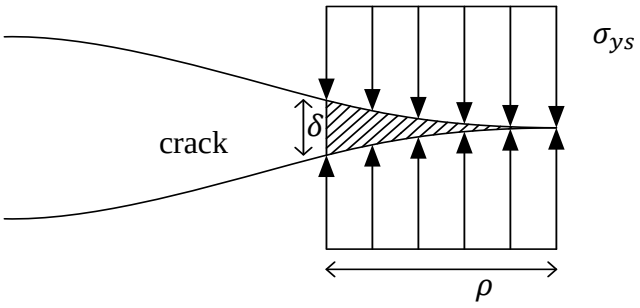

Fig. 2.9 Estimation of CTOD from the Dugdale model [102].

According to this definition, reference [102] gives a solution of CTOD of a through crack (shown in Fig. 2.9) in an infinite plate subject to a remote tensile stress,

$$\delta = \frac{8\sigma_{ys}a}{\pi E}\ln\sec\left(\frac{\pi}{2}\frac{\sigma}{\sigma_{ys}}\right). \tag{2.20}$$

Here we use δ to represent the CTOD of the crack.

2.7. Irwin Model

In 1968, the famous Irwin model [91] was proposed to estimate the PZS and CTOD of a crack. In this model, Irwin showed that the crack tip plasticity makes the crack behave as if it were slightly longer. Thus one can estimate CTOD by

solving for the displacement at the physical crack tip, assuming an effective crack length of $a_c + r_y$, where a_c is the half crack length and r_y is the displacement behind the effective crack tip. The plastic zone size r_y is determined by setting the crack tip stress $\sigma_{yy}(r, \theta = 0)$ equal to the yield stress σ_{ys}. This leads to the following plastic zone size in homogenous material:

$$r_y = \frac{1}{2\pi}\left(\frac{K_I}{\sigma_{ys}}\right)^2. \tag{2.21}$$

The above estimation can be improved by re-distributing the stress within the plastic zone. This can be done by balancing the force that would have been carried by the elastic material from $r = 0$ to $r = r_y$ with that carried by the plastic zone size r_p which sustains a stress of σ_{ys}:

$$\sigma_{ys} r_p = \int_0^{r_y} \sigma_{yy} dr = \int_0^{r_y} \frac{K_I}{\sqrt{2\pi r}} dr, \tag{2.22}$$

which leads to:

$$r_p = 2r_y = \frac{1}{\pi}\left(\frac{K_I}{\sigma_{ys}}\right)^2. \tag{2.23}$$

In Eqs. (2.21) to (2.23), K_I represents the mode I stress intensity factor. r_y is the first estimation of plastic zone size and r_p is the second order estimation of plastic zone size, respectively. From Eq. (2.21), the CTOD under this Irwin model can be estimated as:

$$\delta = \frac{8}{E'} K_I \sqrt{\frac{r_y}{2\pi}}, \tag{2.24}$$

where $E' = E$ for plain stress, is the Young's modulus of the material where the crack is located, and $E' = E/\left(1 - v^2\right)$ for plain strain. v is the Poisson's ratio of the material. The above estimations of PZS and CTOD are for crack located in

single homogeneous material under uniform tensile loading. If the crack is located in composite materials and under mixed-mode loading conditions, a generalized Irwin model is needed which will be introduced in the current work.

2.8. Conclusions

In this chapter, the concept of distributed dislocation was introduced firstly, as it is the fundamental theory used in our current study. Then the continuously distributed dislocation is employed to simulate the stress field for a Griffith crack. The general way of modelling a crack using dislocation method is introduced for both straight crack and curved crack cases. Jacobi Polynomials and Gauss-Legendre Integration method for solving resulted singular integral equations are introduced. Finally, a brief review on Dugdale model and Irwin model was presented to help us have a brief understanding of the elastic-plastic fracture behavior investigation in the following chapters.

Chapter 3 Elastic-Plastic Stress Investigation for an Arc-shaped Interface Crack in Composite Materials

3.1. Introduction

Literatures on crack in fibers-reinforced composite materials have been reviewed in the previous chapter. Historically, although a lot of research work has been done on curved interface crack [103-105], there is still a lack of literature for these problems with plastic zone corrections at the crack tips. For ductile materials (such as metal-matrix composites), fracture analysis will be more accurate if plastic zone corrections at crack tips are made, and the crack tip opening displacement criterion is more applicable to judge if a fracture will take place. Particularly for interface crack problems, it is not practical for engineers to use complex stress intensity factors as parameter to judge fracture occurrence.

In this chapter, an approach to solve the plastic zone size (PZS) and crack tip opening displacement (CTOD) for arc-shaped interface cracks is developed based on the mixed-mode Dugdale model [100]. The PZS and CTOD are evaluated for an interface crack between a circular inclusion and a matrix under uniaxial tensile loading. The mixed-mode Dugdale model is developed to deal with the plastic deformation, where the von Mises yielding criterion is applied. The PZS is calculated by satisfying the condition that the complex stress intensity factors vanish in the plastic zones. The corresponding CTOD can be obtained by the distributed dislocation theory after the PZS is obtained.

3.2. The physical problem and formulation

3.2.1. The arc-shaped interfacial crack with plastic zone corrections

The physical problem is shown in Fig. 3.1(a), where the circular inclusion (with radius r_0) is embedded in an infinite matrix (or the matrix is sufficiently large comparing with the inclusion). The arc-shaped interface crack occupies the region $r = r_0$, $-\omega \le \theta \le \omega$. At each crack tip, there is a plastic strip over the region of $\omega < |\theta| < \omega + \rho$ along the interface. The mechanical properties of the matrix and the inclusion are denoted by '1' and '2', respectively. The normal stress σ_{ys_rr} and the shear stress $\sigma_{ys\_r\theta}$ in the plastic zone at the right crack tip are shown in Fig. 3.1(b). The parameter δ is used to denote the crack tip opening displacement.

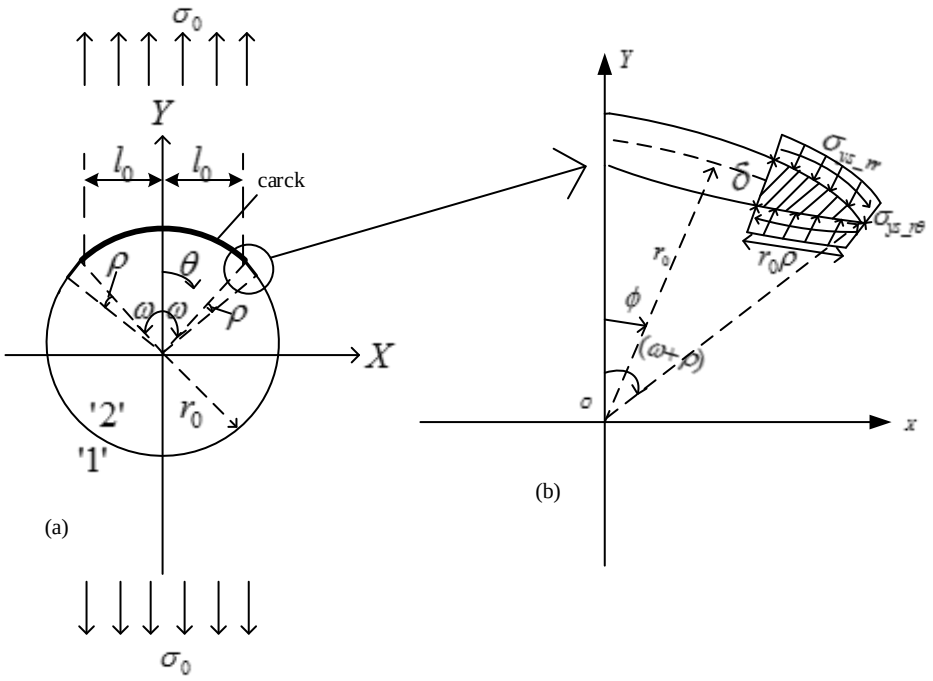

Fig. 3.1 An arc-shaped interface crack between an inclusion and an infinite matrix under remote tension loading. (a) An arc-shaped interface crack with the plastic zone size (arc angle) ρ at each crack tip; (b) The normal and shear stresses in the plastic zone.

The normal stress and the shear stress in the plastic zone should satisfy the

Von Mises yielding criterion and have the form of:

$$\sigma_{ys}^2 = \sigma_{ys\_rr}^2 + 3\sigma_{ys\_r\theta}^2. \tag{3.1}$$

Here, σ_{ys} is the lower yielding stress of the two materials. When the materials are fixed, the yielding stress is a constant.

The plastic zone size (angle of the arc) ρ, the normal stress σ_{ys_rr} and the shear stress $\sigma_{ys\_r\theta}$ can be determined when the stress singularity vanishes at crack tips:

$$K_{closure} + K_{\sigma} = 0, \tag{3.2}$$

where $K_{closure}$ is the stress intensity factor (SIF) induced by the stresses in the plastic zone and K_{σ} is the SIF induced by the external load.

With the distributed dislocation theory, the traction-free condition on the crack surface gives (Kelly et al. [34]):

$$\begin{aligned} -\hat{\sigma}_{rr}(\theta) &= \frac{C}{\pi}\int_{-\omega}^{\omega}\left[B_{\phi}(\phi)G_{\phi rr}(\gamma;\alpha,\beta) + B_{\rho}(\phi)G_{\rho rr}(\gamma;\beta)\right]r_0 d\phi, \\ -\hat{\sigma}_{r\theta}(\theta) &= \frac{C}{\pi}\int_{-\omega}^{\omega}\left[B_{\phi}(\phi)G_{\phi r\theta}(\gamma;\beta) + B_{\rho}(\phi)G_{\rho r\theta}(\gamma;\beta)\right]r_0 d\phi, \qquad |\theta| \le \omega, \end{aligned} \tag{3.3}$$

where $\hat{\sigma}_{rr}(\theta)$ and $\hat{\sigma}_{r\theta}(\theta)$ are the normal and shear stresses arising by the far field load when the crack is absent. When the external load is uniaxial tension, they have the form of [106]:

$$\begin{aligned} \hat{\sigma}_{rr}(r_0,\theta) &= \frac{\sigma_0}{2}\left[\frac{1+\alpha}{1+\alpha-2\beta} + \left(\frac{1+\alpha}{1+\beta}\right)\cos 2\theta\right], \\ \hat{\sigma}_{r\theta}(r_0,\theta) &= -\frac{\sigma_0}{2}\left(\frac{1+\alpha}{1+\beta}\right)\sin 2\theta, \ |\theta| \le \omega, \end{aligned} \tag{3.4}$$

C, α and β are the bi-material parameters given by

$$
\begin{aligned}
&C=\frac{2\mu_1\left(1+\alpha\right)}{\left(\kappa_1+1\right)\left(1-\beta^2\right)}=\frac{2\mu_2\left(1-\alpha\right)}{\left(\kappa_2+1\right)\left(1-\beta^2\right)},\\
&\alpha=\frac{\mu_2\left(\kappa_1+1\right)-\mu_1\left(\kappa_2+1\right)}{\mu_2\left(\kappa_1+1\right)+\mu_1\left(\kappa_2+1\right)},\ \beta=\frac{\mu_2\left(\kappa_1-1\right)-\mu_1\left(\kappa_2-1\right)}{\mu_2\left(\kappa_1+1\right)+\mu_1\left(\kappa_2+1\right)}.
\end{aligned}
\tag{3.5}
$$

Here $\kappa_j=3-4\nu_j$ in plane strain and $\kappa_j=\left(3-\nu_j\right)/\left(1+\nu_j\right),\ j=1,2$ in plane stress. ν_j and μ_j are the Poisson's ratio and the shear modulus of material j, respectively.

The kernels in the integral equations (3.3) are given by [34]:

$$
\begin{aligned}
G_{\phi rr}&=\frac{1}{2r_0}\left[\frac{2-\beta\left(1+\alpha\right)}{1+\alpha-2\beta}+\left(1-\beta\right)\cos\gamma\right]+\pi\beta\delta(r_0\gamma),\\
G_{\phi r\theta}&=G_{\rho rr}=\frac{1}{2r_0}\left[\beta\sin\gamma+\frac{\sin\gamma\cos\gamma}{1-\cos\gamma}\right],\\
G_{\rho r\theta}&=\frac{1}{2r_0}\left[\beta-\left(1-\beta\right)\cos\gamma\right]-\pi\beta\delta(r_0\gamma),
\end{aligned}
\tag{3.6}
$$

in which $\delta\left(x\right)$ is the Dirac delta function and $\gamma=\theta-\phi$.

Substituting $s=\phi/\omega$, $t=\theta/\omega$ into Eq. (3.3), and combine the two equations, we have

$$
F(t)=-\beta B(t)-\frac{i}{\pi}\int_{-1}^{1}\frac{B(s)}{t-s}ds+\int_{-1}^{1}\left[B(s)K_1^{'}(t;s)+\overline{B(s)}K_2^{'}(t;s)\right]ds,
\tag{3.7}
$$

$$
F(t)=-\frac{1}{C}\left[\hat{\sigma}_{r\theta}(t)-i\hat{\sigma}_{rr}(t)\right],
\tag{3.8}
$$

$$
B(t)=B_\rho(t)+iB_\phi(t),
\tag{3.9}
$$

with

$$
\begin{aligned}
K_1^{'}(t;s)&=\frac{\omega}{2\pi}\left[\left(K_{\rho r\theta}-K_{\phi rr}\right)-i\left(K_{\phi r\theta}+K_{\rho rr}\right)\right],\\
K_2^{'}(t;s)&=\frac{\omega}{2\pi}\left[\left(K_{\rho r\theta}+K_{\phi rr}\right)+i\left(K_{\phi r\theta}-K_{\rho rr}\right)\right].
\end{aligned}
\tag{3.10}
$$

Here, the over bar denotes the complex conjugate $\overline{B(s)}=B_\rho(s)-iB_\phi(s)$. The kernels $K_{\rho r\theta},K_{\phi rr},K_{\phi r\theta},K_{\rho rr}$ are given in the work of Kelly et al. [34].

The consistency condition which can be obtained from the requirement of no-net-dislocation is

$$\int_{-1}^{1}\left[B_y(s)+iB_x(s)\right]ds=\int_{-1}^{1}B(s)\left[\cos(\omega s)+i\sin(\omega s)\right]ds=0. \quad (3.11)$$

Equations (3.7) and (3.11) can be solved numerically. The dislocation density $B(s)$ is expressed as

$$B(s)=\omega(s)\sum_{n=0}^{\infty}c_nP_n^{(a,b)}(s)=(1-s)^a(1+s)^b\sum_{n=0}^{\infty}c_nP_n^{(a,b)}(s). \quad (3.12)$$

Here, $P_n^{(a,b)}$ is an infinite series of Jacobi Polynomials, and

$$a=-\frac{1}{2}+i\varepsilon,\ b=-\frac{1}{2}-i\varepsilon,\ \varepsilon=\frac{1}{2\pi}\log\left(\frac{1+\beta}{1-\beta}\right). \quad (3.13)$$

Substituting Eq. (3.12) into (3.7), and using the following relation given by Krenk [107]

$$-\beta\omega(t)P_n^{(a,b)}(t)-\frac{i}{\pi}\int_{-1}^{1}\frac{\omega(s)P_n^{(a,b)}(s)}{t-s}ds=\frac{i}{2}\sqrt{1-\beta^2}\,P_{n-1}^{(-a,-b)}(t), \quad (3.14)$$

we have

$$F(t)=\sum_{n=0}^{\infty}c_n\frac{i}{2}\sqrt{1-\beta^2}\,P_{n-1}^{(-a,-b)}(t)+\sum_{n=0}^{\infty}c_nG_n^{(1)}(t)+\sum_{n=0}^{\infty}\overline{c_n}G_n^{(2)}(t). \quad (3.15)$$

Here

$$\begin{aligned}G_n^{(1)}(t)&=\int_{-1}^{1}\omega(s)P_n^{(a,b)}(s)K_1'(t;s)ds,\\ G_n^{(2)}(t)&=\int_{-1}^{1}\overline{\omega(s)}\,\overline{P_n^{(a,b)}(s)}K_2'(t;s)ds.\end{aligned} \quad (3.16)$$

The following orthogonality relation is used

$$\int_{-1}^{1}\omega(s)P_n^{(a,b)}(s)P_k^{(a,b)}(s)ds=\begin{cases}0, & n\neq k\\ \Theta_k^{(a,b)} & n=k\end{cases},\quad k=0,1,... \quad (3.17)$$

where

$$\Theta_k^{(a,b)} = \frac{2^{a+b+1}}{2k+a+b+1}\frac{\Gamma(k+a+1)\Gamma(k+b+1)}{k!\Gamma(k+a+b+1)}.$$

Here Γ is gamma function.

Now multiplying both sides of Eq. (3.15) by $\omega^{-1}(t)P_k^{(-a,-b)}(t)$, where $\omega^{-1}(t)=(1-t)^{-a}(1+t)^{-b}$ and integrating the equation over [-1, 1], making use of Eq. (3.17) yields the following system of equations:

$$f_k = \frac{i}{2}\sqrt{1-\beta^2}\Theta_k^{(-a,-b)}c_{k+1} + \sum_{n=0}^{\infty}c_n d_{nk}^{(1)} + \sum_{n=0}^{\infty}\overline{c}_n d_{nk}^{(2)},\ k=0,1,... \quad (3.18)$$

with

$$\begin{aligned} f_k &= \int_{-1}^{1}\omega^{-1}(t)P_k^{(-a,-b)}(t)F(t)dt, \\ d_{nk}^{(i)} &= \int_{-1}^{1}\omega^{-1}(t)P_k^{(-a,-b)}(t)G_n^{(i)}(t)dt,\ i=1,2. \end{aligned} \quad (3.19)$$

Combining Eqs. (3.11), (3.12) and (3.18), the $n+1$unknowns, i.e. $c_0, c_1, ..., c_n$, can be solved. Guass-Legendre Integration Method is used to get the integration of Eq. (3.19).

For the curved interface crack, the definition of dislocation densities ($B(\phi)=B_\rho(\phi)+iB_\phi(\phi)$) is given by:

$$-B(\phi) = \frac{d\left(\Delta u_\rho(\phi)+i\Delta u_\phi(\phi)\right)}{r_0 d\phi} + i\frac{\left(\Delta u_\rho(\phi)+i\Delta u_\phi(\phi)\right)}{r_0}, \quad (3.20)$$

$$\Delta u_\rho(r_0,\phi)+i\Delta u_\phi(r_0,\phi) = \left[u_\rho(r_0^+,\phi)-u_\rho(r_0^-,\phi)\right]+i\left[u_\phi(r_0^+,\phi)-u_\phi(r_0^-,\phi)\right], \quad (3.21)$$

where u_ρ and u_ϕ are displacements in radial and tangential directions.

The left hand side of Eq. (3.21) is given by England [31]:

$$\Delta u_\rho(r_0,\phi)+i\Delta u_\phi(r_0,\phi) = \frac{r_0\left(1+\alpha^*\right)Be^{-\varepsilon\omega}}{\mu_1\mu_2\sqrt{\alpha^*}}\left|e^{i\phi}-e^{i\omega}\right|^{\frac{1}{2}+i\varepsilon}\left|e^{i\phi}-e^{-i\omega}\right|^{\frac{1}{2}-i\varepsilon}e^{-\frac{i}{2}\phi}, \quad (3.22)$$

Here B is a constant related to material properties and the external load and

$\alpha^* = (\mu_1 + \mu_2\kappa_1)/(\mu_2 + \mu_1\kappa_2)$.

The stresses on the bonded interface of the two media are also given by [31]:

$$\sigma_{rr} + i\sigma_{r\theta} = -\sigma_0 + \frac{2(1+\alpha^*)Be^{-\varepsilon\omega}}{\mu_1 + \mu_2\kappa_1}\left(e^{i\phi} - \cos\omega - 2\varepsilon\sin\omega\right) \times e^{-i\eta}\left|e^{i\phi} - e^{i\omega}\right|^{-\frac{1}{2}+i\varepsilon}\left|e^{i\phi} - e^{-i\omega}\right|^{-\frac{1}{2}-i\varepsilon}, \tag{3.23}$$

where

$$\begin{cases}\eta = (\phi + \pi)/2, & \phi > \omega,\\ \eta = (\phi - \pi)/2, & \phi < -\omega.\end{cases}$$

The stress intensity factors at the right crack tip K_R is given by [108]:

$$K_R = \lim_{r\to 0}\left(\sigma_{rr}(r) + i\sigma_{r\theta}(r)\right)\sqrt{2\pi r_0 r}(r_0 r)^{-i\varepsilon}. \tag{3.24}$$

Here $r = \omega - \phi$. Substituting Eq. (3.22) into (3.20), we have

$$-B(r) = \frac{(1+\alpha^*)Be^{-\varepsilon\omega}e^{-\frac{i}{2}\omega}\left|e^{ir} - 1\right|^{-\frac{1}{2}+i\varepsilon}\left|e^{i(r+2\omega)} - 1\right|^{-\frac{1}{2}+i\varepsilon}e^{-i\frac{r}{2}}}{\mu_1\mu_2\sqrt{\alpha^*}}\times$$
$$\left\{(\frac{1}{2}+i\varepsilon)\cos\frac{r}{2}\left|e^{i(r+2\omega)} - 1\right| + (\frac{1}{2}-i\varepsilon)\cos\frac{r+2\omega}{2}\left|e^{ir} - 1\right| + \frac{i}{2}\left|e^{ir} - 1\right|\left|e^{i(r+2\omega)} - 1\right|\right\}, \tag{3.25}$$

Equation (3.25) can be rewritten as:

$$(1+\alpha^*)Be^{-\varepsilon\omega}\left|e^{ir} - 1\right|^{-\frac{1}{2}+i\varepsilon}\left|e^{i(r+2\omega)} - 1\right|^{-\frac{1}{2}-i\varepsilon}$$
$$= \frac{\mu_1\mu_2\sqrt{\alpha^*}B(r)e^{\frac{i}{2}\omega}e^{i\frac{r}{2}}}{\left\{(\frac{1}{2}+i\varepsilon)\cos\frac{r}{2}\left|e^{i(r+2\omega)} - 1\right| + (\frac{1}{2}-i\varepsilon)\cos\frac{r+2\omega}{2}\left|e^{ir} - 1\right| + \frac{i}{2}\left|e^{ir} - 1\right|\left|e^{i(r+2\omega)} - 1\right|\right\}}. \tag{3.26}$$

Substituting Eqs. (3.26), (3.23) into (3.24), the stress intensity factor K_R is expressed as

$$K_R = \lim_{r\to 0}\left(\sigma_{rr}(r)+i\sigma_{r\theta}(r)\right)\sqrt{2\pi r_0 r}\,(r_0 r)^{-i\varepsilon} = \sqrt{\pi r_0\omega}\left(2r_0\omega\right)^{-i\varepsilon} C\sqrt{1-\beta^2}\,\Phi(1). \tag{3.27}$$

Equation (3.27) is for calculating the SIF of the right crack tip. For the left side, it can be obtained in the same procedure but the equations involved need to be modified accordingly.

To solve $K_{closure}$, the left-hand side of Eq. (3.3) should be the normal and the shear stress in the plastic zone as shown in Fig. 3.1(b):

$$\hat{\sigma}_{rr}(\theta) = \begin{cases} \sigma_{ys\_rr} & -\omega-\rho<\theta<-\omega, \\ 0 & -\omega<\theta<\omega, \\ \sigma_{ys\_rr} & \omega<t<\omega+\rho. \end{cases} \tag{3.28}$$

and

$$\hat{\sigma}_{r\theta}(t) = \begin{cases} \sigma_{ys\_r\theta} & -\omega-\rho<\theta<-\omega, \\ 0 & -\omega<\theta<\omega, \\ -\sigma_{ys\_r\theta} & \omega<t<\omega+\rho. \end{cases} \tag{3.29}$$

The stress intensity factor K_σ, caused by the external load is obtained in the same way according to the type of the external load. Two different loading conditions are given in Fig. 3.2. Here, σ_0 is the external tensile loading.

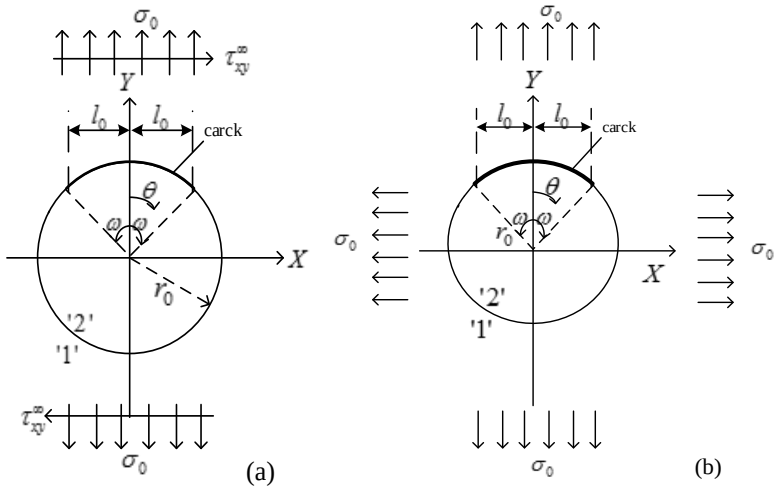

Fig. 3.2. An arc-shaped interface crack (a) under uniaxial tensile loading; (b) under hydrostatic loading.

In the equations of (3.1) and (3.2), we have three unknowns: ρ, σ_{ys_rr} and $\sigma_{ys\_r\theta}$. Correspondingly, there are three equations since Eq. (3.2) is in the complex form, which includes a real and an imaginary part. By an iterative procedure, the three unknowns can be solved.

3.2.2. The crack tip opening displacement

The crack tip opening displacement (CTOD) is a function of the plastic zone size (PZS). After the angle ρ is solved, we can calculate the CTOD by solving Eq. (3.20):

$$-B(\phi)=\frac{d\left(\Delta u_{\rho}(\phi)+i\Delta u_{\phi}(\phi)\right)}{r_0 d\phi}+i\frac{\left(\Delta u_{\rho}(\phi)+i\Delta u_{\phi}(\phi)\right)}{r_0}.$$

Here, $B(\phi)=B_{\rho}(\phi)+iB_{\phi}(\phi)$ is the dislocation density in complex form. $\Delta u_{\rho}(\phi)$ and $\Delta u_{\phi}(\phi)$ are the relative opening displacement and the relative tangential shift between the crack faces, respectively.

Noting that this is a non-homogeneous equation with constant coefficients, it can be solved by either the method of undetermined coefficients or the method of variation of parameters. Substituting $\phi=(\omega+\rho)s$ into Eq. (3.20), we have

$$-B(s)=\frac{\dot{u}(s)}{r_0(\omega+\rho)}+\frac{iu(s)}{r_0}, \tag{3.30}$$

where $u(s)=\Delta u_{\rho}(s)+i\Delta u_{\phi}(s)$. The general solution of this equation is

$$u_H(s)=C_1 e^{-i(\omega+\rho)s}. \tag{3.31}$$

The particular solution of this equation is given by the integration

$$u_*(s)=-r_0(\omega+\rho)e^{-i(\omega+\rho)s}\int_0^s e^{i(\omega+\rho)t}B(t)dt. \tag{3.32}$$

Considering the boundary condition $u(1)=0,$ constant C_1 can be obtained

$$C_1 = r_0(\omega+\rho)\int_0^1 e^{i(\omega+\rho)t}B(t)dt. \tag{3.33}$$

The final solution of Eq. (3.30) should be the sum of Eqs. (3.31) and (3.32):

$$u(s) = u_*(s)+u_H(s) = r_0(\omega+\rho)e^{-i(\omega+\rho)s}\int_s^1 e^{i(\omega+\rho)t}B(t)dt. \tag{3.34}$$

Assuming $s=\rho/(\omega+\rho)$, we can get the value of $\Delta u_\rho(s)+i\Delta u_\varphi(s)$ where Δu_ρ is CTOD (δ) and Δu_φ is the relative tangential shift between the crack faces. We have

$$\frac{\delta}{r_0} = real\left((\omega+\rho)e^{-i(\omega+\rho)s}\int_s^1 e^{i(\omega+\rho)t}B(t)dt\right). \tag{3.35}$$

3.3. Numerical examples and discussions

3.3.1. Verification of the current analysis

When the plastic zones at the both crack tips are not considered, we can compare the SIF from our current method with that obtained from previous researchers to examine the derivation accuracy. In reference [32] and [108], the stress intensity factor (SIF) are given by

$$\begin{aligned} K_1+iK_2 = {} & \frac{2\sqrt{\pi\sin\omega}}{1+1/\alpha^*}\cosh(\varepsilon\pi)e^{-\varepsilon(\omega+\pi)}e^{-i\left(\omega/2-\pi/2+\varepsilon\log(2\sin\omega)\right)} \\ & \times(-i+2\varepsilon)\left\{C_1-\frac{\sigma_{yy}^{\infty}}{2}\frac{\mu_2(1+\kappa_1)}{\mu_1+\mu_2\kappa_1}e^{2\varepsilon\omega}e^{-i(\omega-\pi)}\right\}r_0^{1/2-i\varepsilon}, \end{aligned} \tag{3.36}$$

where

$$\left.\begin{aligned}
C_1 &= \frac{X_1}{2}\left\{\frac{2X_2\left(M_2-M_1^2\right)\mathrm{Re}\left[b_{0A}\right]-\sigma_{yy}^{\infty}\left[X_2/X_1\right]\left[X_2+X_1\right]}{X_1Y_1N_1e^{-2\varepsilon\omega}-Y_2\left[X_1+2X_2\right]}\right\} \\
&\quad -i\left\{\frac{X_2\left(M_2-M_1^2\right)\mathrm{Im}\left[b_{0A}\right]}{Y_2+Y_1N_1e^{-2\varepsilon\omega}}\right\}, \\
X_1 &= \mu_1(1+\kappa_2),\ X_2=\mu_2(1+\kappa_1), \\
Y_1 &= \mu_1+\mu_2\kappa_1,\ Y_2=\mu_2+\mu_1\kappa_2, \\
b_{0A} &= \left(\frac{\sigma_0}{2}\right)e^{-i\pi}, \\
M_1 &= \cos\omega-2\varepsilon\sin\omega, \\
M_2 &= \left(\left(3\cos 2\omega+1\right)/4\right)+\varepsilon^2\left(1-2\cos 2\omega\right)-2\varepsilon\sin 2\omega, \\
N_1 &= \cos\omega+2\varepsilon\sin\omega.
\end{aligned}\right\}. \tag{3.37}$$

Here, $\varepsilon=\frac{1}{2\pi}\log\left(\frac{1+\beta}{1-\beta}\right)$, σ_0 is the remote tension loading, $\kappa_j=3-4\nu_j$ in plane strain and $\kappa_j=\left(3-\nu_j\right)/\left(1+\nu_j\right), j=1,2$ in plane stress. ν_j and μ_j are the Poisson's ratio and the shear modulus of material *j* respectively.

To make the result brief and clear in logic, the following dimensionless expression of the stress intensity factor *F* is introduced [108]

$$F=F_1+iF_2=\frac{K}{\frac{\sqrt{\pi r_0\sin\omega}\left(1+2i\varepsilon\right)}{\left(2r_0\omega\right)^{i\varepsilon}}\sigma_0}, \tag{3.38}$$

where *K* is the result obtained from Eq. (3.36). F_1 and F_2 are the normalized stress intensity factor of mode I and mode II loading, respectively. The results obtained from our current method and those from Eq. (3.36) are shown in Table 3.1 and Table 3.2, which illustrate that the current results agree very well with Eq. (3.36) from reference [32] and [108].

ω°	Current work		Perlman-Sih [32]	
	F_1	F_2	F_1	F_2
15	0.9360	-0.2530	0.9360	-0.2525
30	0.7607	-0.4568	0.7604	-0.4563
45	0.5169	-0.5774	0.5163	-0.5767

Table 3.1 Comparison of SIF: An arc-shaped crack in homogeneous material without plastic zone correction ($\nu_1 = \nu_2 = 0.32$, $\mu_2 / \mu_1 = 1$)

ω°	Current work		Perlman-Sih [32]	
	F_1	F_2	F_1	F_2
15	1.1758	-0.3127	1.1761	-0.3110
30	0.9763	-0.5712	0.9765	-0.5697
45	0.6920	-0.7351	0.6922	-0.7338

Table 3.2 Comparison of SIF for an interfacial arc-shaped crack without plastic zone correction ($\nu_1 = 0.32, \nu_2 = 0.5,\ \mu_2 / \mu_1 = 2$)

3.3.2. Effect of the debonding angle (the crack size) and the shear modulus ratio (inclusion/matrix)

With the plastic zone corrections proposed in the current work, the influence of the half debonding angle ω and the shear modulus ratio μ_2 / μ_1 on the normalized SIF is discussed. The Poisson's ratios of the two material are both taken as 0.32 and μ_2 / μ_1 varies from 0.5 to 100. The half debonding angle ω is set to be 15°, 30° and 45°, respectively. The normalized SIFs for F_1 and F_2 are shown in Fig. 3.3 and Fig. 3.4, respectively.

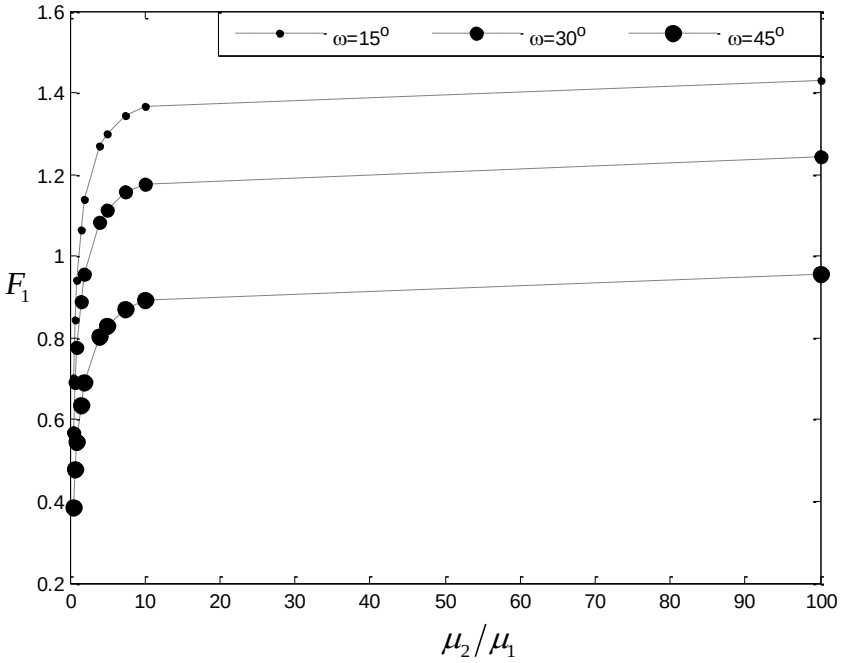

Fig. 3.3 The normalized stress intensity factor of mode I F_1 versus the shear modulus ratio μ_2/μ_1.

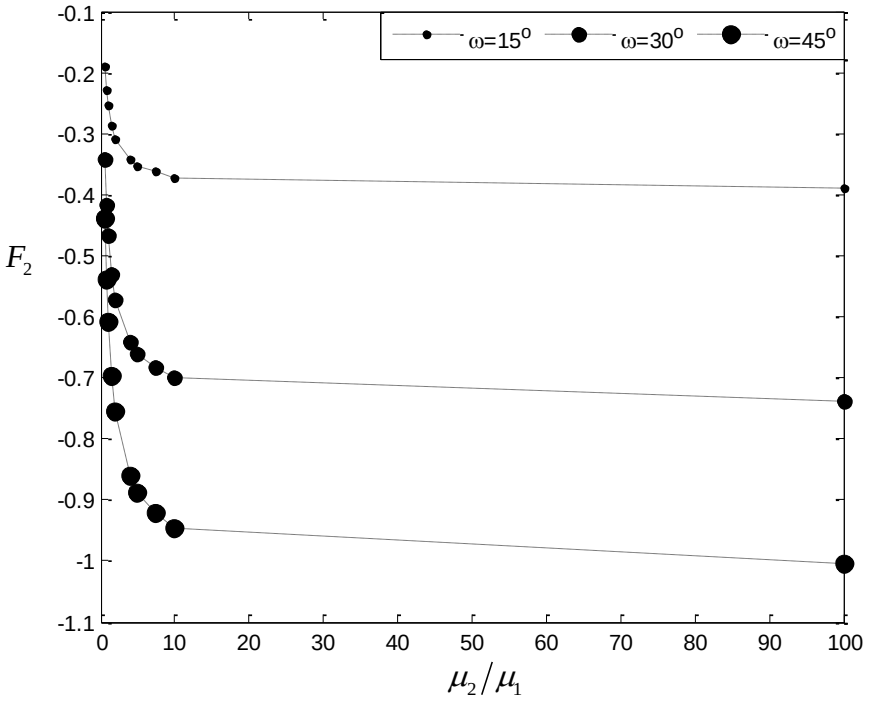

Fig. 3.4 The normalized stress intensity factor of mode II F_2 versus the shear modulus ratio μ_2/μ_1.

From Fig. 3.3 and Fig. 3.4, as the half debonding angle ω increases, both

the normalized mode I and mode II SIFs decrease. This is because the traction components depend on the debonding angle for the curved crack. Even after normalization, the influence of ω is still significant. On the effect of the shear modulus ratio, when the stiffness of the inclusion is increased, the absolute values of F_1 and F_2 both increase for any given crack length $2r_0\omega$. When the inclusion is "softer" (μ_2/μ_1 decreases or close to 1), the influence of μ_2/μ_1 is very significant. When the inclusion is much "harder" than the matrix (μ_2/μ_1 is very large), the normalized values of SIF are less sensitive to the increasing inclusion stiffness.

3.3.3. The influence of the debonding angle and the shear modulus ratio on the normalized plastic zone size and normalized CTOD

In this section, the effects of the shear modulus ratio μ_2/μ_1 and the half debonding angle ω on the normalized PZS $\rho/(\omega+\rho)$ and the normalized CTOD δ/r_0 are investigated. The normalized loading σ_0/σ_{ys} is set to be 0.1. The Poisson's ratios of the two materials are taken as 0.32 and the shear modulus ratio μ_2/μ_1 increases from 0.5 to 10. The half debonding angle ω is set to be 15°, 30° and 45°, respectively.

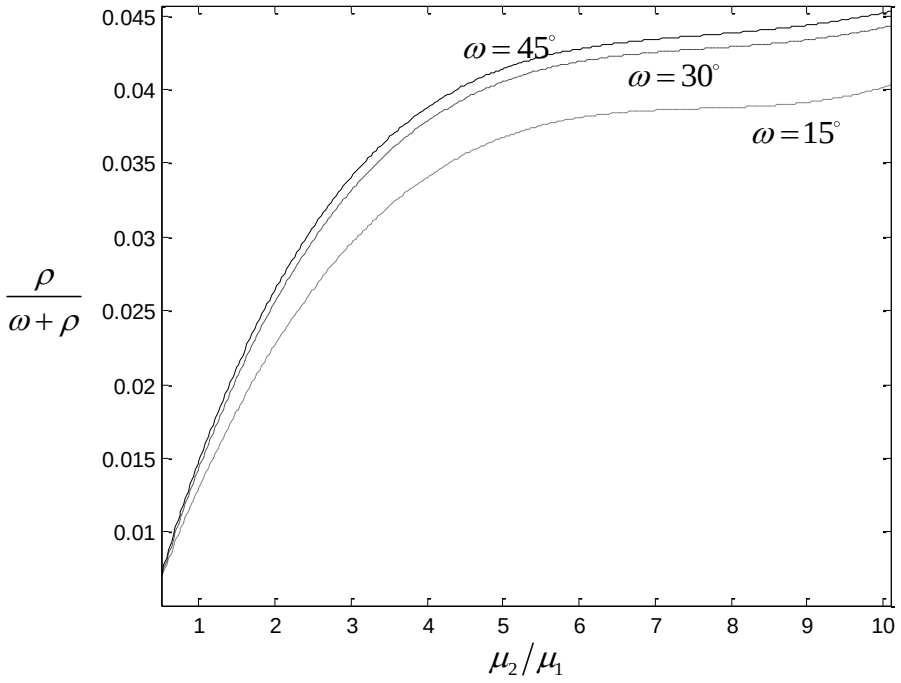

Fig. 3.5 The normalized plastic zone size $\rho/(\rho+\omega)$ versus the shear modulus ratio μ_2/μ_1.

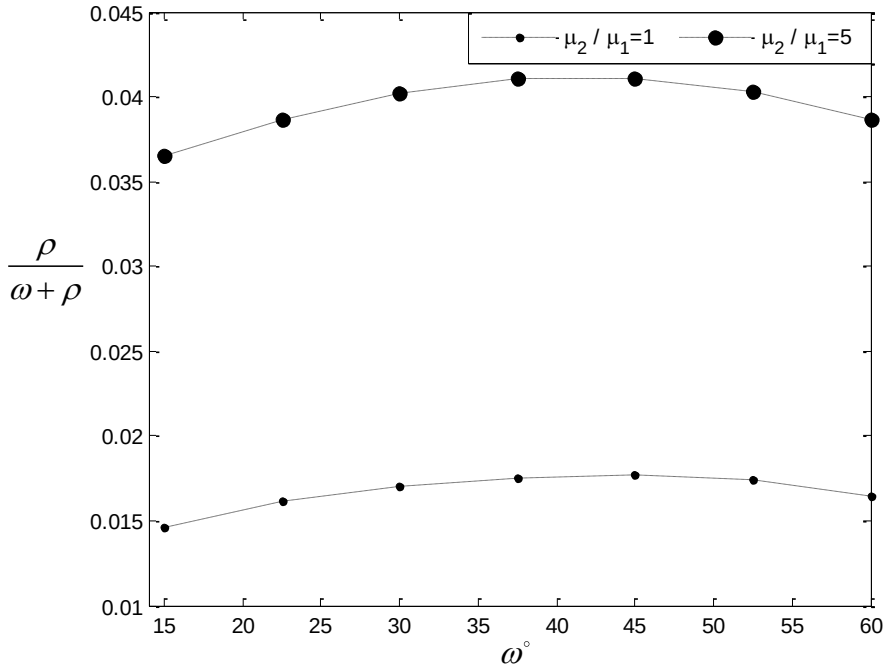

Fig. 3.6 The normalized plastic zone size $\rho/(\rho+\omega)$ versus the half debonding angle ω.

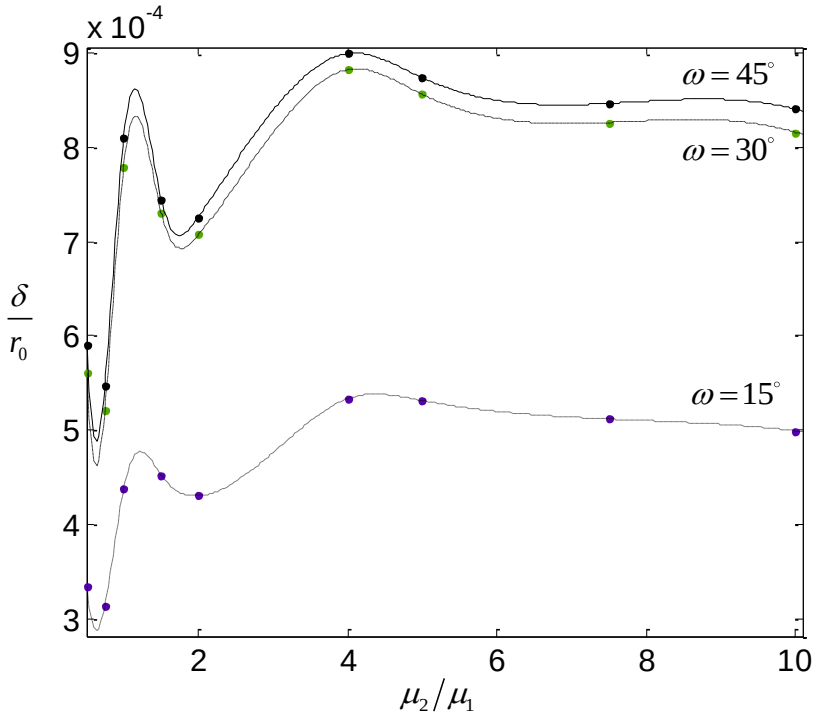

Fig. 3.7 The normalized CTOD δ / r_0 versus the shear modulus ratio μ_2 / μ_1.

From Fig. 3.5, it is observed that $\rho / (\omega + \rho)$ increases when ω various from 15° to 45°. But for each μ_2 / μ_1, the normalized PZS $\rho / (\omega + \rho)$ will get its maximum value at 45°. as shown in Fig. 3.6. It is also found from Fig. 3.5 that when μ_2 / μ_1 is small (for "softer" inclusion case), $\rho / (\omega + \rho)$ increases quickly. When the inclusion is much stiffer than the matrix (μ_2 / μ_1 is high), the slopes of these curves approach to zero slowly. We can also find from the two figures that the ratio ρ / ω has a variation between 1% ~ 1.5% with ω for homogenous cases ($\mu_2 / \mu_1 = 1$). When the debonding angle ω is very small, this value could be quite close to the value of a homogenous straight crack (about 1.2% difference). This is also an indirect verification for the current method.

The effects of the shear modulus ratio μ_2 / μ_1, and the half debonding angle ω on the normalized CTOD δ / r_0 are illustrated in Fig. 3.7. The figure shows

when ω increases, the normalized CTOD value increases accordingly. For the influence of inclusion stiffness, when the modulus ratio μ_2 / μ_1 is small, the normalized CTOD changes quickly because the stress field of the interface crack is very sensitive to the shear modulus of the materials. When the shear modulus ratio becomes large, the inclusion property dominates the stress field of the interface crack, hence the normalized CTOD becomes stable slowly.

3.3.4. Validation of the current method with hydrostatic loading

For each crack case solved, we must ensure that the crack is open ($\Delta u_\rho \geq 0$) at all points in the crack area. It is shown in Fig.3.8 when ω increases to about 77°, the normalized mode I SIF becomes negative ($F_1 < 0$) if μ_2/μ_1 is relatively small. This is physically impossible for Griffith crack problems and could result to a negative crack face displacement. The physical meaning of the result is that under uniaxial tension, the maximum debonding angle ω is less than 77°. To further study this interesting conclusion, the hydrostatic loading case is considered as shown in Fig. 3.2(b). The normalized mode I SIF is illustrated in Fig. 3.9 for this case. We can find that, up to $\omega = 150^\circ$, F_I is still positive. When $\omega = 180^\circ$, F_I becomes zero for all cases of μ_2/μ_1. It means the inclusion can be completely debonded in hydrostatic loading condition.

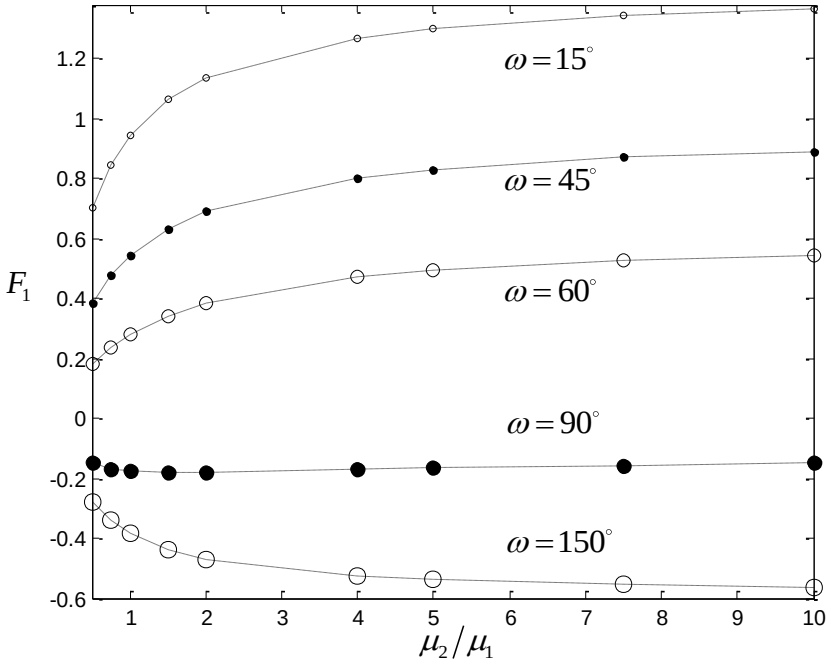

Fig. 3.8 Normalized mode I stress intensity factors of uniaxial loading (ω ups to 150°).

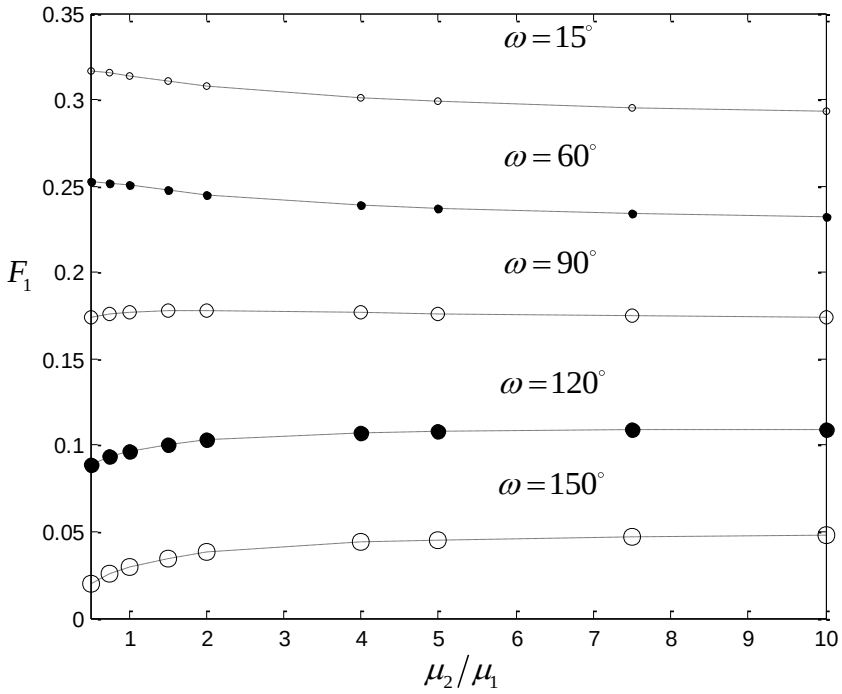

Fig. 3.9 Normalized mode I stress intensity factors under hydrostatic loading (ω ups to 150°).

3.4. Conclusions

A systematic analytical method has been developed to investigate the

elastic-plastic stress field for an arc-shaped interfacial crack between a circular inclusion and matrix. The mixed mode Dugdale model is proposed to investigate the elastic-plastic fracture behavior under remote uniform tension. The influence of the half debonding angle ω and the shear modulus ratio μ_2 / μ_1 on the normalized plastic zone size and the normalized crack tip opening displace are studied.

Our numerical examples show that the half debonding angle has great influence on the SIF, PZS and CTOD. When the ratio μ_2 / μ_1 is small than 1, which means the inclusion is "softer" than or close to the matrix, the influence of μ_2 / μ_1 on the SIF, PZS and CTOD is significant. When the ratio μ_2 / μ_1 approaches to infinity (the inclusion is rigid), the SIF, PZS and CTOD tend to be stabilized. An interesting result is that under uniaxial tension, the maximum debonding angle ω is less than 77°, which means the inclusion can be partially debonded from the matrix. Further study shows if the remote loading is hydrostatic tension, the inclusion can be completely debonded.

Chapter 4 Elastic-plastic Fracture Analysis of a Radial Crack Interacting with a Coated Circular Inclusion

4.1. Introduction

Fibers-reinforced composites have been increasingly used in various engineering structures as it can exploit beneficial characteristics of individual constituents to achieve desired overall properties. However, due to the mismatches of material properties between the matrix and the embedded phase (the fibers), high stress concentration at the interface between the two dissimilar materials is often induced, which usually causes interface cracking or fiber-matrix debonding as explored in the previous chapter. One of the efficient approaches to avoid material mismatch is to add an intermediate layer of a third material with appropriate geometry and properties between the matrix and inclusion. In other words, the inclusion is covered by a coating layer. When a coating phase is considered, the elastic-plastic problem becomes even more complicated (3 dissimilar materials involved), but more applicable to engineering practice.

In this chapter, the elastic-plastic fracture investigation for a radial Griffith crack interacting with a coated circular inclusion has been carried out. The objective is to estimate the plastic zone size and the CTOD for a crack embedded in the matrix with arbitrarily orientation angle near a coated inclusion. Numerical examples and discussions are given to show how these quantities vary with the

material properties and the crack location. The results obtained are verified by the FEM simulation.

4.2. A brief review of Irwin model

4.2.1. Generalized Irwin model for Griffith crack

The physical problem studied in this chapter is shown in Fig. 4.1, where a radial crack is located near a coated inclusion. The inclusion, coating layer and matrix are denoted by Phase 1, 2, 3, respectively. With the remote uniaxial tension, when the crack orientation angle θ is not zero, both traction components in normal and shear directions exist at the crack surfaces. The original physical problem shown in Fig. 4.1(a) is equivalent to the one in Fig. 4.1(b), where the tractions on the crack surfaces are solved from Fig. 4.1(a) when the crack vanishes.

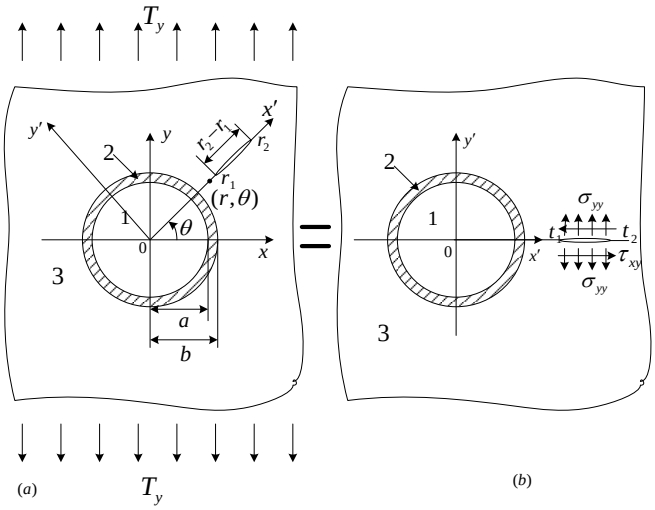

Fig. 4.1 A crack in the matrix interacts with a near-by coated circular inclusion.

The stress field ahead the crack tips is given by Anderson [13] :

$$\sigma_{xx}^{(t_m)}=\sigma_{yy}^{(t_m)}=\frac{K_I^{(t_m)}}{\sqrt{2\pi r^{(t_m)}}},\sigma_{xy}^{(t_m)}=\frac{K_{II}^{(t_m)}}{\sqrt{2\pi r^{(t_m)}}},\sigma_{zz}^{(t_m)}=\frac{2\nu_3 K_I^{(t_m)}}{\sqrt{2\pi r^{(t_m)}}},\quad m=1,2. \tag{4.1}$$

Here, (t_1) and (t_2) represent the left and right crack tips, respectively. $K_I^{(t_m)}$ and $K_{II}^{(t_m)}$ are mode I and mode II stress intensity factor near (t_m). ν_3 is the Poisson's ratio of phase 3 (the matrix phase). Plane strain condition is considered in this chapter. To estimate the plastic zone size around the crack tips, the von Mises criterion is used, in which yielding occurs when the effective stress reaches the yield stress $\sigma_e=\sigma_{ys}$. The effective stress is related to the stress components shown in Eq. (4.1) as follows:

$$\sigma_e^{(t_m)}=\sqrt{\frac{\left(\sigma_{xx}^{(t_m)}-\sigma_{yy}^{(t_m)}\right)^2+\left(\sigma_{xx}^{(t_m)}-\sigma_{zz}^{(t_m)}\right)^2+\left(\sigma_{yy}^{(t_m)}-\sigma_{zz}^{(t_m)}\right)^2+6\left(\sigma_{xy}^{(t_m)2}\right)}{2}}=\sigma_{ys}, \tag{4.2}$$

where $\sigma_e^{(t_m)}$ is the effective stress near the crack tip (t_m), σ_{ys} is the yield stress. Substituting the stress components of Eq. (4.1) into (4.2), we can get the following expression:

$$\sigma_e^{(t_m)}=\frac{\sqrt{\left(1-2\nu_3\right)^2\left(K_I^{(t_m)}\right)^2+3\left(K_{II}^{(t_m)}\right)^2}}{\sqrt{2\pi r^{(t_m)}}}. \tag{4.3}$$

Assuming that

$$K_e^{(t_m)}=\sqrt{\left(1-2\nu_3\right)^2\left(K_I^{(t_m)}\right)^2+3\left(K_{II}^{(t_m)}\right)^2}, \tag{4.4}$$

where $K_e^{(t_m)}$ is a constant related to the stress intensity factor components $K_I^{(t_m)}$ and $K_{II}^{(t_m)}$. It represents the strength of the equivalent stress fields near the crack tip along the crack line.

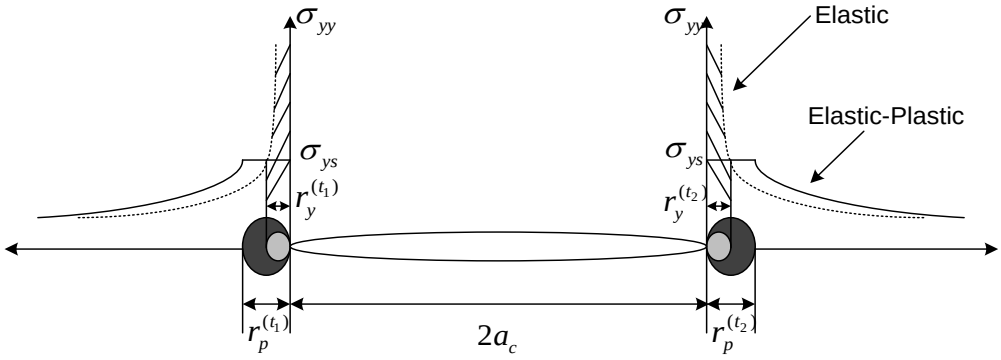

4.2(a)

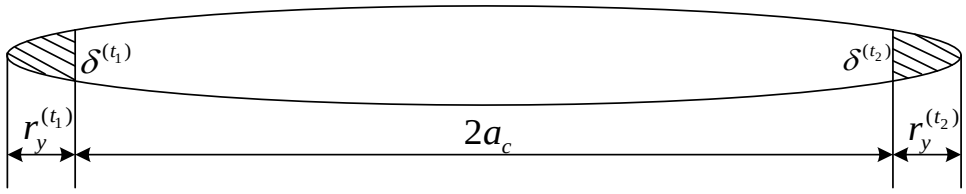

4.2(b)

Fig. 4.2 (a) The Irwin model: the plastic zones of sizes r_y and r_p ahead of a crack tip; (b) The crack tip opening displacement δ in generalized Irwin model.

Substituting Eq. (4.4) into (4.3) and letting $\sigma_e^{(t_m)} = \sigma_{ys}$, the plastic zone size is obtained as:

$$r_y^{(t_m)} = \frac{1}{2\pi}\left(\frac{K_e^{(t_m)}}{\sigma_{ys}}\right)^2. \tag{4.5}$$

This is the first-order estimation of the plastic zone size. When the stress in the cross-hatched region (shown in Fig. 4.2(a)) is considered, a second-order estimation of plastic zone size is obtained by the force balance equation:

$$\sigma_{ys} r_p^{(t_m)} = \int_0^{r_y} \sigma_e^{(t_m)} dr^{(t_m)} = \int_0^{r_y} \frac{K_e^{(t_m)}}{\sqrt{2\pi r^{(t_m)}}} dr^{(t_m)}, \tag{4.6}$$

and it leads to

$$r_p^{(t_m)} = 2r_y^{(t_m)} = \frac{1}{\pi}\left(\frac{K_e^{(t_m)}}{\sigma_{ys}}\right)^2. \tag{4.7}$$

4.2.2. Effective stress intensity factors

For the current problem, the model I and mode II stress intensity factors could be written as:

$$K_I^{(t_m)} = Y_I^{(t_m)}\left(A,B,C,D,M,\alpha,a_c,\theta\right)\sigma_0\sqrt{\pi a_c}, \tag{4.8}$$

$$K_{II}^{(t_m)} = Y_{II}^{(t_m)}\left(A,B,C,D,M,\alpha,a_c,\theta\right)\sigma_0\sqrt{\pi a_c}, \tag{4.9}$$

where $Y_I^{(t_m)}$ and $Y_{II}^{(t_m)}$ are functions of material property constants related the three phases and crack location constants. A, B, C, D, M and α are defined in the Appendix A. Constant a_c is the half-crack length, θ is the angle between the radial crack and x-axis (crack orientation angle). σ_0 is the remote loading and equals to T_y as shown in Fig. 4.1.

In section 4.2.1, the plastic zone size $r_y^{(t_m)}$ is obtained. For small scale yielding, the effective crack length is defined by:

$$a_c^{eff,(t_m)} = a_c + r_y^{(t_m)}. \tag{4.10}$$

Substituting Eq. (4.10) into (4.8) and (4.9), the effective stress intensity factors can be expressed as:

$$K_I^{eff,(t_m)} = Y_I^{eff,(t_m)}\left(A,B,C,D,M,\alpha,\frac{1}{2}\sum_m a_c^{eff,(t_m)},\theta\right)\sigma_0\sqrt{\frac{\pi}{2}\sum_m a_c^{eff,(t_m)}}, \tag{4.11}$$

$$K_{II}^{eff,(t_m)} = Y_{II}^{eff,(t_m)}\left(A,B,C,D,M,\alpha,\frac{1}{2}\sum_m a_c^{eff,(t_m)},\theta\right)\sigma_0\sqrt{\frac{\pi}{2}\sum_m a_c^{eff,(t_m)}}. \tag{4.12}$$

4.3. Formulation of the current physical problem

4.3.1. Singular integral equations of the problem

As illustrated in Fig. 4.1, the current physical problem to be investigated is

on the interaction between a coated circular inclusion and an arbitrarily oriented radial crack. Three dissimilar material phases are involved. Phase 1 is the circular inclusion with material properties κ_1 and μ_1, occupies the region $r < a$ while the coating layer (phase 2, properties κ_2 and μ_2) occupies $a < r < b$. The matrix (phase 3, properties κ_3 and μ_3) occupies the area in $r > b$. The crack orientation angle is denoted by θ. Uniaxial loading T_y is applied at infinity. By taking coordinate transformation from the $x0y$ system in Fig. 4.1(a) to $x'0y'$ system in Fig. 4.1(b), it can be found that both normal and shear tractions exist on the crack faces, which depend on the crack location parameters t_1, t_2 and θ ($t_1 = r_1, t_2 = r_2$) under loading T_y.

Distributed dislocation method is used to formulate the crack problem. The singular integral equation is given [14]:

$$\begin{cases} \sigma_{yy}(x) = -\dfrac{2\mu_3}{(\kappa_3+1)\pi}\left[\displaystyle\int_{t_1}^{t_2}\frac{B_y(\xi)}{\xi - x}d\xi + \int_{t_1}^{t_2} k_1(x,\xi)B_y(\xi)d\xi\right], \quad t_1 \le x \le t_2 \\ \sigma_{xy}(x) = -\dfrac{2\mu_3}{(\kappa_3+1)\pi}\left[\displaystyle\int_{t_1}^{t_2}\frac{B_x(\xi)}{\xi - x}d\xi + \int_{t_1}^{t_2} k_2(x,\xi)B_x(\xi)d\xi\right], \quad t_1 \le x \le t_2 \end{cases} \tag{4.13}$$

where the kernels $k_1(x,\xi)$ and $k_2(x,\xi)$ are:

$$\begin{aligned} k_1(x,\xi) = {} & \frac{C+D}{2\left(x - b^2/\xi\right)} + C\frac{\xi^2 - b^2}{\xi^3}\frac{b^2}{\left(x - b^2/\xi\right)^2}?\left[\left(\frac{\xi}{b}\right)^2 - \frac{\xi^2 - b^2}{x\xi - b^2}\right] \\ & - \frac{C+D}{2x} - \frac{1-CD}{2(1-C)}a_0\frac{b}{x^2} - \frac{1}{2\xi}\left(\frac{b}{x}\right)^2\left[2C\left(\frac{\xi}{\beta}\right)^2 - C - 1\right] \\ & + \frac{1-CD}{2b(1-D)}\left[\sum_{n=1}^{\infty} n a_{-n}\left(\frac{b}{x}\right)^n - \sum_{n=1}^{\infty}(n+1)a_{-n}\left(\frac{b}{x}\right)^{n+2}\right] - C\frac{b^2}{x^3} \\ & - \frac{1-CD}{b(1-D)}\sum_{n=1}^{\infty} a_{-n}\left(\frac{b}{x}\right)^n - \frac{1-CD}{2b(1-C)}\sum_{n=1}^{\infty} a_n\left(\frac{b}{x}\right)^{n+2}, \end{aligned} \tag{4.14}$$

$$k_2(x,\xi)=\frac{C+D}{2\left(x-b^2/\xi\right)}+C\frac{b^2}{\left(x-b^2/\xi\right)^2}?\left[\frac{x-\xi}{\xi^2}\frac{\xi^2-b^2}{x\xi-b^2}\right]-\frac{C+D}{2x}$$
$$-\frac{1-C}{2\xi}\left(\frac{b}{x}\right)^2+\frac{1-CD}{2(1-C)}a_0'\frac{b}{x^2}+C\frac{b^2}{x^3}+\frac{1-CD}{2b(1-C)}\sum_{n=1}^{\infty}a_n'\left(\frac{b}{x}\right)^{n+2} \quad (4.15)$$
$$+\frac{1-CD}{2b(1-D)}\left[\sum_{n=1}^{\infty}na_{-n}'\left(\frac{b}{x}\right)^n-\sum_{n=1}^{\infty}(n+1)a_{-n}'\left(\frac{b}{x}\right)^{n+2}\right].$$

Here, the real coefficients a_n, a_n', b_n and b_n' are determined by the equations shown in Appendix A1. C and D are material property constants given in Appendix A1. $B_x(\xi)$ and $B_y(\xi)$ are dislocation densities. $\sigma_{yy}(x)$ and $\sigma_{xy}(x)$ are traction components on the crack faces due to the external uniaxial tensile loading. In the current problem, they are in the forms of:

$$\sigma_{yy}(x,\theta)=\frac{\sigma_0}{2}\left[1+\frac{\mu_3}{\lambda_3+\mu_3}\frac{b^2}{x^2}a_4+\left(1-3b_7\frac{b^4}{x^4}\right)\cos(2\theta)\right], \quad (4.16)$$

$$\sigma_{xy}(x,\theta)=\frac{\sigma_0}{2}\left(1+3b_7\frac{b^4}{x^4}+2b_8\frac{b^2}{x^2}\right)\sin(2\theta), \quad (4.17)$$

where μ_3 and λ_3 are material property constants of phase 3 given in Appendix A2. The unknown coefficients a_4, b_7 and b_8 can be obtained by solving the equations (A.5) and (A.6).

The dislocation densities $B_x(x)$ and $B_y(x)$ must satisfy the condition of zero-net-dislocation along the crack:

$$\int_{t_1}^{t_2}B_x(\xi)d\xi=0,\ \int_{t_1}^{t_2}B_y(\xi)d\xi=0. \quad (4.18)$$

The dislocation densities $B_x(x)$ and $B_y(x)$ can be obtained by solving the integral equations (4.13) numerically [80]. With the dislocation density solutions, the mode I and mode II stress intensity factors on the left and right crack tips are then given by Weertman [15]:

$$
\begin{aligned}
K_I^{(t_1)} &= -\frac{2\mu_3\sqrt{\pi\left(t_2-t_1\right)/2}}{\kappa_3+1}F_y\left(-1\right)= -\sigma_0\sqrt{\pi\left(t_2-t_1\right)/2}F_{0y}\left(-1\right),\\
K_I^{(t_2)} &= \frac{2\mu_3\sqrt{\pi\left(t_2-t_1\right)/2}}{\kappa_3+1}F_y\left(1\right)= \sigma_0\sqrt{\pi\left(t_2-t_1\right)/2}F_{0y}\left(1\right),\\
K_{II}^{(t_1)} &= -\frac{2\mu_3\sqrt{\pi\left(t_2-t_1\right)/2}}{\kappa_3+1}F_x\left(-1\right)= -\sigma_0\sqrt{\pi\left(t_2-t_1\right)/2}F_{0x}\left(-1\right),\\
K_{II}^{(t_2)} &= \frac{2\mu_3\sqrt{\pi\left(t_2-t_1\right)/2}}{\kappa_3+1}F_x\left(1\right)= \sigma_0\sqrt{\pi\left(t_2-t_1\right)/2}F_{0x}\left(1\right).
\end{aligned}
\tag{4.19}
$$

Here, $K_I^{(t_m)}, K_{II}^{(t_m)}, (m=1,2)$ represent the mode I and mode II stress intensity factors, respectively. $F_{0x}(s)$ and $F_{0y}(s)$ can be obtained by setting $\frac{\kappa_3+1}{2\mu_3}\sigma_0=1$.

4.3.2. Crack tip opening displacement (CTOD).

The expression of CTOD due to Irwin Model (shown in Fig. 4.2(b)) takes the form [13] :

$$\delta^{(t_m)} = \frac{8}{E'}K_I^{(t_m)}\sqrt{\frac{r_y^{(t_m)}}{2\pi}}, \tag{4.20}$$

where $E'=E_3\Big/\left(1-\nu_3^2\right)$ in plane strain. E_3 and ν_3 are Young's modulus and Poisson's ratio of phase 3 (the matrix). Substituting Eq. (4.5) into (4.20), we can have the CTOD as:

$$\delta^{(t_m)} = \frac{4}{\pi}\frac{K_I^{(t_m)}K_e^{(t_m)}}{E'\ \sigma_{ys}}. \tag{4.21}$$

4.4. Numerical examples and discussions

The parameters affecting the elastic-plastic fracture behavior of the current problem include the coating thickness, the crack-inclusion distance (distance between the left crack tip and the inclusion center) and the material properties of

the three phases (inclusion, coating and matrix). In this section, the influence of those parameters on the SIF, the PZS and the CTOD are studied. Since the effect of the coated inclusion on the closer tip of the crack (the left crack tip) is stronger [42], only the results of the left crack tip are presented in this chapter. All the results are obtained by assuming $\nu_1 = \nu_2 = \nu_3 = 1/3$.

4.4.1. Effect of the crack orientation angle

To examine the influence of the angle θ between the crack line and *x*-axial, the inclusion is set to be stiffer than the matrix, testing the coating phase for the cases $\mu_1 > \mu_2 > \mu_3$ and $\mu_2 > \mu_1 > \mu_3$. The other parameters are set as: $\mu_2/\mu_3 = 2, 10, 25$, $\mu_1/\mu_3 = 10$, $b/a_c = 4$, $b/a = 1.1$ and $t_1/a_c = 5$ while the angle θ is varied.

To get the normalized values of the stress intensity factor, the plastic zone size and the CTOD, we use:

$$K_0 = \sigma_0\sqrt{\pi a_c},\ r_{y0} = \frac{\left(K_0^e\right)^2}{2\pi\sigma_{ys}^2},\ \delta_{y0} = \frac{4K_0K_0^e}{\pi E'\sigma_{ys}}, \tag{4.22}$$

which are the SIF, PZS and CTOD for the homogeneous case when all the 3 materials are the same and $\theta = 0$. Here, $K_0^e = (1-2\nu_3)K_0$ is obtained from Eq. (4.4) for plane strain condition.

Figures 4.3(a)-4.3(d) show the curves of the normalized mode I and mode II stress intensity factors ($K_I^{(t_1)}/K_0$ and $K_{II}^{(t_1)}/K_0$), the normalized plastic zone size ($r_y^{(t_1)}/r_{y0}$) and the normalized CTOD ($\delta^{(t_1)}/\delta_{y0}$), respectively. It is observed that the normalized mode II stress intensity factor is symmetric around $\theta = 45^\circ$. When

θ increases from 0 to 90°, the normalized mode I stress intensity factor decreases accordingly. In the cases of the normalized plastic zone size and the normalized CTOD, the figures show that both values increase when θ is small and decrease when θ is large (close to 90°). We find that the influence of the shear modulus ratio μ_2/μ_3 is smaller than the influence of angle θ.

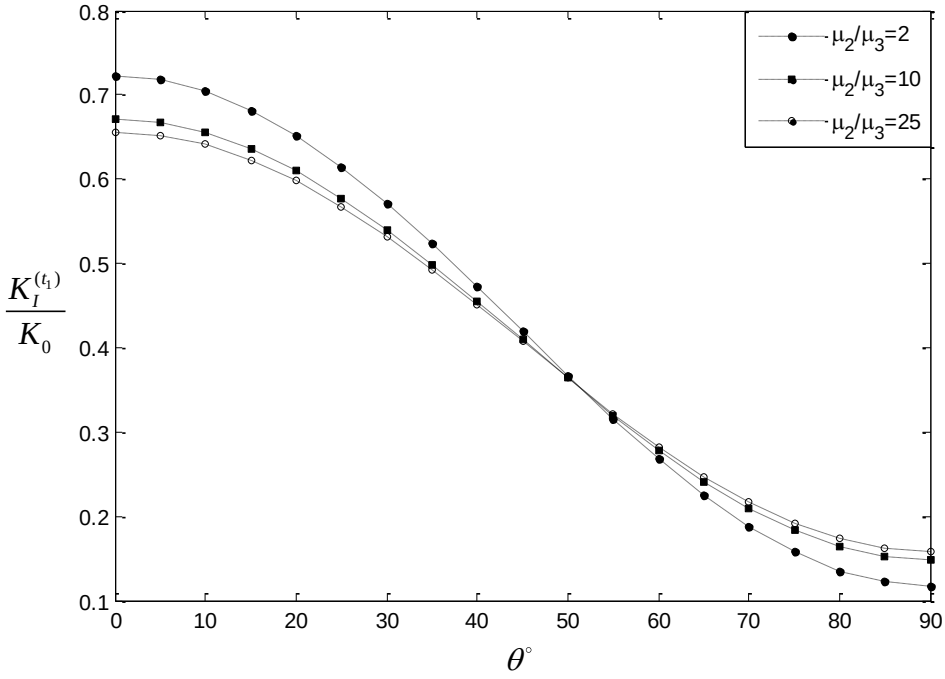

4.3(a)

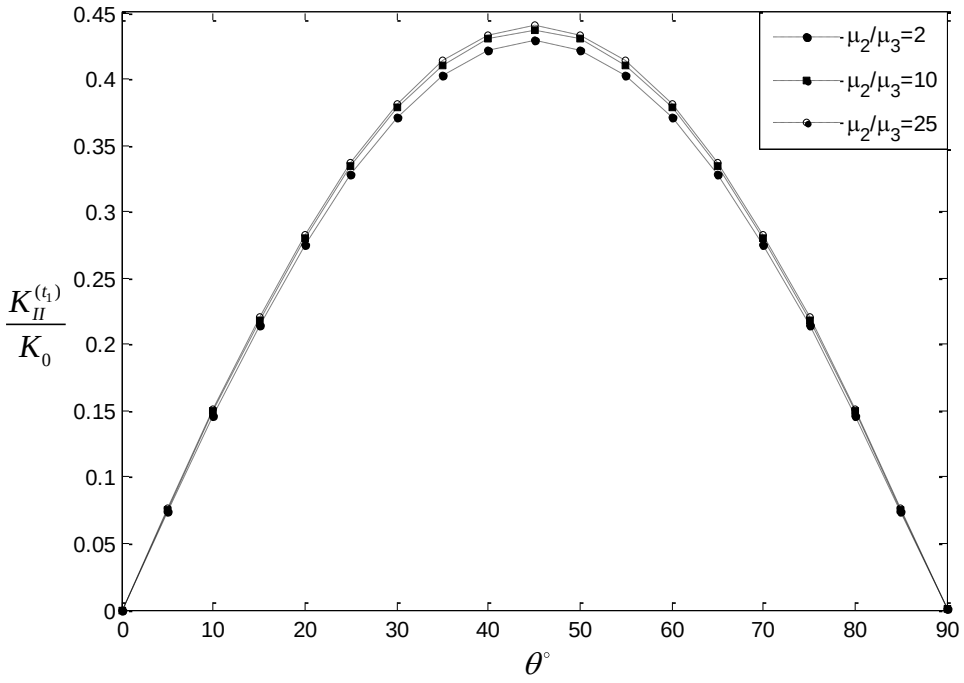
$\frac{K_{II}^{(t_1)}}{K_0}$
θ°
μ2/μ3=2
μ2/μ3=10
μ2/μ3=25

4.3(b)

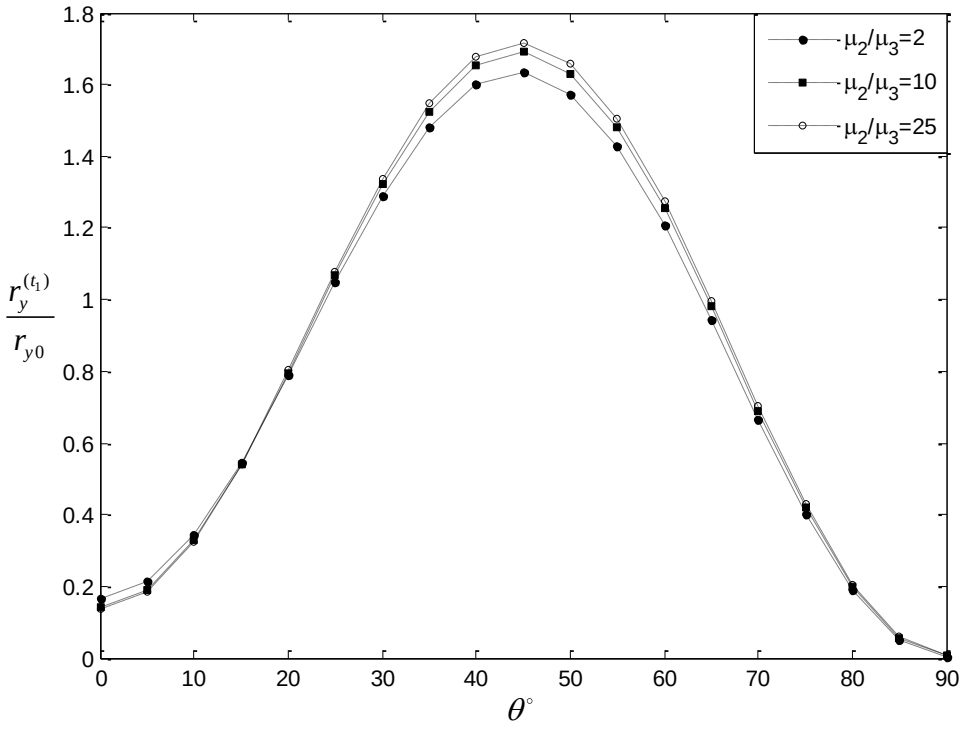
$\frac{r_y^{(t_1)}}{r_{y0}}$
θ°
μ2/μ3=2
μ2/μ3=10
μ2/μ3=25

4.3(c)

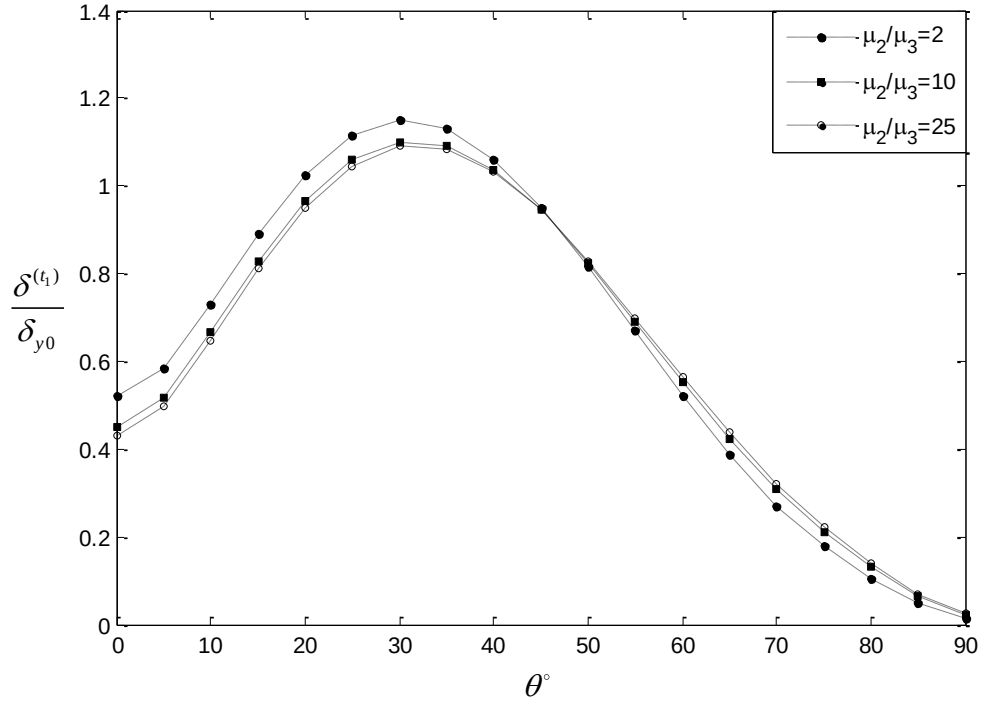

4.3(d)

Fig. 4.3 Effect of the crack orientation angle on the SIFs, PZS and CTOD with $\mu_1/\mu_3=10$, $b/a_c=4$, $b/a=1.1$ and $t_1/a_c=5$: (a) The normalized mode I SIF at the left crack tip; (b) The normalized mode II SIF at the left crack tip; (c) The normalized PZS at the left crack tip; (d) The normalized CTOD at the left crack tip.

4.4.2. Effect of the crack-inclusion distance

To examine the influence of the crack-inclusion distance (the distance between the left crack tip and the inclusion center), other parameters are set as: $\mu_2/\mu_3=2,10,25,\quad \mu_1/\mu_3=10$, $b/a_c=4$ and $b/a=1.1$ while the normalized crack distance t_1/a_c is varied. The crack orientation angle is set to be $\theta=30^\circ$.

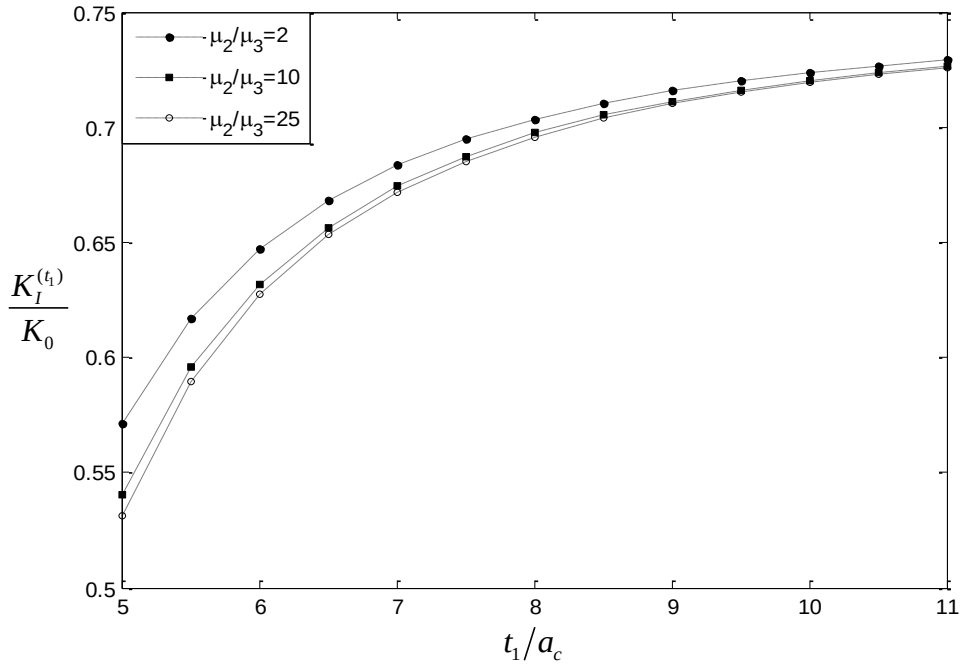
μ2/μ3=2
μ2/μ3=10
μ2/μ3=25
0.75
0.7
0.65
0.6
0.55
0.5
5
6
7
8
9
10
11
$\frac{K_I^{(t_1)}}{K_0}$
t_1/a_c

4.4(a)

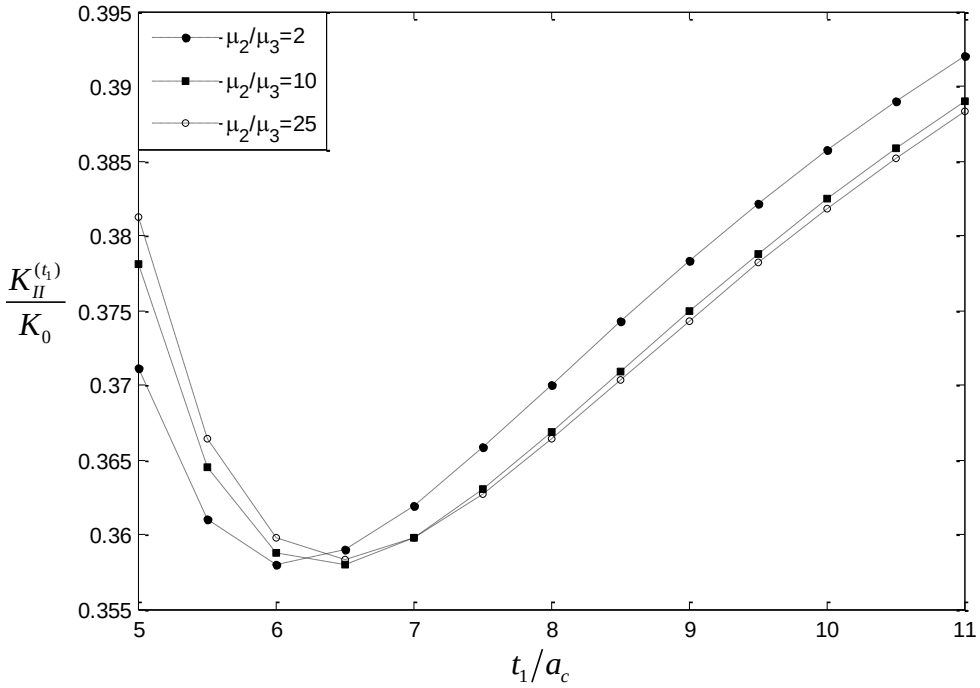
μ2/μ3=2
μ2/μ3=10
μ2/μ3=25
0.395
0.39
0.385
0.38
0.375
0.37
0.365
0.36
0.355
5
6
7
8
9
10
11
$\frac{K_{II}^{(t_1)}}{K_0}$
t_1/a_c

4.4(b)

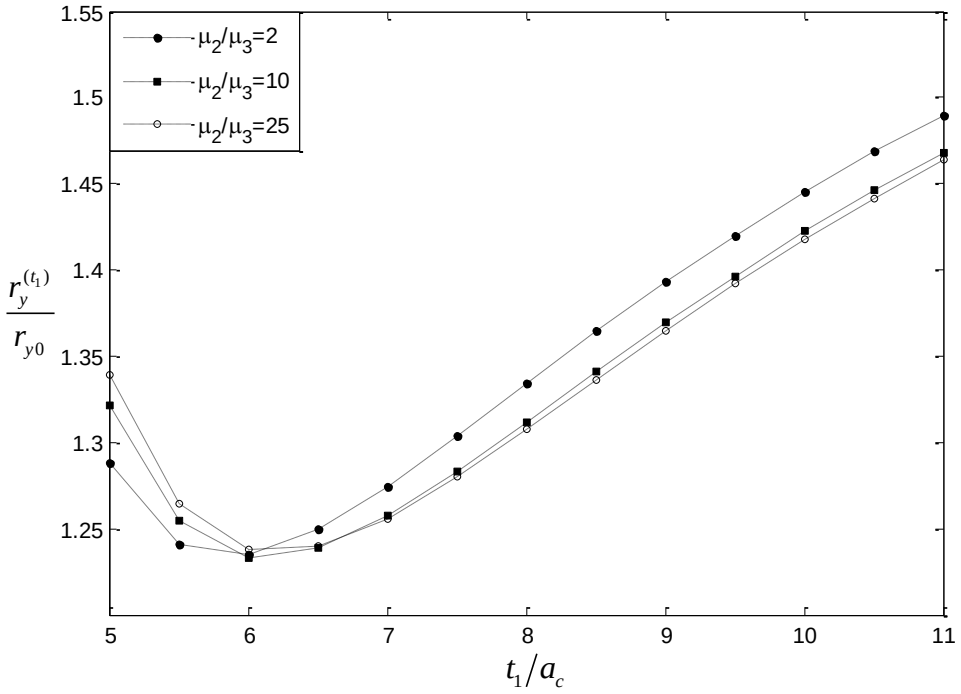

4.4(c)

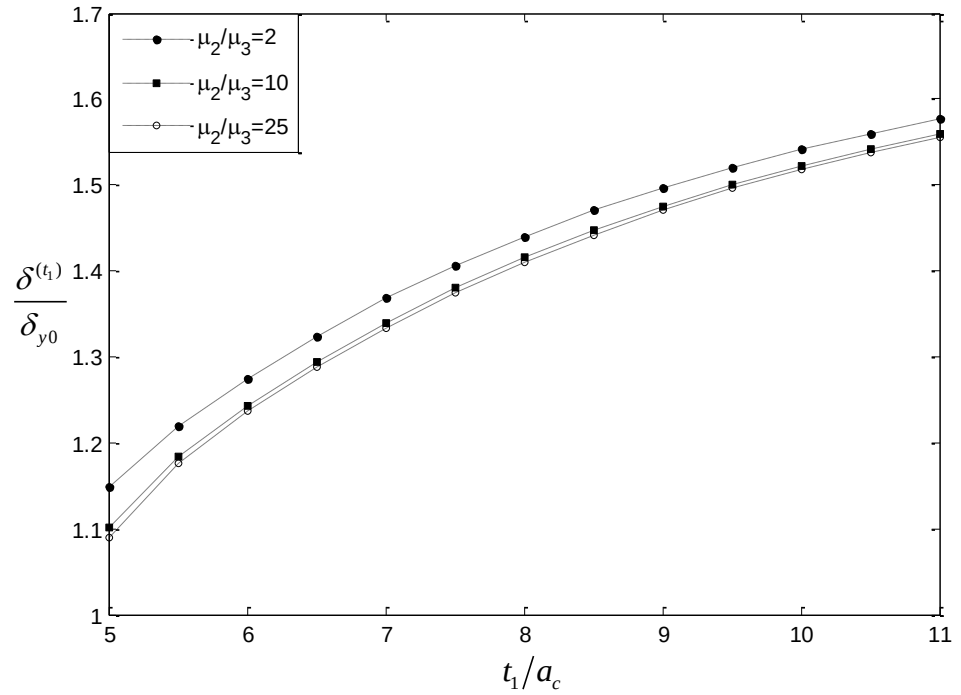

4.4(d)

Fig. 4.4 Effect of the crack distance on SIFs, PZS (Plastic Zone Size) and CTOD: with $\theta = 30^\circ$, $\mu_1/\mu_3 = 10$, $b/a_c = 4$ and $b/a = 1.1$: (a) The normalized mode I SIF at the left crack tip; (b) The normalized mode II SIF at the left crack tip; (c) The normalized PZS ahead of the left crack tip; (d) The normalized CTOD at the left crack tip.

The curves of the normalized stress intensity factor $K_I^{(t_1)} / K_0$, the normalized

plastic zone size ($r_y^{(t_1)} / r_{y0}$) and the normalized CTOD ($\delta^{(t_1)} / \delta_{y0}$) are depicted in Figs. 4.4(a)-4.4(d). We can find from the figures when the distance between the left crack tip and the inclusion center increase, the effect of the inclusion is less felt, the normalized mode I stress intensity factor and normalized CTOD will increase. But when the crack is closer to the inclusion, the values increase quickly, and while farther away, the corresponding values increase slower. The normalized mode II stress intensity factor and the normalized plastic zone size will decrease first and then increase with the increasing value of t_1/a_c. For the shear modulus ratio, the normalized mode I stress intensity factor and normalized CTOD decreases with the increasing value of μ_2/μ_3.

4.4.3. Effect of the coating phase thickness

To examine the influence of the coating phase thickness b, other parameters are set as: $\mu_2/\mu_3 = 2, 10, 25$, $\mu_1/\mu_3 = 10$, $t_1/a_c = 7.8$, $a/a_c = 4$ and $\theta = 30^\circ$. The ratio b/a_c is varied. The curves of the normalized stress intensity factor (mode I and mode II), the normalized plastic zone size and the normalized CTOD are given in Figs. 4.5(a)-4.5(d). It is found that with increasing b (the coating phase thickness), the normalized mode I stress intensity factor and the normalized CTOD decrease, while the normalized mode II stress intensity factor and the normalized plastic zone size increase.

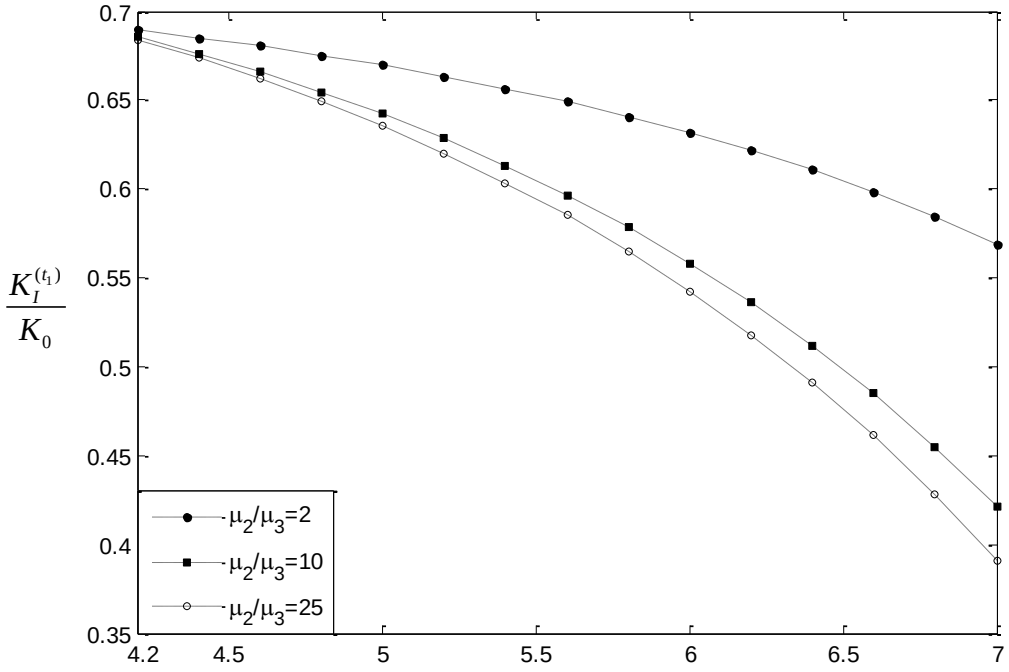
0.7
0.65
0.6
0.55
0.5
0.45
0.4
0.35
4.2
4.5
5
5.5
6
6.5
7
μ2/μ3=2
μ2/μ3=10
μ2/μ3=25
$\frac{K_I^{(t_1)}}{K_0}$
b/a_c

4.5(a)

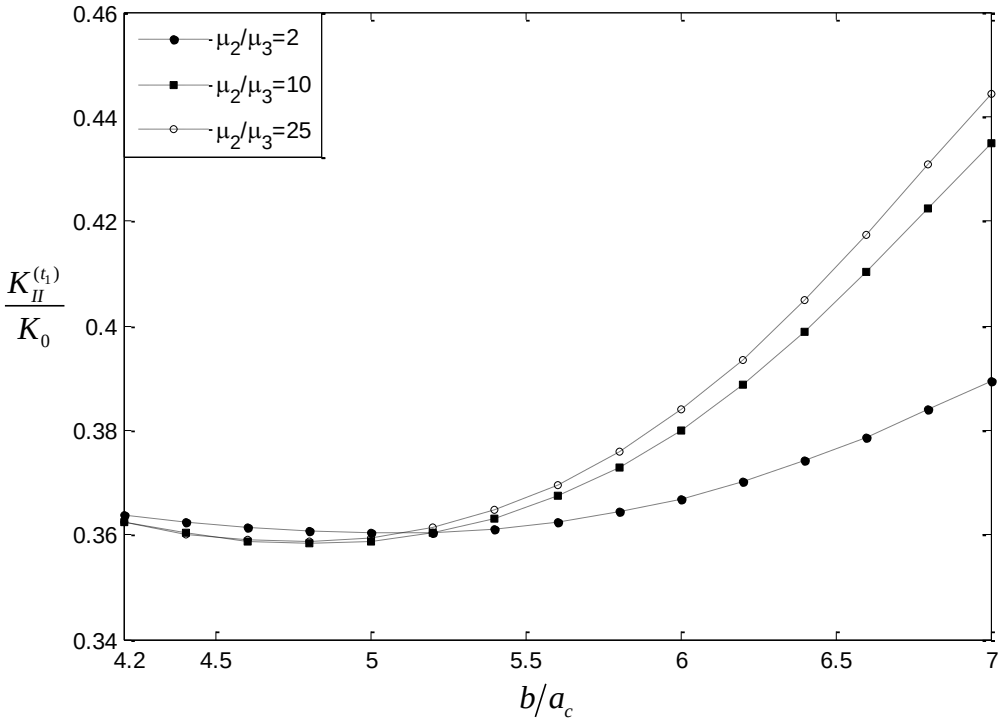
0.46
0.44
0.42
0.4
0.38
0.36
0.34
4.2
4.5
5
5.5
6
6.5
7
μ2/μ3=2
μ2/μ3=10
μ2/μ3=25
$\frac{K_{II}^{(t_1)}}{K_0}$
b/a_c

4.5(b)

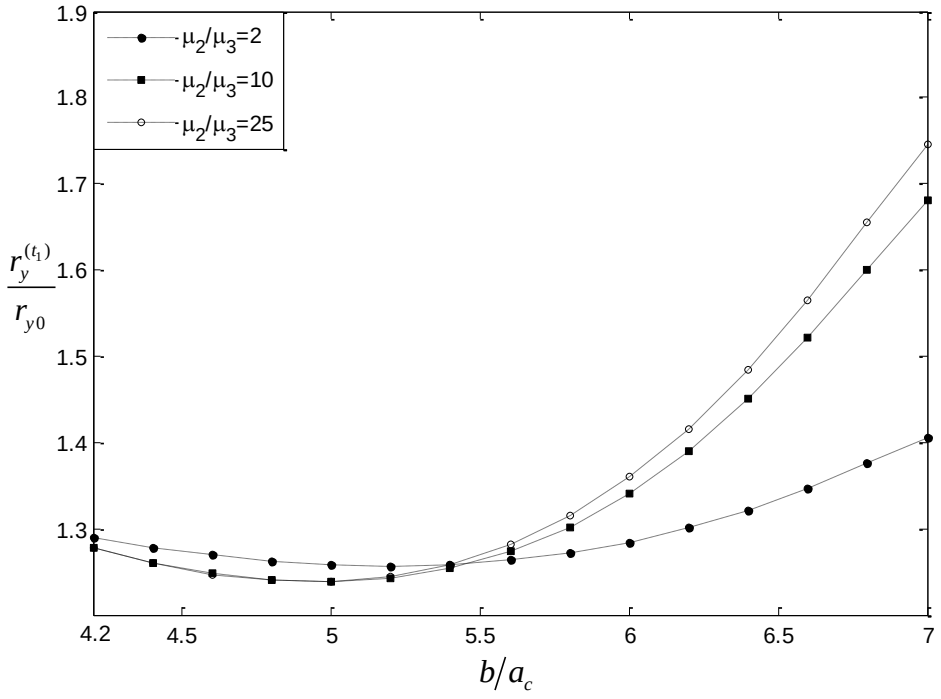

4.5(c)

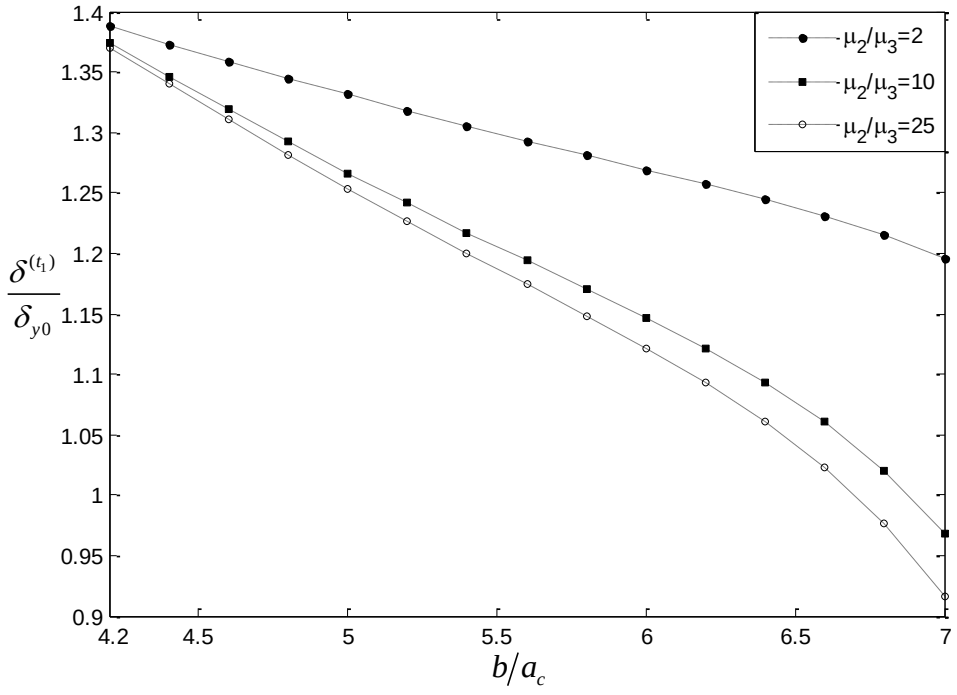

4.5(d)

Fig. 4.5 Effect of the coating phase thickness on SIFs, PZS (Plastic Zone Size) and CTOD: with $\mu_1/\mu_3 = 10,\quad t_1/a_c = 7.8,\ a/a_c = 4$ and $\theta = 30^\circ$: (a) The normalized mode I SIF at left crack tip; (b) The normalized mode II SIF at the left crack tip; (c) The normalized PZS ahead of the left crack tip; (d) The normalized CTOD at the left crack tip.

4.4.4. Effective stress intensity factors

Equations (4.11) and (4.12) present a way to get the effective stress intensity factors. When the plastic zone size $r_y^{(t_m)}$ is obtained, the effective half crack length $a_c^{eff,(t_m)}$ is given in Eq. (4.10). Then the effective stress intensity factor is obtained by resolving the singular integral equations with the effective half crack length.

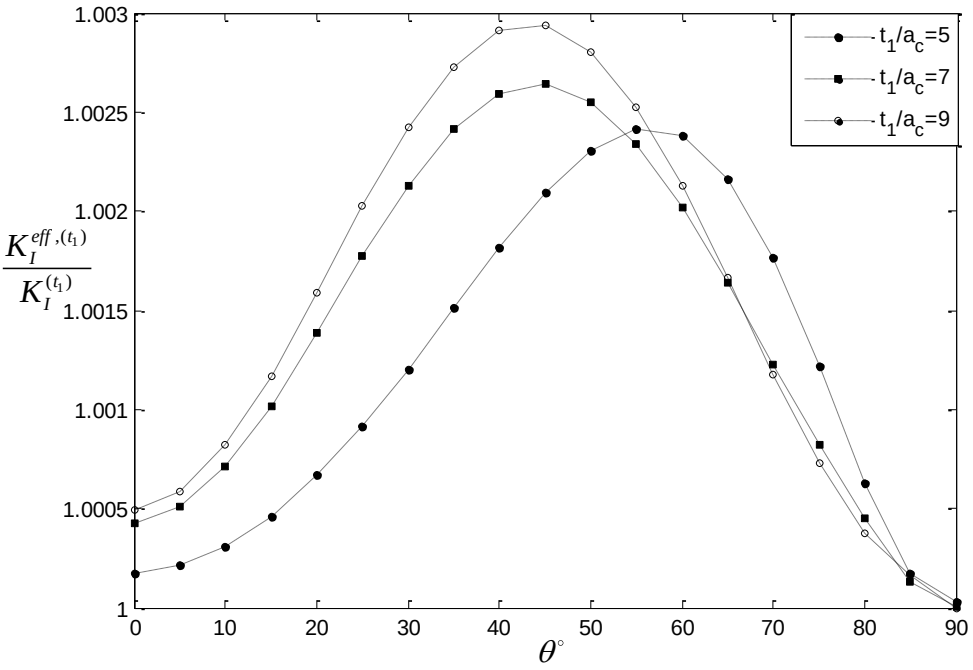

4.6(a)

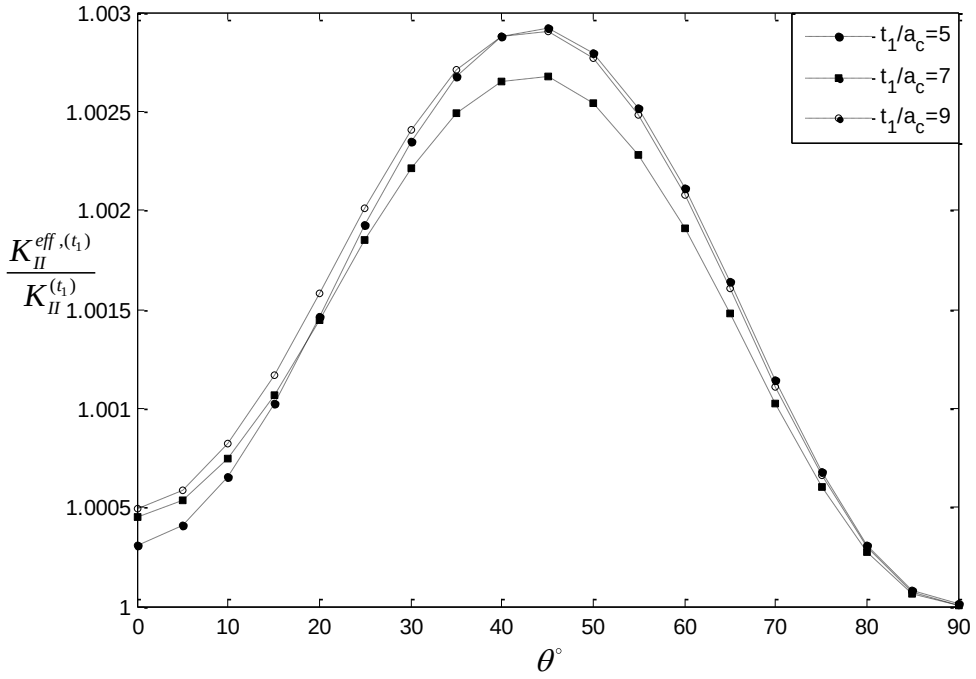

4.6(b)

Fig.4.6 Variation of the effective stress intensity factors with θ when $\mu_1/\mu_3 = \mu_2/\mu_3 = 10$, $b/a_c = 4$, and $b/a = 1.1$: (a) Effective stress intensity factor (mode I) at the left crack tip; (b) Effective stress intensity factor (mode II) at the left crack tip.

Figs. 4.6(a) and 4.6(b) show the variation of the normalized effective stress intensity factors with the angle θ. $K_I^{(t_1)}$ and $K_{II}^{(t_1)}$ are the stress intensity factors without considering the plastic zone size. The other parameters are set as: $\mu_2/\mu_3 = \mu_1/\mu_3 = 10$, $b/a_c = 4$, $b/a = 1.1$ and $t_1/a_c = 5, 7, 9$. We can find that the normalized effective stress intensity factors ($K_I^{eff,(t_1)}/K_I^{(t_1)}$ and $K_{II}^{eff,(t_1)}/K_{II}^{(t_1)}$) increase first and then decrease with the increasing θ.

4.4.5. Validation checking by finite element method

In this section, an independent finite element analysis using Abaqus is performed to study the elastic-plastic fracture behaviors of the current problem.

By using Abaqus 6.9.2, the mesh model of the coated inclusion and the matrix is shown in Fig. 4.7(a). The geometrical parameters are taken as: the inclusion center, $(-50,0)$, the left crack tip, $(50,0)$, and the right crack tip, $(70,0)$. The radius $a=50$ and $b=80$. The 8-node CPS8R element type is employed.

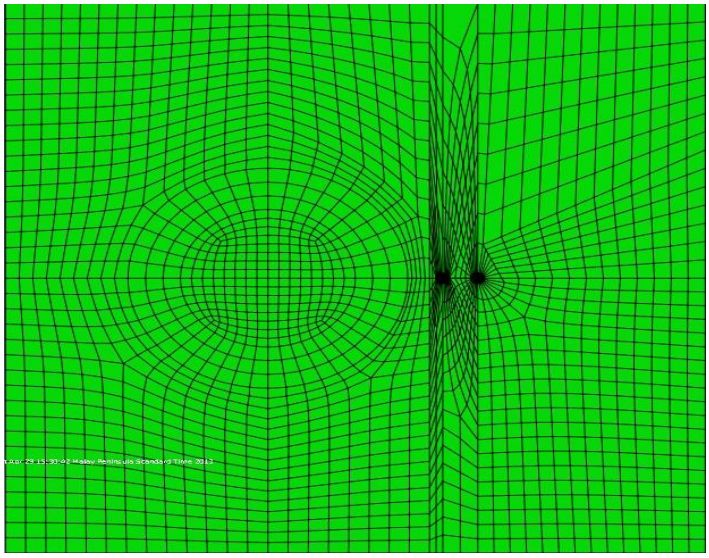

4.7(a)

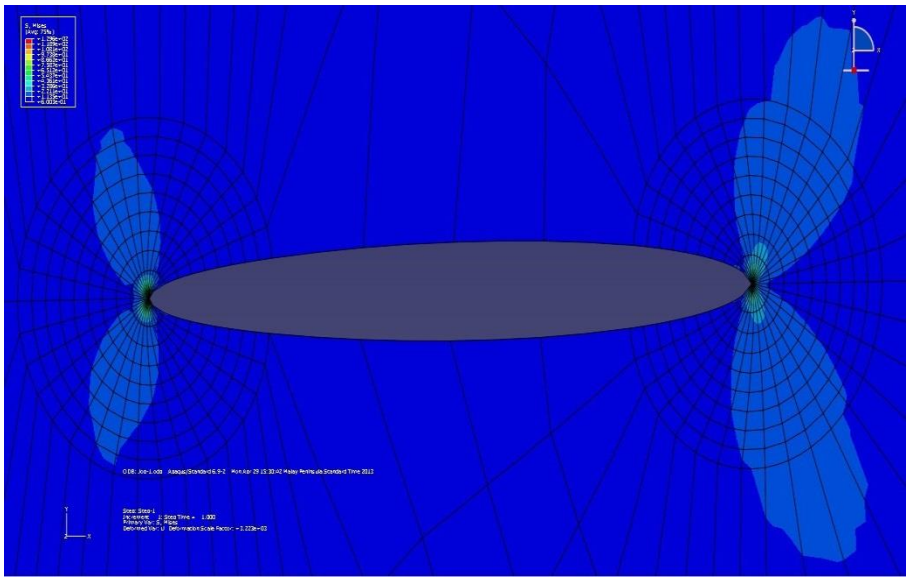

4.7(b)

Fig. 4.7 (a) The FM model for a crack near a coated circular inclusion; (b) The deformation fields near the crack tips.

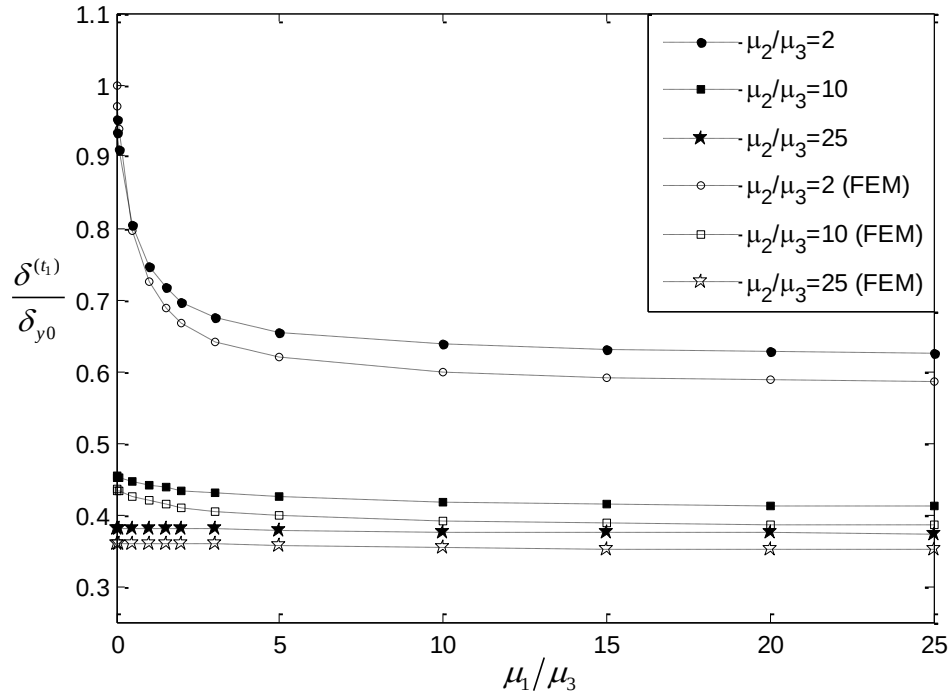

Fig. 4.8 Comparisons of the normalized CTOD between the current method and the finite element method for the case of θ=0.

The material property constants are set as: $\nu_1 = \nu_2 = \nu_3 = 0.3$, $\mu_2/\mu_3 = 2,10,25$ and μ_1/μ_3 varies from 0.01 to 25. The loading ratio is $\sigma_0/\sigma_{ys} = 0.1 \text{and} \theta = 0$. Fig. 4.7(b) shows the deformation in front of crack tips from the FEM result. It can be found from Fig. 4.8 that the values of the normalized CTOD obtained by the analytic method match those obtained by the FEM.

4.5. Conclusions

In this chapter, the elastic-plastic fracture behavior of a coated circular inclusion interacting with an arbitrarily oriented radial crack has been investigated with a generalized Irwin plastic zone correction. In the numerical examples, the influence of various parameters on the normalized SIF, the

normalized PZS and the normalized CTOD are studied in detail. Considering the condition that the coating layer and the inclusion are stiffer than the matrix, some useful conclusion marks are obtained as following:

1. The normalized mode I stress intensity factor always decreases with the increasing value of θ (the crack orientation angle), and the normalized mode II stress intensity factor is symmetric around $\theta = 45^{\circ}$. The normalized plastic zone size and the normalized CTOD increase first and then decrease with the increasing θ.

2. With the increasing t_1/a_c (the normalized distance from the left crack tip to the inclusion center), the normalized mode I stress intensity factor and the normalized CTOD increase, while the normalized mode II stress intensity factor and the normalized plastic zone size decrease first and then increase.

3. With the increasing b/a_c (the coating phase thickness normalized by the inclusion radius), the normalized mode I stress intensity factor and the normalized CTOD decrease, while the normalized mode II stress intensity factor and the normalized plastic zone size increase.

4. The validation result shows that the values of the normalized CTOD obtained by the FEM and the current method match well with each other.

Chapter 5 A Zener-Stroh Crack Interacting with a Coated Inclusion with Generalized Irwin Plastic Zone Correction

5.1. Introduction

In Chapter 4, the fracture investigation for a Griffith crack interacting with a coated inclusion has been carried out. The problem is now extended to the case of a Zener-Stroh crack interacting with a coated inclusion. Zener-Stroh crack is another mechanism of crack types which illustrates the fracture behavior at the early stage of micro crack initiation. A pure Zener-Stroh crack can be initiated by a pile-up of real physical dislocations without external loading, which is the major difference comparing with the famous Griffith crack. In the current chapter, Irwin plastic zone correction has been introduced to study the fracture behavior of a Zener-Stroh crack near a coated inclusion. The influence of the coating phase properties and other material/geometric constants on the effective stress intensity factor, plastic zone size and crack tip opening displacement of the crack are emphasized. The generalized Irwin model is introduced to determine the plastic zone size at the sharp and blunt crack tip of the Zener-Stroh crack. For a Zener-Stroh crack, the crack propagation always occurs from the sharp tip, but yielding exists at the blunt tip as well.

5.2. The generalized Irwin model for a Zener-Stroh crack

5.2.1. Zener-Stroh crack mechanism

Zener-Stroh crack, different to the conventional Griffith crack, is another type of crack which was proposed initially by Zener [109]. In this model, a pileup of edge dislocations that were stopped at an obstacle, such as a grain boundary (Fig. 5.1(a)), could coalesce into a crack nucleus. An experimental SEM photo of a crack initiated by this physical mechanism is shown Fig. 5.2. Zener's research work was further developed by Stroh [110, 111], who analyzed the amount of dislocations needed for such nucleation in the absence/presence of a slip plane. Weertman [112] compared the stress, displacement, dislocation and stress intensity factor between the Griffith crack and Zener-Stroh crack. Fan and Xiao [113] examined the stress intensity factor of Zener-Stroh crack near an interface. The multiple Zener-Stroh crack problem was looked into by Chen [114]. Besides Zener's mechanism of micro crack initiation, there are some other variants. One was presented by Cottrell [115], where piled-up dislocations on two intersecting slip planes can coalesce into a micro crack as shown in Fig. 5.1(b). Fig. 5.1(c) shows a particle at a grain boundary in a stressed solid, concentrated stress fields exist near the ends of the particle, slip is thus nucleated in these regions. This is another variant proposed by Kikuchi [116]. In this model, dislocations of one sign move away from the region, leaving stationary dislocations of the opposite sign behind to form a crack near the particle.

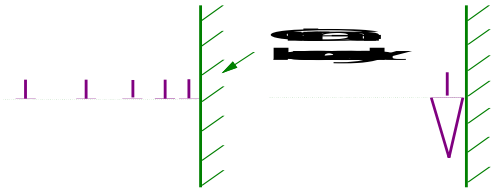

(a)

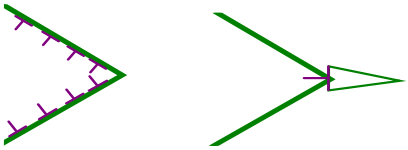

(b)

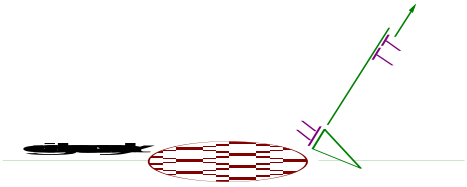

(c)

Fig. 5.1 (a) Zener's mechanism of crack initiation; (b) Cottrel's model of crack initiation; (c) Anti-Zener-Stroh crack model

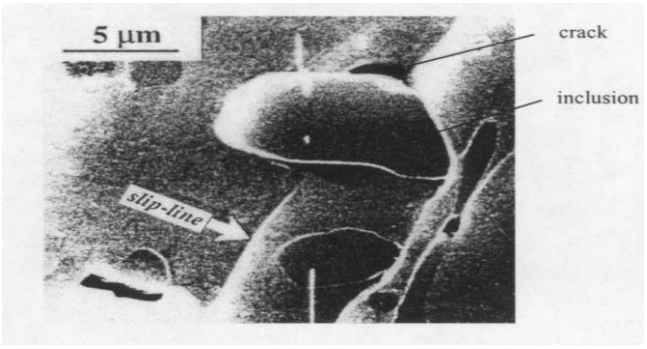

Fig. 5.2 A pile-up of dislocations stopped by an inclusion to form a Zener-Stroh crack.

Different to the famous Griffith crack, the physical parameters that are symmetric for the Griffith crack are anti-symmetric for the Zener-Stroh crack and vice versa. The Zener-Stroh crack has an anti-symmetric crack plane traction stress which arises from a symmetric crack plane dislocation distribution. For a Zener-Stroh crack, the total sum of the Burgers vectors of the dislocations is not equal to zero according to the displacement loading mechanism. The two crack

tips of Zener-Stroh crack are different. The tip where the dislocation enters the crack is a blunt tip and the other tip is a sharp tip, as shown in Fig. 5.3(a). The crack propagation always starts from the sharp tip.

5.2.2. Plastic zone sizes

It is noted that for a Zener-Stroh crack, the crack tip where the dislocations enter the crack is a blunt tip and the other tip is a sharp tip. The closure stress distribution of the Zener-Stroh crack is given in Fig. 5.3. It is found from Fig. 5.3(b) and 5.3(c) that the blunt tip of a Zener-Stroh crack is under tensile closure stress and the sharp tip is under compression stress, which means the crack is unable to be opened at the blunt tip, but plastic zone still exists ahead of the blunt crack tip.

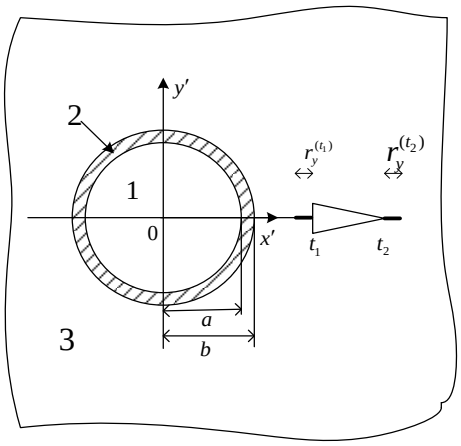

5.3(a)

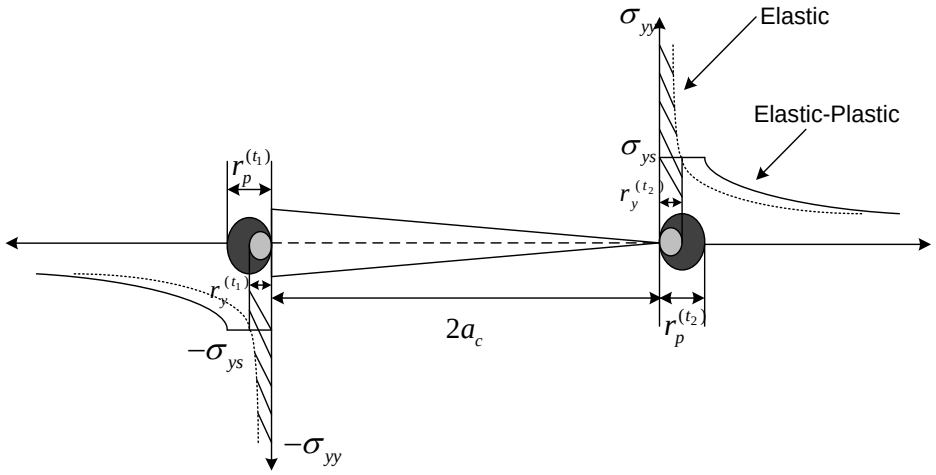

5.3(b)

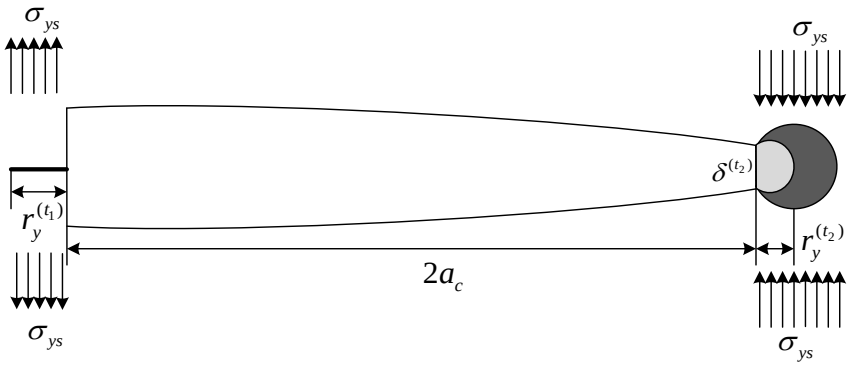

5.3(c)

Fig. 5.3 The current problem: (a) A Zener-Stroh crack near a coated circular inclusion with plastic zone correction; (b) Irwin Plastic Zone Model: plastic zones of sizes r_y and r_p ahead of a crack tip; (c) The crack tip opening displacement δ and corresponding loading conditions.

The first order estimation of plastic zone size at the crack tip (t_m) is given as:

$$r_y^{(t_m)} = \frac{1}{2\pi}\left(\frac{K_e^{(t_m)}}{\sigma_{ys}}\right)^2, \tag{5.1}$$

where $(t_m), m = 1, 2$ represent the left and right crack tip, respectively, and

$$K_e^{(t_m)} = \sqrt{\left(1-2\nu_3\right)^2\left(K_I^{(t_m)}\right)^2 + 3\left(K_{II}^{(t_m)}\right)^2}, \tag{5.2}$$

$K_e^{(t_m)}$ is a constant related to the stress intensity factors $K_I^{(t_m)}$ and $K_{II}^{(t_m)}$ which represents the strength of the equivalent stress fields near the crack tips along the

crack line.

When the stress in the cross-hatched region (shown in Fig. 5.3(b)) is considered, a second-order estimation of plastic zone size is obtained by the force balance equation:

$$\sigma_{ys} r_p^{(t_m)} = \int_0^{r_y} \sigma_e^{(t_m)} dr^{(t_m)} = \int_0^{r_y} \frac{K_e^{(t_m)}}{\sqrt{2\pi r^{(t_m)}}} dr^{(t_m)}, \tag{5.3}$$

which leads to:

$$r_p^{(t_m)} = 2r_y^{(t_m)} = \frac{1}{\pi}\left(\frac{K_e^{(t_m)}}{\sigma_{ys}}\right)^2. \tag{5.4}$$

5.2.3. The crack tip opening displacement (CTOD)

As depicted in Fig. 5.3(c), for a Zener-Stroh crack, the plastic zone of left crack tip (the blunt tip) is caused by compression, while the plastic zone at right crack tip (the sharp tip) is caused by tension. The crack propagation always occurs from the sharp tip, which is different to the Griffith crack. Hence, only the crack tip opening displacement at the sharp tip is considered. Based on the generalized Irwin model, the expression of CTOD can be given as:

$$\delta^{(t_2)} = \frac{8}{E'} K_I^{(t_2)} \sqrt{\frac{r_y^{(t_2)}}{2\pi}}, \tag{5.5}$$

where $E' = E_3 \big/ \left(1 - \nu_3^2\right)$ in plane strain. Substituting Eq. (5.4) into (5.5) leads:

$$\delta^{(t_2)} = \frac{4}{\pi} \frac{K_I^{(t_2)} K_e^{(t_2)}}{E' \sigma_{ys}}. \tag{5.6}$$

5.3. Formulation of the current problem

As depicted in Fig. 5.3(a), the physical problem to be studied is a Zener-Stroh crack interacting with a coated circular inclusion. Both the crack and the coated inclusion are embedded in the matrix. The left crack tip is at a distance t_1 from the inclusion center, with the plastic zone size $r_y^{(t_1)}$. The right crack tip is at a distance t_2 and the plastic zone size is $r_y^{(t_2)}$. The crack is orientated along the radial direction of the circular inclusion which occupies the area of $r < a$ with material properties μ_1 (shear modulus) and ν_1 (Poisson's ratio). The region $a < r < b$ is the coating phase with material properties μ_2 and ν_2. The matrix occupies the region of $r > b$ with the material properties μ_3 and ν_3.

In order to concentrate on the effect of the net dislocations inside the Zener-Stroh crack, the problem is studied without external loading:

$$\sigma_{yy}^{\infty} = \sigma_{xy}^{\infty} = 0. \tag{5.7}$$

The distributed dislocation technique [14] is adopted to simulate the crack near the inclusion. As the crack tip opening displacement (CTOD) mainly depends on the mode I loading, only the climb dislocation density $B_y(x)$ is considered in the following derivation. Setting $B_y(x)$ as the climb dislocation density in the crack zone, making use of the distributed dislocation method [14], the traction at $(x,0)$ due to the dislocation distribution is:

$$\sigma_{yy}(x,0) = -\frac{2\mu_3}{(\kappa_3+1)\pi}\left[\int_{t_1}^{t_2}\frac{B_y(\xi)}{\xi - x}d\xi + \int_{t_1}^{t_2} k_1(x,\xi)B_y(\xi)d\xi\right], \quad t_1 \le x \le t_2 \tag{5.8}$$

here, $\kappa_3 = 3-4\nu_3$ is a constant of material properties of the matrix. Then the traction free conditions on the upper and lower crack surface are written in terms of B_y:

$$\frac{1}{\pi}\left[\int_{t_1}^{t_2}\frac{B_y(\xi)}{\xi-x}d\xi+\int_{t_1}^{t_2}k_1(x,\xi)B_y(\xi)d\xi\right]=0,\quad t_1\le x\le t_2 \tag{5.9}$$

The kernel $k_1(x,\xi)$ is given as [117]:

$$\begin{aligned}k_1(x,\xi)=&\frac{C+D}{2\left(x-b^2/\xi\right)}+C\frac{\xi^2-b^2}{\xi^3}\frac{b^2}{\left(x-b^2/\xi\right)^2}?\left[\left(\frac{\xi}{b}\right)^2-\frac{\xi^2-b^2}{x\xi-b^2}\right]\\&-\frac{C+D}{2x}-\frac{1-CD}{2(1-C)}a_0\frac{b}{x^2}-\frac{1}{2\xi}\left(\frac{b}{x}\right)^2\left[2C\left(\frac{\xi}{\beta}\right)^2-C-1\right]\\&+\frac{1-CD}{2b(1-D)}\left[\sum_{n=1}^{\infty}na_{-n}\left(\frac{b}{x}\right)^n-\sum_{n=1}^{\infty}(n+1)a_{-n}\left(\frac{b}{x}\right)^{n+2}\right]-C\frac{b^2}{x^3}\\&-\frac{1-CD}{b(1-D)}\sum_{n=1}^{\infty}a_{-n}\left(\frac{b}{x}\right)^n-\frac{1-CD}{2b(1-C)}\sum_{n=1}^{\infty}a_n\left(\frac{b}{x}\right)^{n+2},\end{aligned} \tag{5.10}$$

where the detailed expression of the coefficients a_n and a_n' can be found in the work of Xiao and Chen [117], and

$$C=\frac{\mu_3-\mu_2}{\mu_2\kappa_3+\mu_3},\ D=\frac{\mu_3\kappa_2-\mu_2\kappa_3}{\mu_3\kappa_2+\mu_2}. \tag{5.11}$$

Similarly, $\kappa_i = 3-4\nu_i, i=1,2,3,$ is material constant of phase "i". $\nu_i, i=1,2,3,$ is the Poisson's ratio of phase "i".

Moreover, for the Zener-Stroh crack, the dislocation density $B_y(x)$ must satisfy:

$$\int_{t_1}^{t_2}B_y(\xi)d\xi=b_y^T, \tag{5.12}$$

where b_y^T is the total sum of Burgers vectors of the net dislocation inside the Zener-Stroh crack.

5.3.1. The stress intensity factors

Equation (5.9) is the standard singular integral equation with Cauchy type regular kernels. Once the dislocation density B_y is solved, the stress fields in the matrix phase can be obtained from Eq. (5.8). The singularity on the both crack tips should be inverse square root since the whole crack is located in the pure matrix material. As a result, the dislocation density function can be taken as:

$$B_y(x) = \omega(x) F_y(x), \tag{5.13}$$

where $F_y(x)$ is non-singular smooth function in $t_1 \le x \le t_2$, and

$$\omega(x) = (x - t_1)^{-1/2} (t_2 - x)^{-1/2}, \tag{5.14}$$

is the fundamental function of the integral equation.

The numerical procedure for solving the equations was given by Erdogan and Gupta [80]. The integral interval is shifted from (t_1, t_2) to $(-1,1)$ by:

$$x = \frac{t_2 - t_1}{2} t + \frac{t_2 + t_1}{2}, \xi = \frac{t_2 - t_1}{2} s + \frac{t_2 + t_1}{2}. \tag{5.15}$$

Then, Eqs. (5.9) and (5.12) are rewritten in terms of s,t as:

$$\frac{1}{\pi} \int_{-1}^{1} \frac{B_y(s)}{s - t} ds + \frac{1}{\pi} \int_{-1}^{1} k_{11}(t, s) B_y(s) ds = 0, \quad -1 < s, t < 1, \tag{5.16}$$

$$\int_{-1}^{1} B_y(s) ds = \frac{2 b_y^T}{t_2 - t_1}. \tag{5.17}$$

Here,

$$k_{11}(t, s) = \frac{t_2 - t_1}{2} k_1 \left(\frac{t_2 - t_1}{2} t + \frac{t_2 + t_1}{2}, \frac{t_2 - t_1}{2} s + \frac{t_2 + t_1}{2} \right). \tag{5.18}$$

The expression of $k_1(x, \xi)$ was given in Eq. (5.10). $B_y(s)$ is the dislocation density in $y-$direction and b_y^T is the total sum of Burgers vectors of the net dislocation inside the Zener-Stroh crack.

With the numerical solution of the dislocation density function found from Eqs. (5.16) and (5.17), the mode I stress intensity factor on the left (the blunt) and right (the sharp) crack tips are given by [15]:

$$\begin{aligned} K_I^{(t_1)} &= \lim_{\xi \to t_1} \frac{-2\mu_3\sqrt{2\pi}}{\kappa_3+1}\sqrt{\xi - t_1}B_y(x) = -\frac{2\mu_3}{\kappa_3+1}\frac{b_y^T}{\sqrt{\pi(t_2-t_1)/2}}F_y(-1), \\ K_I^{(t_2)} &= \lim_{\xi \to t_2} \frac{2\mu_3\sqrt{2\pi}}{\kappa_3+1}\sqrt{t_2 - \xi}B_y(x) = \frac{2\mu_3}{\kappa_3+1}\frac{b_y^T}{\sqrt{\pi(t_2-t_1)/2}}F_y(1). \end{aligned} \tag{5.19}$$

Here, (t_1) and (t_2) represent the left and right crack tips, respectively.

5.3.2. The effective stress intensity factors

For small scale yielding, the effective half crack length can be approximated as:

$$a_{eff}^{(t_m)} = a_c + r_y^{(t_m)}, \tag{5.20}$$

where, $a_{eff}^{(t_m)}$ is the effective half crack length from the (t_m) tip. a_c is the initial half crack length as shown in Fig. 5.3. $r_y^{(t_m)}$ is the first order estimation of plastic zone size obtained from Eq. (5.1). Eqs. (5.9) and (5.12) can be rewritten as:

$$\frac{1}{\pi}\left[\int_{t_1'}^{t_2'}\frac{B_y(\xi)}{\xi - x}d\xi + \int_{t_1'}^{t_2'}k_1(x,\xi)B_y(\xi)d\xi\right] = 0, \quad t_1' \le x \le t_2' \tag{5.21}$$

$$\int_{t_1'}^{t_2'} B_y(\xi)d\xi = b_y^T, \tag{5.22}$$

where, $t_1' = t_1$ for the left crack tip and $t_2' = t_2 + r_y^{(t_2)}$ for the right crack tip, respectively. Here, plastic zone correction is only considered at the right crack tip, because the crack tip opening exists at the sharp tip only. By solving Eqs. (5.21) and (5.22), the effective stress intensity factors are obtained in the expression:

$$K_I^{eff,(t_2)} = \lim_{\xi \to t_2} \frac{2\mu_3\sqrt{2\pi}}{\kappa_3 + 1}\sqrt{t_2' - \xi}B_y(x) = \frac{2\mu_3}{\kappa_3 + 1}\frac{b_y^T}{\sqrt{\pi(t_2' - t_1')/2}}F_y'(1). \quad (5.23)$$

Here, $F_y'(1)$ is solved from the singular integral equations (5.21) and (5.22).

5.4. Numerical examples and discussions

In this section, numerical examples are given to show the results of stress intensity factors (SIFs), plastic zone sizes and CTOD (at the sharp tip) for a Zener-Stroh crack near a coated circular inclusion. Only the displacement loading b_y^T is considered.

The stress intensity factors, the plastic zone sizes and the CTOD are normalized separately by:

$$K_0 = \frac{2\mu_3 b_y^T}{(1+\kappa_3)\sqrt{\pi(t_2 - t_1)/2}},\ r_{y0} = \frac{\left(K_0^e\right)^2}{2\pi\sigma_{ys}^2},\ \delta_{y0} = \frac{4K_0K_0^e}{\pi E'\sigma_{ys}}. \quad (5.24)$$

Here, K_0, r_{y0} and δ_{y0} are the mode I stress intensity factor, the plastic zone size and the CTOD separately for the same Zener-Stroh crack in a homogeneous material without the inclusion. Here, $K_0^e = (1-2\nu_3)K_0$ in plane strain when the mode II stress intensity factor is zero.

5.4.1. Effects of the shear modulus of the inclusion

Since the mode II stress intensity factor is not involved in the current study, Eqs. (5.1) and (5.6) are re-written as:

$$r_y^{(t_m)} = \frac{1}{2\pi}\frac{(1-2\nu_3)^2\left(K_I^{(t_m)}\right)^2}{\sigma_{ys}^2}. \quad (5.25)$$

$$\delta^{(t_m)} = \frac{4}{\pi}\frac{(1-2\nu_3)K_I^{(t_m)2}}{E'\ \sigma_{ys}}. \quad (5.26)$$

Considering Eq.(5.24), the normalized plastic zone size $r_y^{(t_m)}/r_{y0}$ and the normalized CTOD $\delta^{(t_m)}/\delta_{y0}$ are written as:

$$\frac{r_y^{(t_m)}}{r_{y0}} = \frac{\delta^{(t_m)}}{\delta_{y0}} = \left(\frac{K_I^{(t_m)}}{K_0} \right)^2 .$$

The normalized plastic zone size $r_y^{(t_m)}/r_{y0}$ is emphasized in the following sections.

The curves of the normalized SIF and the normalized plastic zone size with the shear modulus ratio μ_1/μ_3 are depicted in Figs. 5.4(a) to 5.4(d). A series of coating layer thickness are taken as: $b/a = 1.05, 1.2, 1.5$. Other parameters are: $t_1 = 1.05b$, $t_2 = 1.35b$, $\mu_2/\mu_3 = 2.33$, $\nu_1 = 0.3$, $\nu_2 = 0.28$ and $\nu_3 = 0.3$. From Fig. 5.4(b), it is observed that the values of the normalized SIF at the right crack tip are always greater than 1, which indicates that a harder inclusion makes a Zener-Stroh easier to propagate. Similar phenomena are also observed in the curves of the normalized plastic zone size, which signifies that a harder inclusion causes a larger plastic zone size and CTOD, as shown in Fig. 5.4(d). For the left (blunt) crack tip, the normalized SIF is always below zero (Fig. 5.4(a)) and the normalized plastic zone size below 1 (Fig. 5.4(c)), which agrees with the physical phenomena that propagation of a Zener-Stroh crack always occur at the sharp tip.

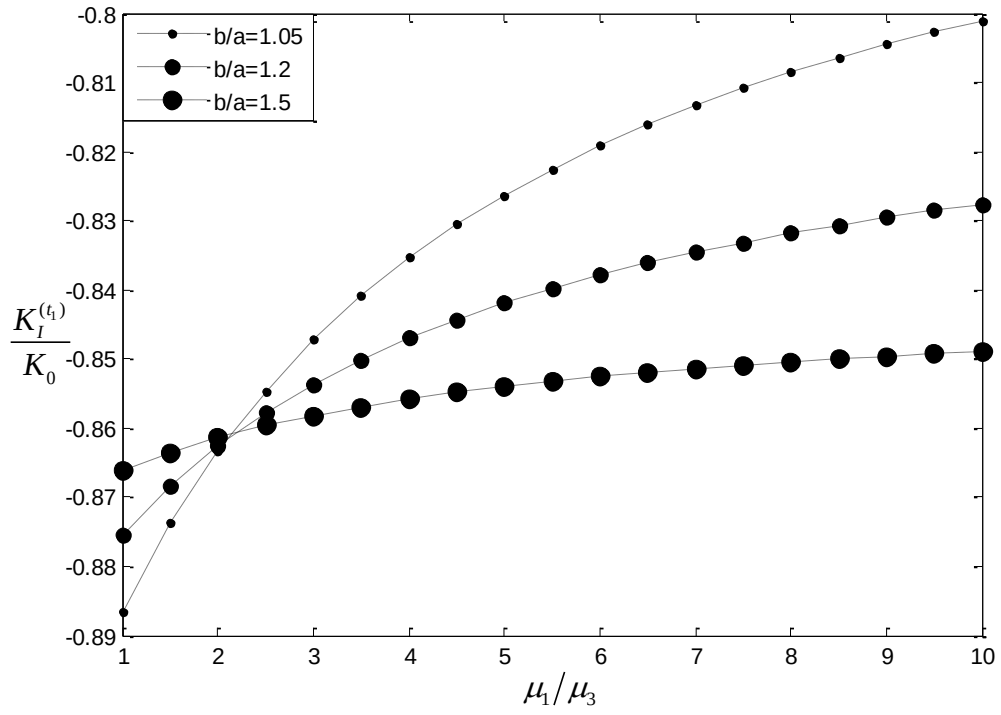
b/a=1.05
b/a=1.2
b/a=1.5
-0.8
-0.81
-0.82
-0.83
-0.84
-0.85
-0.86
-0.87
-0.88
-0.89
$\frac{K_I^{(t_1)}}{K_0}$
1
2
3
4
5
6
7
8
9
10
μ_1/μ_3

5.4(a)

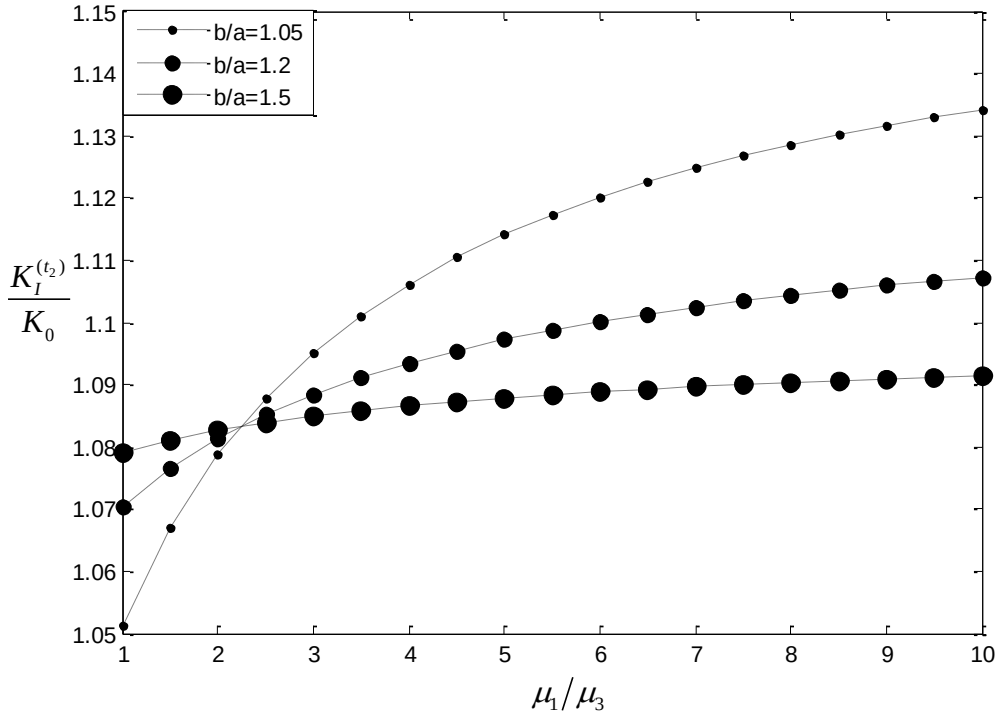
b/a=1.05
b/a=1.2
b/a=1.5
1.15
1.14
1.13
1.12
1.11
1.1
1.09
1.08
1.07
1.06
1.05
$\frac{K_I^{(t_2)}}{K_0}$
1
2
3
4
5
6
7
8
9
10
μ_1/μ_3

5.4(b)

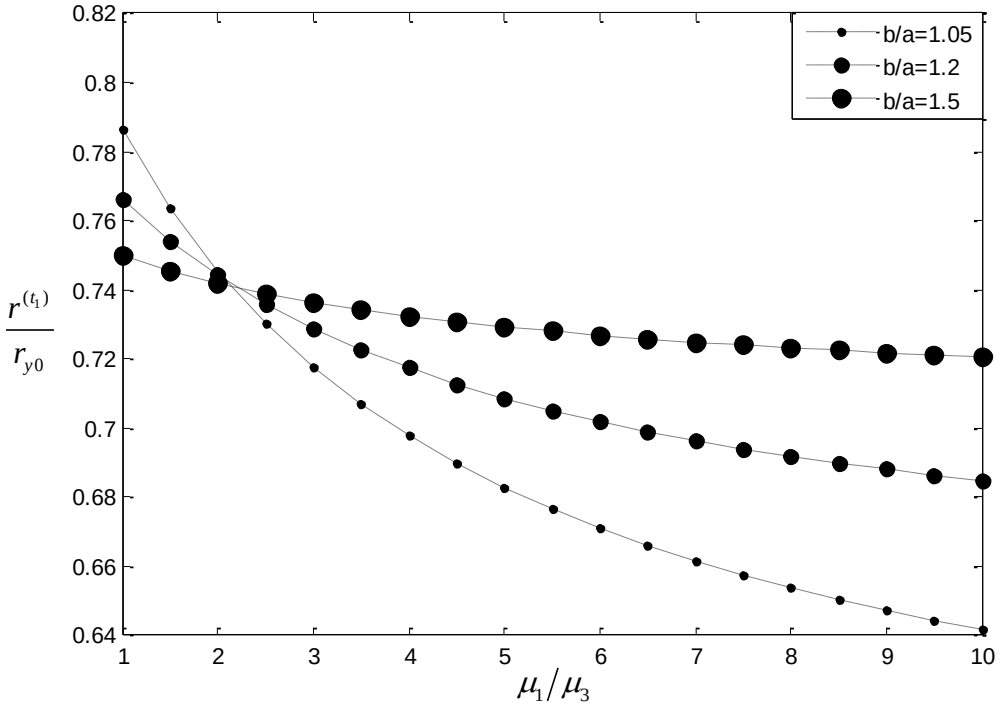

5.4(c)

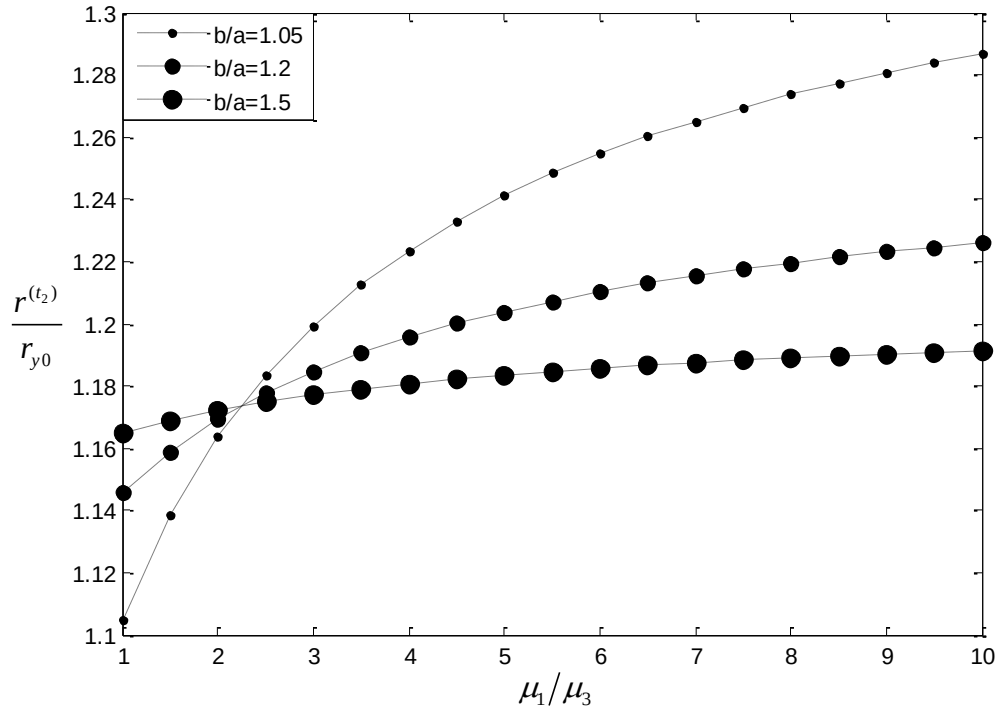

5.4(d)

Fig. 5.4 Effect of shear modulus ratio μ_1/μ_3 (inclusion/matrix), with $t_1 = 1.05b$, $t_2 = 1.35b$, $\mu_2/\mu_3 = 2.33$, $\nu_1 = 0.3, \nu_2 = 0.2$, and $\nu_3 = 0.3$: (a) The normalized SIF of left crack tip; (b) The normalized SIF of right crack tip; (c) The normalized plastic zone size of the left crack tip; (d) The normalized plastic zone size of the right crack tip.

5.4.2. Effects of the shear modulus of coating phase

In this section, the influence of the shear modulus of the coating phase on the crack behavior is investigated. The other parameters are taken as: $\nu_1=\nu_2=\nu_3=0.3$, $b/a=1.1$, $t_1=1.05b$ and $t_2=1.35b$, the shear modulus ratio: $\mu_1/\mu_3=0.1,0.5,1,2,5,10,$ including the conditions that the inclusion is “softer” and “harder” than the matrix. The coating phase is assumed to be "harder" than the matrix $(\mu_2/\mu_3>1)$.

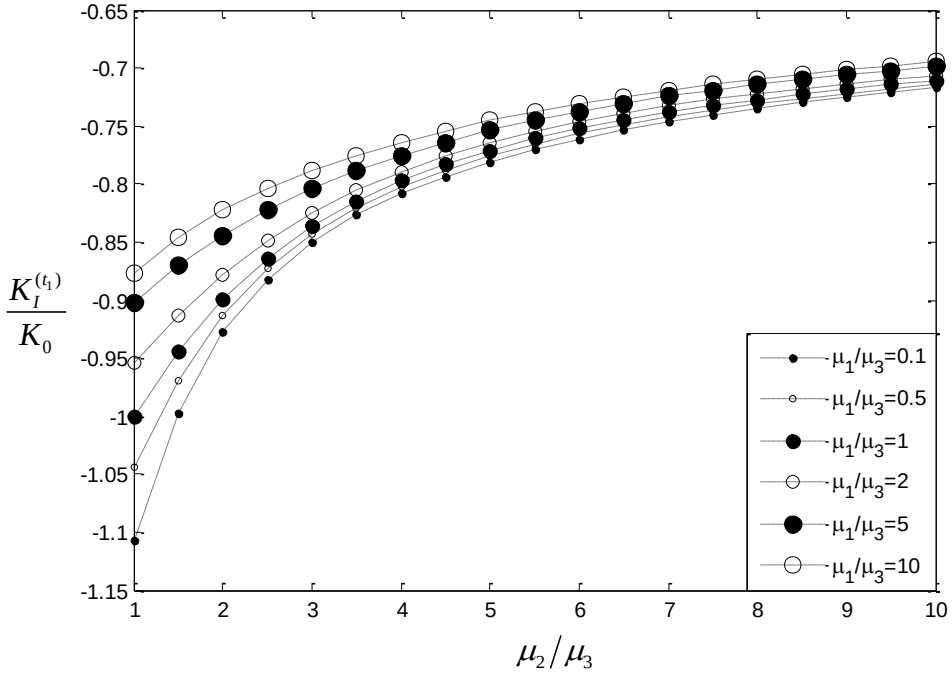

5.5(a)

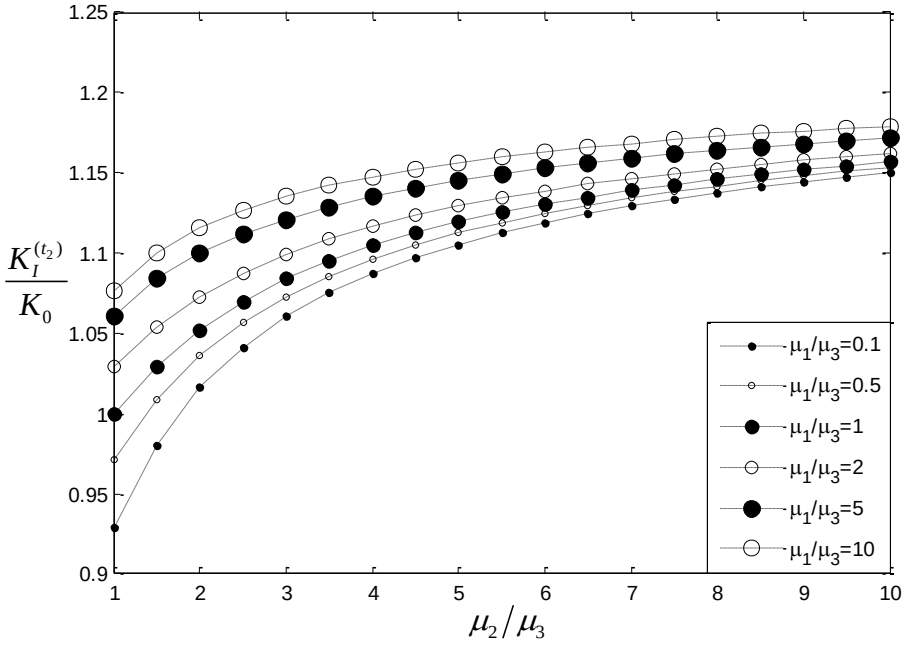
$\frac{K_I^{(t_2)}}{K_0}$
μ_2/μ_3
μ1/μ3=0.1
μ1/μ3=0.5
μ1/μ3=1
μ1/μ3=2
μ1/μ3=5
μ1/μ3=10

5.5(b)

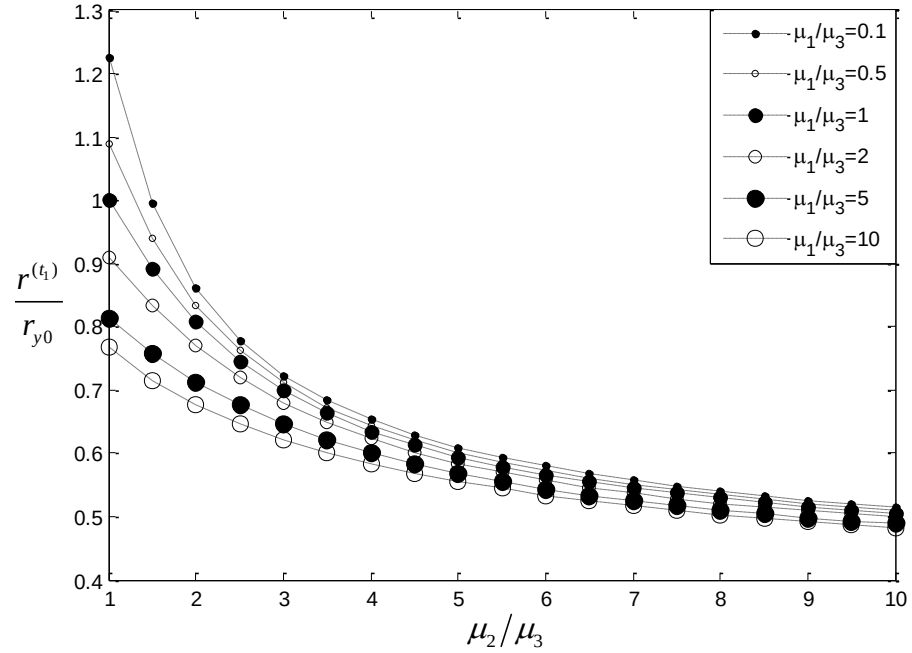
$\frac{r^{(t_1)}}{r_{y0}}$
μ_2/μ_3
μ1/μ3=0.1
μ1/μ3=0.5
μ1/μ3=1
μ1/μ3=2
μ1/μ3=5
μ1/μ3=10

5.5(c)

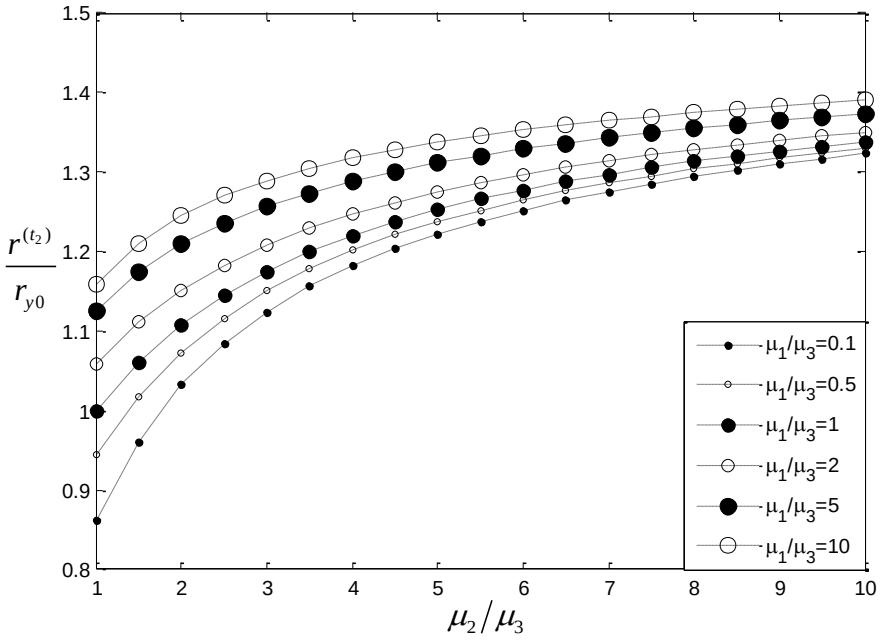

5.5(d)

Fig. 5.5 Effect of shear modulus ratio μ_2/μ_3 (coating phase/matrix), with $\nu_1=\nu_2=\nu_3=0.3$, $b/a=1.1$, $t_1=1.05b$ and $t_2=1.35b$: (a) The normalized SIF of left crack tip; (b) The normalized SIF of right crack tip; (c) The normalized plastic zone size of the left crack tip; (d) The normalized plastic zone size of the right crack tip.

The normalized SIF and the normalized plastic zone size at the left and right crack tips are depicted in Figs. 5.5(a) to 5.5(d). With the increasing coating phase shear modulus (μ_2/μ_3), the normalized SIFs at both crack tips increase. The normalized plastic zone sizes at the right crack tip increases as well, while the normalized plastic zone size at the left tip decreases. Also we observed that the normalized SIFs and the normalized plastic zone sizes are insensitive to the change of the inclusion phase shear modulus (μ_1/μ_3) when μ_2/μ_3 is increasing. It is concluded that a "harder" coating phase can reduce/shield the influence of the inclusion on the stress and displacement fields near the crack tips.

5.4.3. Effects of the coating phase thickness

In this section, the influence of the coating phase thickness on the elastic-plastic fracture behavior of the Zener-Stroh crack is discussed. The other parameters are set as: $\nu_1=\nu_2=\nu_3=0.3$, $t_1=1.05b$, $t_2=1.35b$, $\mu_1/\mu_3=0.1,0.5,1,1.86,5,10$, $\mu_2/\mu_3=1.86$. When the coating phase and the inclusion have the same type of materials and the current problem is simplified to the two-phase problem. The variable b/a changes from 1 to 2.

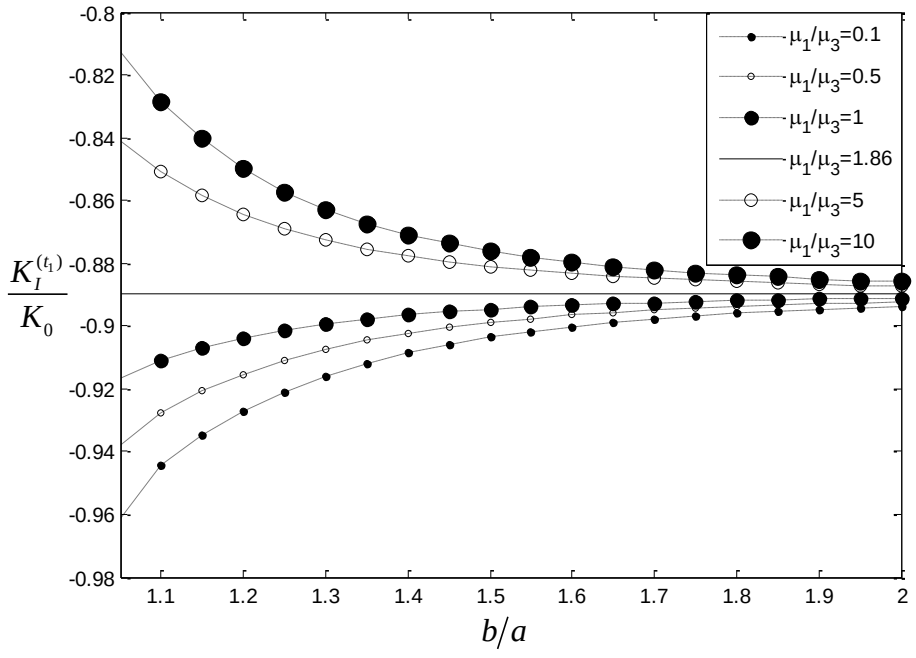

5.6(a)

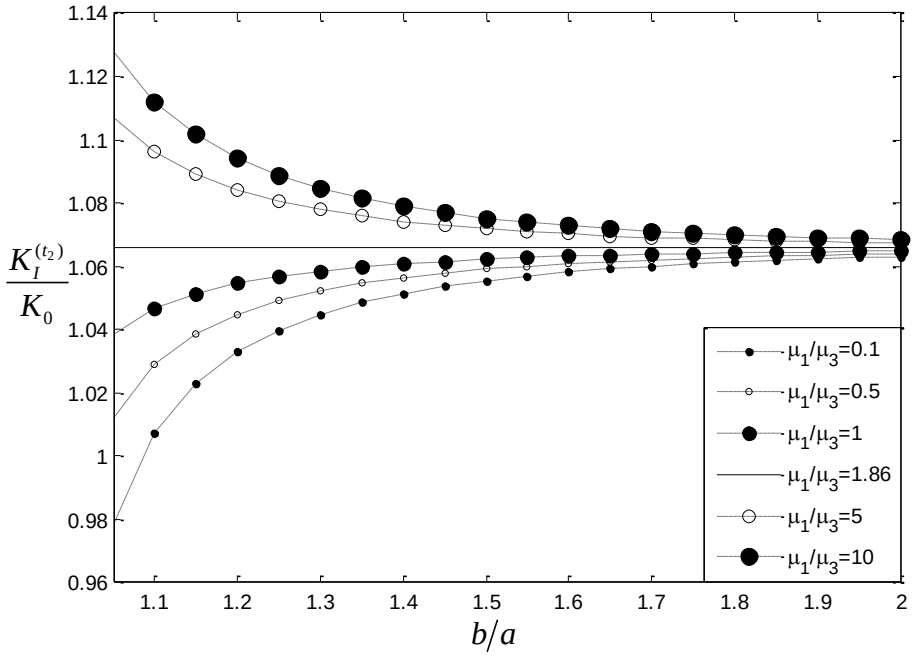
1.14
1.12
1.1
1.08
1.06
1.04
1.02
1
0.98
0.96
$\frac{K_I^{(t_2)}}{K_0}$
1.1
1.2
1.3
1.4
1.5
1.6
1.7
1.8
1.9
2
b/a
μ_1/μ_3=0.1
μ_1/μ_3=0.5
μ_1/μ_3=1
μ_1/μ_3=1.86
μ_1/μ_3=5
μ_1/μ_3=10

5.6(b)

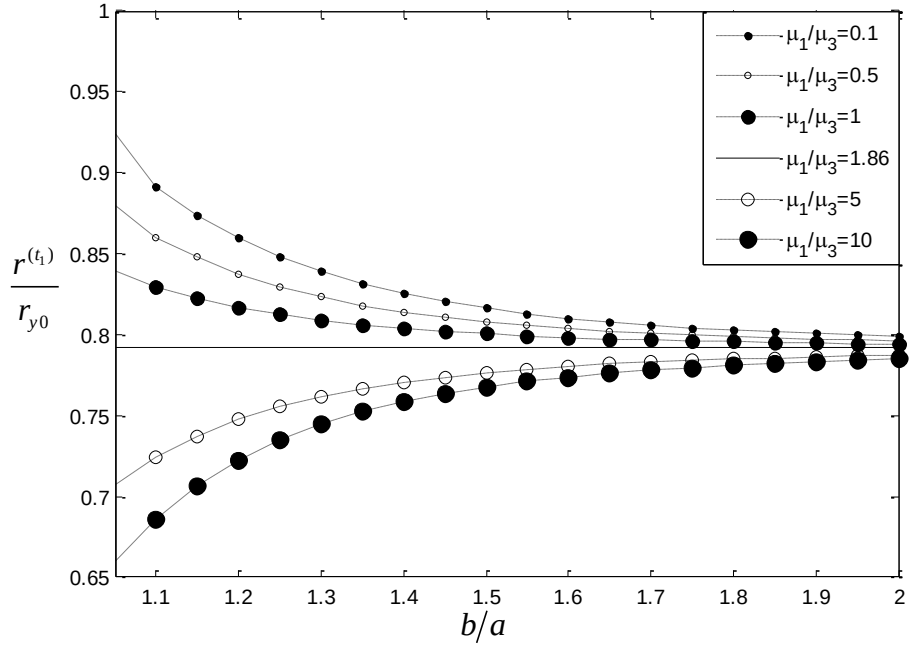
1
0.95
0.9
0.85
0.8
0.75
0.7
0.65
$\frac{r^{(t_1)}}{r_{y0}}$
1.1
1.2
1.3
1.4
1.5
1.6
1.7
1.8
1.9
2
b/a
μ_1/μ_3=0.1
μ_1/μ_3=0.5
μ_1/μ_3=1
μ_1/μ_3=1.86
μ_1/μ_3=5
μ_1/μ_3=10

5.6(c)

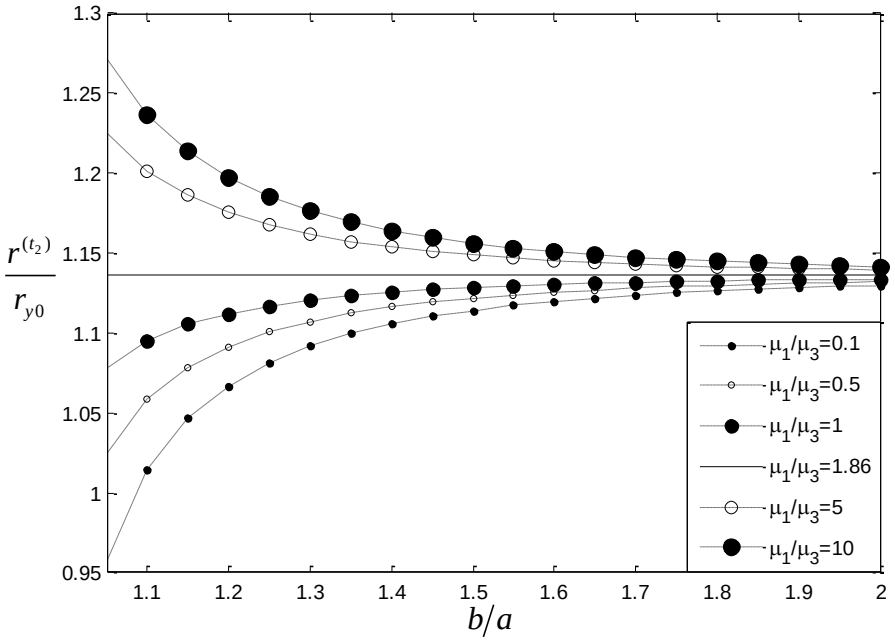

5.6(d)

Fig. 5.6 Effect of coating phase thickness b/a with $\nu_1 = \nu_2 = \nu_3 = 0.3$, $t_1 = 1.05b$, $t_2 = 1.35b$ and $\mu_2/\mu_3 = 1.86$: (a) The normalized SIF of left crack tip; (b) The normalized SIF of right crack tip; (c) The normalized plastic zone size of the left crack tip; (d) The normalized plastic zone size of the right crack tip.

The curves of the normalized SIF and the normalized plastic zone size at the both crack tips are illustrated in Figs. 5.6(a) to 5.6(d). In these figures, it is shown that when the coating thickness increases, the influence of the shear modulus ratio μ_1/μ_3 decreases. In other words, a thick coating will reduce the influence of the inclusion material on the crack. The figures also illustrate that, when $\mu_1 > \mu_2$, the normalized SIF at both crack tips and the normalized plastic zone size at the right tip decrease with increasing b/a. When $\mu_1 < \mu_2$, these normalized quantities all increase with the increasing b/a. On the other hand, for the normalized plastic zone size at the left crack tip (blunt tip), it increases with increasing b/a when $\mu_1 > \mu_2$, and decreases with increasing b/a when $\mu_1 < \mu_2$. From the above

observations, it can be concluded that when the inclusion is harder than the coating phase ($\mu_1 > \mu_2$), a thicker coating phase helps avoid fracture failures. Conversely, when the inclusion is "softer" than the coating phase ($\mu_1 < \mu_2$), a thinner coating phase is better to prevent fracture failures.

5.4.4. Effects of the distance between the crack and the inclusion

In this section, the influence of the distance between the crack and the inclusion is studied. The normalized SIF and the normalized plastic zone size at both crack tips are plotted in Figs. 5.7(a) to 5.7(d). The length of the Zener-Stroh crack is fixed at $t_2 - t_1 = 0.5b$. Other parameters are set as: $\mu_1/\mu_3 = 5.43$, $\nu_1 = \nu_2 = \nu_3 = 0.25$ and $b/a = 1.1$. The coating phase shear modulus is set to: $\mu_2/\mu_3 = 1, 2, 5, 10$.

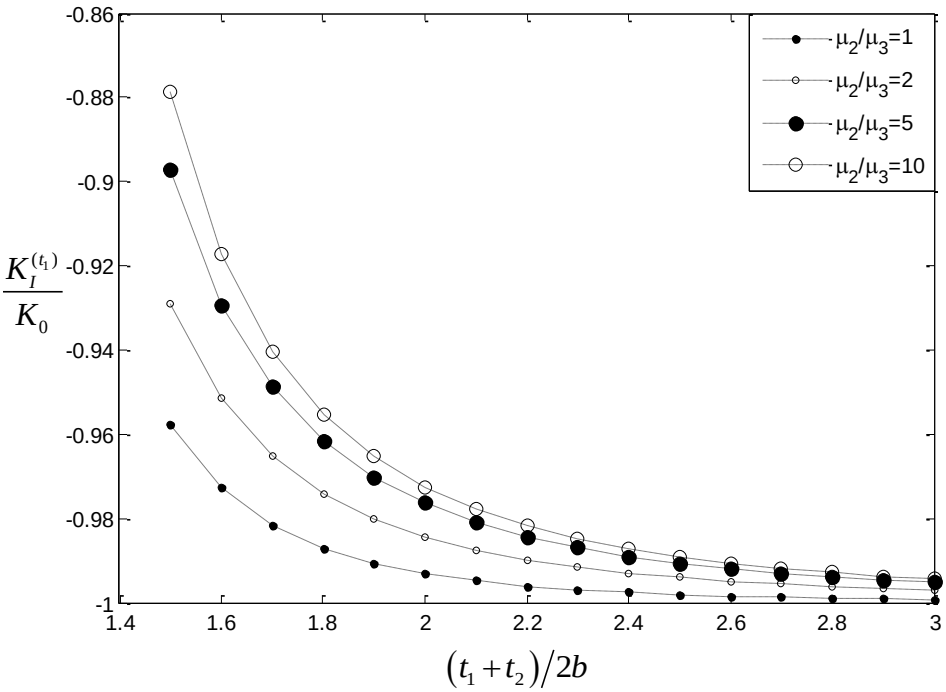

5.7(a)

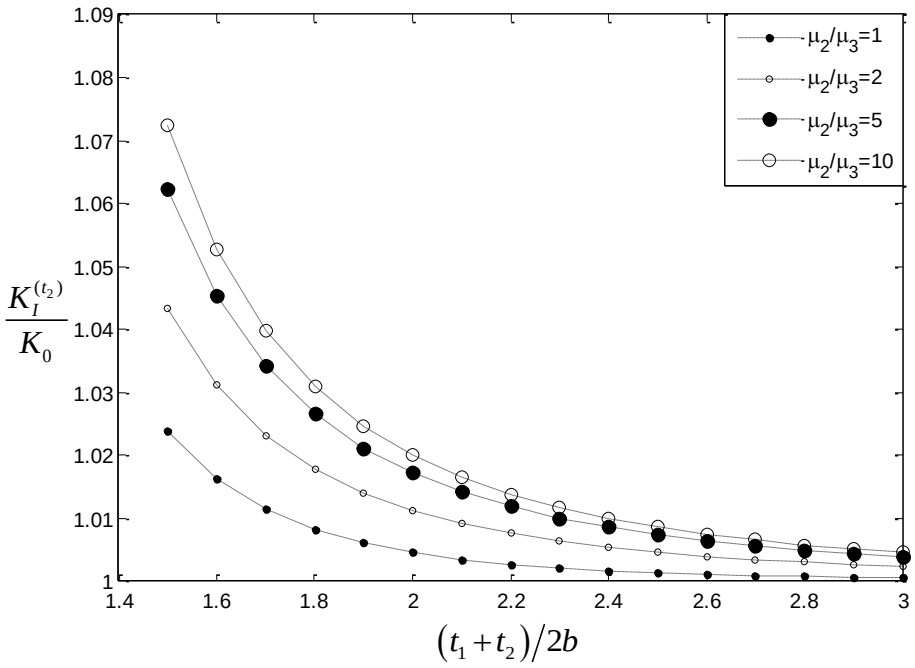
1.09
1.08
1.07
1.06
1.05
1.04
1.03
1.02
1.01
1
1.4
1.6
1.8
2
2.2
2.4
2.6
2.8
3
$\frac{K_I^{(t_2)}}{K_0}$
$(t_1+t_2)/2b$
μ2/μ3=1
μ2/μ3=2
μ2/μ3=5
μ2/μ3=10

5.7(b)

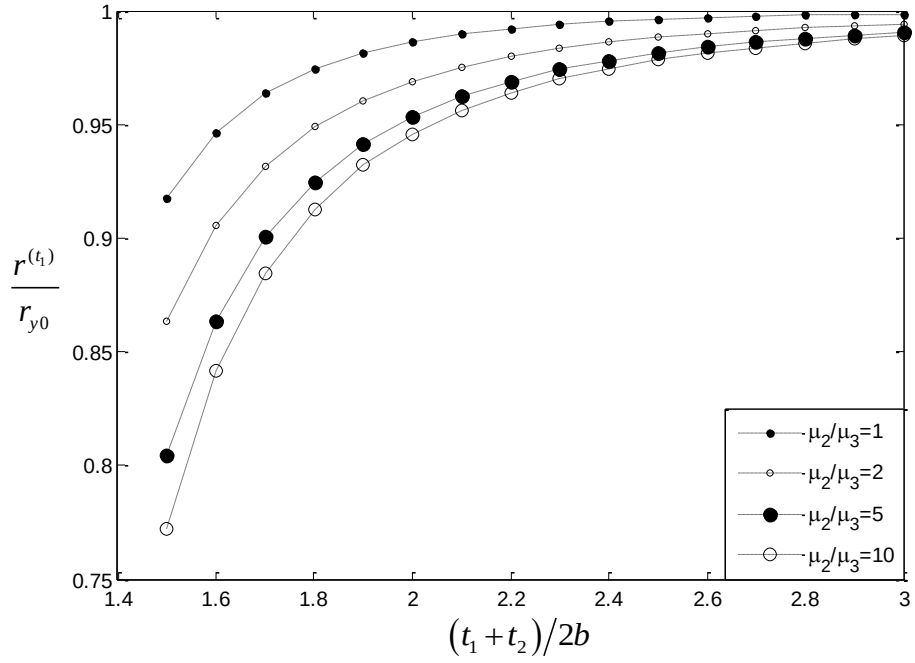
1
0.95
0.9
0.85
0.8
0.75
1.4
1.6
1.8
2
2.2
2.4
2.6
2.8
3
$\frac{r^{(t_1)}}{r_{y0}}$
$(t_1+t_2)/2b$
μ2/μ3=1
μ2/μ3=2
μ2/μ3=5
μ2/μ3=10

5.7(c)

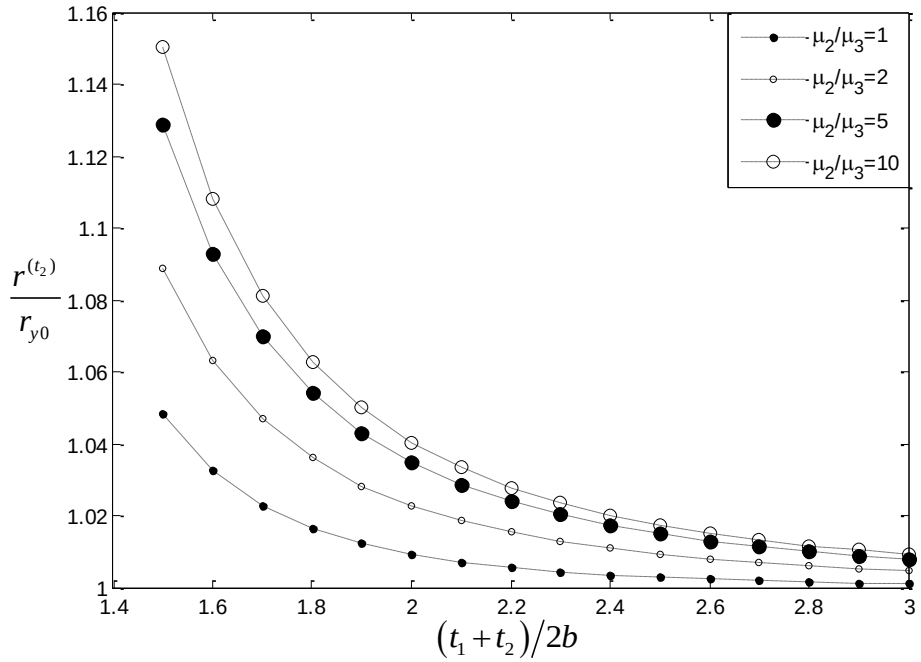

5.7(d)

Fig. 5.7 Effect of crack-inclusion distance $(t_1+t_2)/2b$ with $t_2-t_1=0.5b$, $\mu_1/\mu_3=5.43$, $\nu_1=\nu_2=\nu_3=0.25$, and $b/a=1.1$: (a) The normalized SIF of left crack tip; (b) The normalized SIF of right crack tip; (c) The normalized plastic zone size of the left crack tip; (d) The normalized plastic zone size of the right crack tip.

From Figs. 5.7(a) to 5.7(d), we observe that with the increasing crack-inclusion distance, the normalized SIF at both crack tips, and the normalized plastic zone size at the right crack tip decrease, while the normalized plastic zone size at the left crack tip increases. When the shear modulus of the coating phase is larger, its influence on the normalized SIF and the normalized plastic zone size will be greater.

5.4.5. Effective stress intensity factors

The curves of the effective stress intensity factor at the right crack tip (sharp tip) are shown in Fig. 5.8. The other involved parameters are taken as: $t_1=1.05b$,

$t_2 = 1.35b$, $\mu_2/\mu_3 = 2.33$, $\nu_1 = 0.3$, $\nu_2 = 0.28$ and $\nu_3 = 0.3$. Three different coating thicknesses, $b/a = 1.02, 1.2, 1.5$ are studied. The shear modulus of the inclusion is varied.

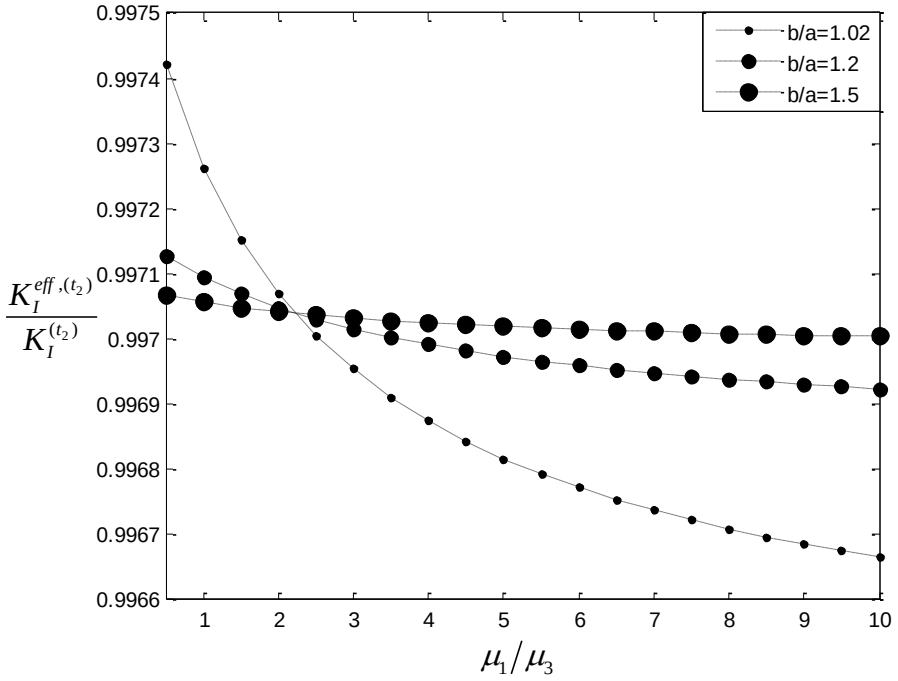

Fig. 5.8 The normalized effective SIF of the right crack tip versus μ_1/μ_3 with $t_1 = 1.05b$, $t_2 = 1.35b$, $\mu_2/\mu_3 = 2.33$, $\nu_1 = 0.3$, $\nu_2 = 0.28$ and $\nu_3 = 0.3$.

The effective stress intensity factor is normalized by the SIF value ($K_I^{(t_2)}$) of the same crack without plastic zone correction. When the plastic zone correction is considered, Fig. 5.8 illustrates the normalized effective SIF is slightly smaller than 1. This result means when the displacement loading b_y^T is fixed, a longer crack length will induce to smaller stress intensity factors, which is the major difference between a Zener-Stroh and a Griffith crack.

5.4.6. Comparison with the Dugdale model

In this section, the current results are compared with those obtained by Hoh et al. [118] where the plastic zone size and CTOD were solved by Dugdale mode.

$\nu_1=\nu_2=\nu_3$	$\delta^{(t_2)}/\delta_{y0}$		$\delta^{(t_1)}/\delta_{y0}$	
	Hoh[118]	Current	Hoh[118]	Current
0.2	1.2136	1.0293	1.0043	--
1/3	1.1837	1.0261	1.0037	--
0.45	1.1599	1.0242	1.0033	--

Table 5.1 Comparison of the normalized CTOD from Hoh et al. [118] and the current work, with $\mu_1=10\mu_3,\ \mu_2=\mu_3,\ \ t_1=1.6a,\ t_2=2.2a,\ \nu_1=\nu_2=\nu_3=0.2,1/3,$ and 0.45.

By taking the same materials constants, a comparison has been made between the result of Hoh and our current work as shown in Table 6.1, where $\mu_1=10\mu_3,\ \mu_2=\mu_3,\ \ t_1=1.6a,\ t_2=2.2a,\ \nu_1=\nu_2=\nu_3=0.2,1/3$ and 0.45. We can see when the current problem is reduced to the two-phase problem, the result obtained by our method agrees with Hoh's work well for the sharp crack tip. For the blunt crack tip, the CTOD was not considered in this model since the crack tip is under compression and not able to be opened.

5.5. Conclusions

In this chapter, the elastic-plastic stress investigation for a Zener-Stroh crack interacting with a near-by coated inclusion has been carried out based on the generalized Irwin model. We focus on the influence of the coating phase

properties on the stress intensity factor (SIF), effective stress intensity factor, plastic zone size and CTOD. The following conclusions are drawn from our study:

1. When the shear modulus ratio $\mu_1/\mu_3 > 1$, or the inclusion is "harder" than the matrix, a displacement loaded Zener-Stroh is easier to propagate than the same crack in a homogeneous material. Increasing the shear modulus of the coating phase (μ_2/μ_3), the influence of the inclusion on the normalized SIF and normalized plastic zone size decreases. With increasing the coating phase thickness, the influence of the inclusion on the quantities decreases as well.

2. When the inclusion is "harder" than the coating layer, the normalized SIF at the both crack tips, and the normalized plastic zone size at the right tip decrease with the increasing coating layer thickness b/a . While when the inclusion is "softer" than the coating phase, these quantities increase with the increasing b/a . The curvilinear trend of normalized plastic zone size at the left crack tip is converse.

3. For the influence of the coating phase, when the thickness is fixed ($b/a = 1.1$ for instance), a lower shear modulus will induce to smaller normalized SIF (for both the left and right tips) and smaller normalized plastic zone size at the right (the sharp) crack tip, but larger normalized plastic zone size at the left (blunt) tip. When the shear modulus ratio is fixed ($\mu_2/\mu_3 = 1.86$), a smaller coating phase thickness causes smaller normalized SIF (for the both crack tips) and smaller normalized plastic zone size at the right tip, but larger normalized plastic zone

size at the left tip, under the condition that the inclusion is "softer" than coating. When the inclusion is "harder" than coating, the situation is contrary.

Chapter 6 Crack-inclusion Interaction in Three-phase Fibers-reinforced Composites with Plastic Zone Correction

6.1. Introduction

As reviewed in the previous chapters, an appealing property of fibers-reinforced composites is their high specific strength (strength per unit weight), which is credited to the reinforcing fibers (the inclusions) intentionally introduced into the matrix. Dislocations and cracks are usually very easy to be formed near these inclusions because of stress concentration. It is of great importance to investigate the interaction between the dislocations/cracks and the near-by inclusions so that such matrix cracking problems can be analyzed more accurately.

In this chapter we study the mixed-mode fracture problem of a matrix crack interacting with multiple inclusions in fiber-reinforced composite, by applying the generalized Irwin model to evaluate the plastic zone size at the crack tips. We employ the famous three-phase cylindrical model to simulate the composite material. By employing the Von Mises yielding criterion, the stress intensity factor, plastic zone size and crack tip opening displacement at the crack tips are obtained for the current crack-inclusion interaction problem under mixed loading condition. The results obtained have taken the fiber concentration of the composite into account (through the three-phase cylindrical model), and are more accurate and realistic than the two-phase model where only a single inclusion is

considered to interact with the crack.

6.2. Problem formulation

The current physical problem to be solved is shown in Fig. 6.1, where the three-phase cylindrical composite model is used to represent the fiber-reinforced composite material. Phase 1 is the nearest inclusion (fiber) to the crack, occupies the area of $r < a$, phase 2 ($a < r < b$) is the pure matrix where the inclusion and the crack are embedded in. While the other inclusions and matrix part are replaced by an equivalent homogeneous media (the composite material), which is phase 3, occupies the area of $r > b$.

In Fig. 6.1(a), a radial crack with orientation angle θ is located in the matrix. r_1 and r_2 are the distance between the left and right ends of the crack to the inclusion center, respectively. The plastic zone ahead each crack tip is illustrated by bold line. An external uniform tension σ_0 is applied on the composite. By doing coordinate transformation, the crack is replaced to the $x-$axis as shown in Fig. 6.1(b), where $t_1 = r_1, t_2 = r_2$, respectively. The crack is loaded with a tensile stress $\sigma_{yy}(x,\theta)$ and a shear stress $\sigma_{xy}(x,\theta)$ related to the orientation angle θ. Thus the crack is under mixed-mode loading. The closure stress distribution from the current generalized Irwin model is given in Fig. 6.1(c) and the crack tip opening displacement at each crack tip is depicted in Fig. 6.2.

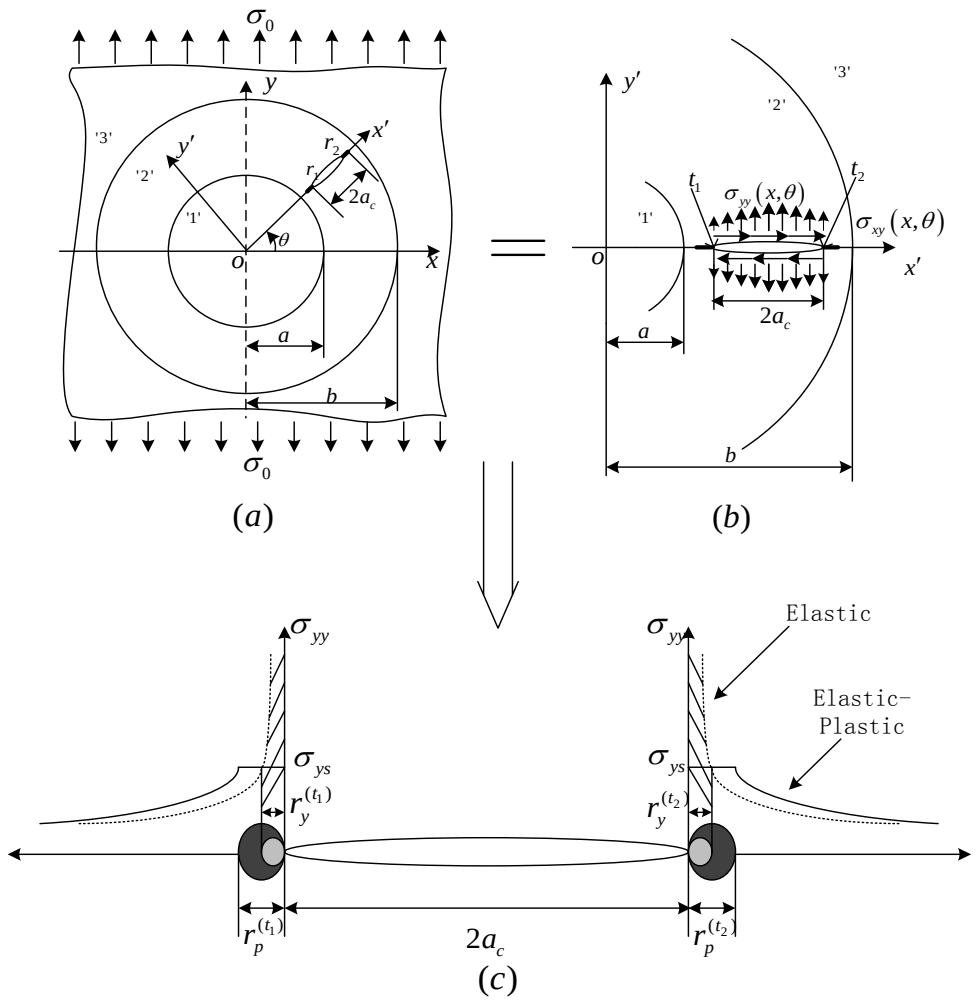

Fig. 6.1 (a) A radial crack in the three-phase cylinder composites under infinity uniaxial tensile loading; (b) Loading conditions on the crack faces with the generalized Irwin plastic zone correction; (c) The generalized Irwin model: plastic zones ahead the crack tips.

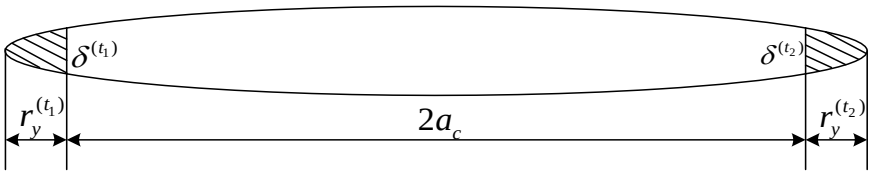

Fig. 6.2 The crack tip opening displacement in generalized Irwin model.

6.2.1. Crack simulation with distributed dislocation method

The stress solution for a single edge dislocation locates in the three-phase composite (shown in Fig. 6.3) is used as a Green function solution for the current problem: the crack is simulated by distributed dislocation pile-up and the stress

fields are given by the following singular integral equations (Hoh et al.[119]):

$$\begin{cases} \sigma_{yy}(x,\theta) = -\dfrac{2\mu_2}{(\kappa_2+1)\pi}\left[\displaystyle\int_{t_1}^{t_2}\frac{B_y(\xi)}{\xi-x}d\xi + \int_{t_1}^{t_2}k_1(x,\xi)B_y(\xi)d\xi\right], \quad t_1 \le x \le t_2 \\ \sigma_{xy}(x,\theta) = -\dfrac{2\mu_2}{(\kappa_2+1)\pi}\left[\displaystyle\int_{t_1}^{t_2}\frac{B_x(\xi)}{\xi-x}d\xi + \int_{t_1}^{t_2}k_2(x,\xi)B_x(\xi)d\xi\right], \quad t_1 \le x \le t_2 \end{cases} \tag{6.1}$$

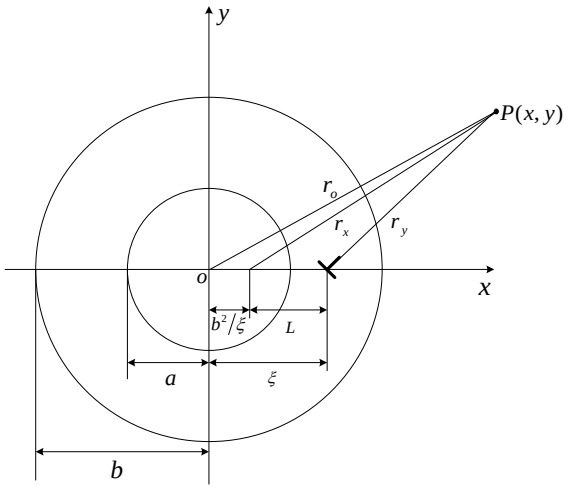

Fig. 6.3 An edge dislocation in a three-phase cylinder composite.

The left-hand sides of Eq. (6.1) are the traction components induced by the external loading:

$$\sigma_{yy}(x,\theta) = \frac{\sigma_0}{2K_{12}}\left\{\left[\left(\lambda_2+\mu_2\right)a_2 + \mu_2 a_3\frac{b^2}{x^2}\right] - \frac{\mu_2 K_{12}}{\mu_{12}}\left[-b_3 + 12b_4\frac{x^2}{b^2} + b_5\frac{b^4}{x^4}\right]\cos 2\theta\right\}, \tag{6.2}$$

$$\sigma_{xy}(x,\theta) = -\frac{\mu_2\sigma_0}{2\mu_{12}}\left[-b_3 + 6b_4\frac{x^2}{b^2} - 3b_5\frac{b^4}{x^4} - 2b_6\frac{b^2}{x^2}\right]\sin 2\theta \tag{6.3}$$

where $\lambda_2 = \dfrac{E_2\nu_2}{(1+\nu_2)(1-2\nu_2)}$, $\mu_2 = \dfrac{E_2}{2(1+\nu_2)}$ are Lame's constants. E_2 is the Young's modulus and ν_2 is the Poisson's ratio of phase 2. μ_{12} and K_{12} are the transverse shear modulus and plain strain bulk modulus determined by Christensen [69]:

$$K_{12}=k_2'+\frac{\mu_2}{3}+\frac{c}{1/\left[k_1'-k_2'+(\mu_1-\mu_2)/3\right]+(1-c)/(k_2'+4\mu_2/3)}, \tag{6.4}$$

where $k_i'=\lambda_i+2\mu_i/3, i=1,2$ .The constant $c=a^2/b^2$ represents the fiber concentration of the three-phase composite material and is the key parameter in the current study. The definition of the transverse shear modulus μ_{12} is given in Appendix B. The constants a_2, a_3, b_3, b_4, b_5 and b_6 are given by Luo [120].

The right-hand side of Eq. (6.1) is the traction induced by the distributed dislocations. $B_x(\xi)$ and $B_y(\xi)$ are the climb and glide dislocation densities in the crack zone, respectively. $\kappa_2=3-4\nu_2$. The kernel $k_1(x,\xi)$, $k_2(x,\xi)$ are given as:

$$\begin{aligned}k_1(x,\xi)=&\frac{A+B}{2\left(x-a^2/\xi\right)}-\frac{A+B}{2x}+A\frac{\xi^2-a^2}{\xi^3}\left(\frac{\xi^2}{a^2}-\frac{\xi^2-a^2}{x\xi-a^2}\right)\frac{a^2}{\left(x-a^2/\xi\right)^2}\\&-A\frac{a^2}{x^3}-\frac{1}{2\xi}\left(\frac{a}{x}\right)^2\left[A\left(\frac{2\xi^2}{a^2}-1\right)+B-2N\right]-Nb_0\frac{a}{x^2}\\&-\frac{1}{2a}\left\{\sum_{n=1}^{\infty}b_n(n+2)\left(\frac{x}{a}\right)^n-\sum_{n=1}^{\infty}\left[b_n(n-1)-b_{-n}\right]\left(\frac{x}{a}\right)^{n-2}\right\}\\&+\frac{1}{2a}\left\{\sum_{n=1}^{\infty}Ab_{-n}(n-2)\left(\frac{a}{x}\right)^n-\sum_{n=1}^{\infty}\left[Bb_n+A(n+1)b_{-n}\right]\left(\frac{a}{x}\right)^{n+2}\right\},\end{aligned} \tag{6.5}$$

$$\begin{aligned}k_2(x,\xi)=&\frac{A+B}{2\left(x-a^2/\xi\right)}-\frac{A+B}{2x}+A\frac{\xi^2-a^2}{\xi^2}\frac{x-\xi}{x\xi-a^2}\frac{a^2}{\left(x-a^2/\xi\right)^2}-\frac{B-A}{2\xi}\left(\frac{a}{x}\right)^2\\&+A\frac{a^2}{x^3}-\frac{1}{2a}\left\{\sum_{n=1}^{\infty}b_n'n\left(\frac{x}{a}\right)^n-\sum_{n=1}^{\infty}\left[b_n'(n-1)-b_{-n}'\right]\left(\frac{x}{a}\right)^{n-2}\right\}\\&+\frac{1}{2a}\left\{\sum_{n=1}^{\infty}Ab_{-n}'n\left(\frac{x}{a}\right)^n-\sum_{n=1}^{\infty}\left[Bb_{-n}'(n+1)-Ab_n'\right]\left(\frac{a}{x}\right)^{n+2}\right\},\end{aligned} \tag{6.6}$$

where $A=\dfrac{\mu_2-\mu_1}{\mu_2+\mu_1\kappa_2}$, $B=\dfrac{\mu_2\kappa_1-\mu_1\kappa_2}{\mu_2\kappa_1+\mu_1}$, $N=\dfrac{\mu_2(\kappa_1-1)-\mu_1(\kappa_2-1)}{\mu_2(\kappa_1-1)+2\mu_1}$. The

constants a_n, b_n, a_n' and b_n' can be found in the work of Luo and Chen [71].

Furthermore, for a Griffith crack, the zero net-dislocation condition in the crack leads to:

$$\int_{t_1}^{t_2} B_y(\xi)\,d\xi = 0, \int_{t_1}^{t_2} B_x(\xi)\,d\xi = 0. \tag{6.7}$$

Solving the singular integral equations of (6.1) and (6.7) numerically[80], the mode I and mode II stress intensity factors are finally obtained based on the solutions of the dislocation density as following:

$$\begin{aligned} K_I^{(t_1)} &= \lim_{\xi\to t_1} \frac{-2\mu_2\sqrt{2\pi}}{\kappa_2+1}\sqrt{\xi-t_1}B_y(x), K_I^{(t_2)} = \lim_{\xi\to t_2} \frac{2\mu_2\sqrt{2\pi}}{\kappa_2+1}\sqrt{t_2-\xi}B_y(x), \\ K_{II}^{(t_1)} &= \lim_{\xi\to t_1} \frac{-2\mu_2\sqrt{2\pi}}{\kappa_2+1}\sqrt{\xi-t_1}B_x(x), K_{II}^{(t_2)} = \lim_{\xi\to t_2} \frac{2\mu_2\sqrt{2\pi}}{\kappa_2+1}\sqrt{t_2-\xi}B_y(x). \end{aligned} \tag{6.8}$$

6.2.2. Generalized Irwin plastic zone size and CTOD

After the stress intensity factors at each crack tip have been obtained, the stress field ahead of crack tips can be written as:

$$\sigma_{xx}^{(t_m)} = \sigma_{yy}^{(t_m)} = \frac{K_I^{(t_m)}}{\sqrt{2\pi r^{(t_m)}}}, \sigma_{xy}^{(t_m)} = \frac{K_{II}^{(t_m)}}{\sqrt{2\pi r^{(t_m)}}}, \sigma_{zz}^{(t_m)} = \frac{2\nu_2 K_I^{(t_m)}}{\sqrt{2\pi r^{(t_m)}}}, \quad m = 1, 2. \tag{6.9}$$

Here, (t_1) and (t_2) represent the left and right crack tips, respectively. $K_I^{(t_m)}$ and $K_{II}^{(t_m)}$ are the mode I and mode II stress intensity factors near crack tip (t_m). ν_2 is the Poisson's ratio of phase 2. Plain strain condition is considered in this work. To estimate the plastic zone size around the crack tips, the von Mises criterion is used. Yielding occurs when the effective stress reaches the yield stress $\sigma_e = \sigma_{ys}$,

$$\sigma_e^{(t_m)}=\sqrt{\frac{\left(\sigma_{xx}^{(t_m)}-\sigma_{yy}^{(t_m)}\right)^2+\left(\sigma_{xx}^{(t_m)}-\sigma_{zz}^{(t_m)}\right)^2+\left(\sigma_{yy}^{(t_m)}-\sigma_{zz}^{(t_m)}\right)^2+6\left(\sigma_{xy}^{(t_m)2}\right)}{2}}=\sigma_{ys},$$

(6.10)

$\sigma_e^{(t_m)}$ is the effective stress near crack tip $\left(t_m\right)$. σ_{ys} is the yield stress.

Substituting Eq. (6.9) into (6.10):

$$\sigma_e^{(t_m)}=\frac{K_e^{(t_m)}}{\sqrt{2\pi r^{(t_m)}}},\tag{6.11}$$

where

$$K_e^{(t_m)}=\sqrt{\left(1-2\nu_2\right)^2\left(K_I^{(t_m)}\right)^2+3\left(K_{II}^{(t_m)}\right)^2}.\tag{6.12}$$

From Eqs. (6.10) and (6.11), we can obtain the plastic zone size under generalized Irwin model as:

$$r_y^{(t_m)}=\frac{1}{2\pi}\left(\frac{K_e^{(t_m)}}{\sigma_{ys}}\right)^2,\tag{6.13}$$

$$r_p^{(t_m)}=2r_y^{(t_m)}=\frac{1}{\pi}\left(\frac{K_e^{(t_m)}}{\sigma_{ys}}\right)^2,\tag{6.14}$$

where, $r_y^{(t_m)}$ is the first order estimation of plastic zone size at crack tip $\left(t_m\right)$ and $r_p^{(t_m)}$ is the second order estimation of plastic zone sizes.

The crack tip opening displacement CTOD which is denoted by $\delta^{(t_m)}$ as shown in Fig. 6.2, can thus be estimated by:

$$\delta^{(t_m)}=\frac{8}{E'}K_I^{(t_m)}\sqrt{\frac{r_y^{(t_m)}}{2\pi}},\tag{6.15}$$

where $K_I^{(t_m)}$ is the mode I stress intensity factor. $E'=E_2/\left(1-\nu_2^2\right)$ for plain strain. E_2 and ν_2 are the Young's modulus and Poisson's ratio of phase 2, respectively. Substituting the expression of plastic zone size into Eq.(6.15), we can have the final expression of CTOD in multi-phase composites as:

$$\delta^{(t_m)} = \frac{4}{\pi}\frac{K_I^{(t_m)}K_e^{(t_m)}}{E'\ \sigma_{ys}}. \tag{6.16}$$

6.2.3. The effective stress intensity factors.

In this section, the effective stress intensity factor is obtained when the plastic zone correction is taken into consideration. The iterative method is used to compute the effective stress intensity factor. Under the condition of small scale yielding, the effective half crack length of the radial crack can be approximated as:

$$a_{eff}^{(t_m)} = a_c + r_y^{(t_m)} = a_c + \frac{1}{2\pi}\left(\frac{K_e^{(t_m)}}{\sigma_{ys}}\right)^2, \tag{6.17}$$

where a_c is the half crack length as shown in Fig. 1. $r_y^{(t_m)}$ is the first order estimation of plastic zone size near crack tip (t_m) which can be obtained from Eq.(6.13).

Hence, the left and right crack tips are at the positions of:

$$t_1' = t_1 - r_y^{(t_1)},\ t_2' = t_2 - r_y^{(t_2)}, \tag{6.18}$$

$$t_2' - t_1' = \sum_{m=1}^{2} a_{eff}^{(t_m)}, \tag{6.19}$$

where t_1, t_2 are the positions of the left and right crack tips without considering the plastic zone size. t_1' , t_2' are the new positions of crack tips under the generalized Irwin model.

With the plastic zone correction, the singular integral equation (6.1) and zero net dislocation condition in Eq. (6.7) are modified into：

$$\begin{cases} \sigma_{yy}\left(x,\theta\right)=-\dfrac{2\mu_2}{\left(\kappa_2+1\right)\pi}\left[\displaystyle\int_{t_1'}^{t_2'}\frac{B_y(\xi)}{\xi-x}d\xi+\int_{t_1'}^{t_2'}k_1(x,\xi)B_y(\xi)d\xi\right], & t_1'\le x\le t_2' \\ \sigma_{xy}\left(x,\theta\right)=-\dfrac{2\mu_2}{\left(\kappa_2+1\right)\pi}\left[\displaystyle\int_{t_1'}^{t_2'}\frac{B_x(\xi)}{\xi-x}d\xi+\int_{t_1'}^{t_2'}k_2(x,\xi)B_x(\xi)d\xi\right], & t_1'\le x\le t_2' \end{cases} \tag{6.20}$$

$$\int_{t_1'}^{t_2'}B_y\left(\xi\right)d\xi=0,\int_{t_1'}^{t_2'}B_x\left(\xi\right)d\xi=0. \tag{6.21}$$

By solving Eq. (6.20), the effective stress intensity factors can be obtained finally:

$$\begin{aligned} &K_I^{eff,(t_1')}=-\lim_{\xi\to t_1'}\frac{2\mu_2\sqrt{2\pi}}{\kappa_2+1}\sqrt{\xi-t_1'}B_y^{eff}\left(x\right),K_I^{eff,(t_2')}=\lim_{\xi\to t_2'}\frac{2\mu_2\sqrt{2\pi}}{\kappa_2+1}\sqrt{t_2'-\xi}B_y^{eff}\left(x\right), \\ &K_{II}^{eff,(t_1')}=-\lim_{\xi\to t_1'}\frac{2\mu_2\sqrt{2\pi}}{\kappa_2+1}\sqrt{\xi-t_1'}B_x^{eff}\left(x\right),K_{II}^{eff,(t_2')}=\lim_{\xi\to t_2'}\frac{2\mu_2\sqrt{2\pi}}{\kappa_2+1}\sqrt{t_2'-\xi}B_x^{eff}\left(x\right). \end{aligned} \tag{6.22}$$

The effective dislocation densities $B_x^{eff}\left(x\right)$ and $B_y^{eff}\left(x\right)$ can be solved by the procedure given in the previous section.

6.3. Numerical examples and discussions

Based on the analytical results, numerical examples are given for various materials parameters and geometric configurations. To emphasize the influence of the crack orientation angle and the material constants on the crack, the plastic zone size and CTOD are normalized by:

$$r_{y0}=\frac{\left(K_0^e\right)^2}{2\pi\sigma_{ys}^2},\delta_{y0}=\frac{4K_0K_0^e}{\pi E'\sigma_{ys}}, \tag{6.23}$$

where $K_0=\sigma_0\sqrt{\pi a_c}$, $K_0^e=(1-2\nu_2)K_0$. K_0 , r_{y0} and δ_{y0} are the respective mode I stress intensity factor, plastic zone size and CTOD for the same size crack in a homogenous material (the pure matrix material) with the same external loading.

The Poisson's ratios in the following examples are taken as: $\nu_1 = \nu_2 = 1/3$.

6.3.1. Influence of the crack orientation angle and the fiber volume fraction (fiber concentration)

The orientation angle θ has great effect on the traction components distribution. To study the influence of θ on the normalized plastic zone size and normalized CTOD, we set the shear modulus ratio μ_1/μ_2 =15. The crack-inclusion distance is set at $(t_1 - a)/a_c = 4/3$, with the inclusion size $a/a_c = 20/3$.The fiber volume fraction (fiber concentration) $c = (a/b)^2$ takes a series of values from 0.01 to 0.4.

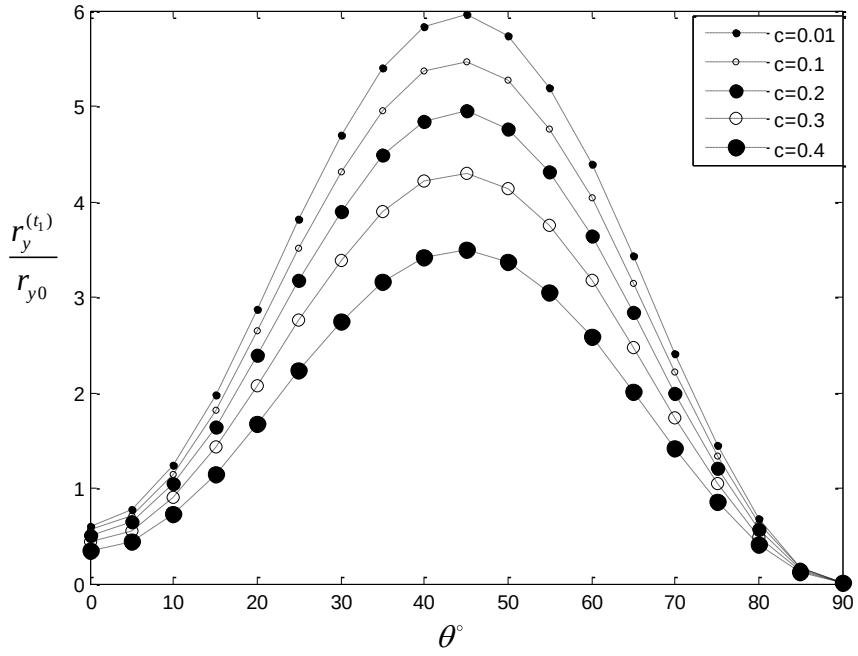

6.4(a)

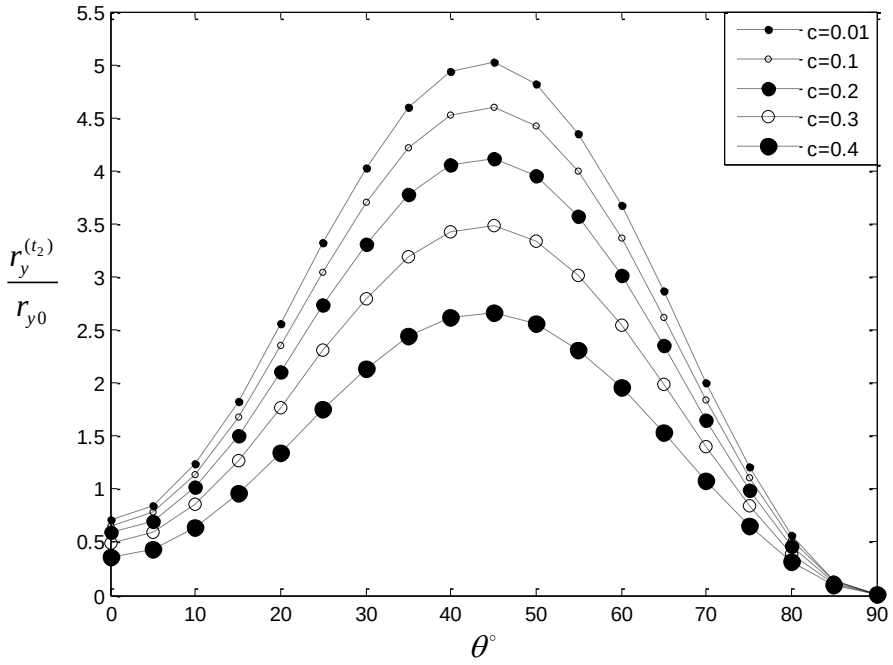
c=0.01
c=0.1
c=0.2
c=0.3
c=0.4
$\frac{r_y^{(t_2)}}{r_{y0}}$
θ°

6.4(b)

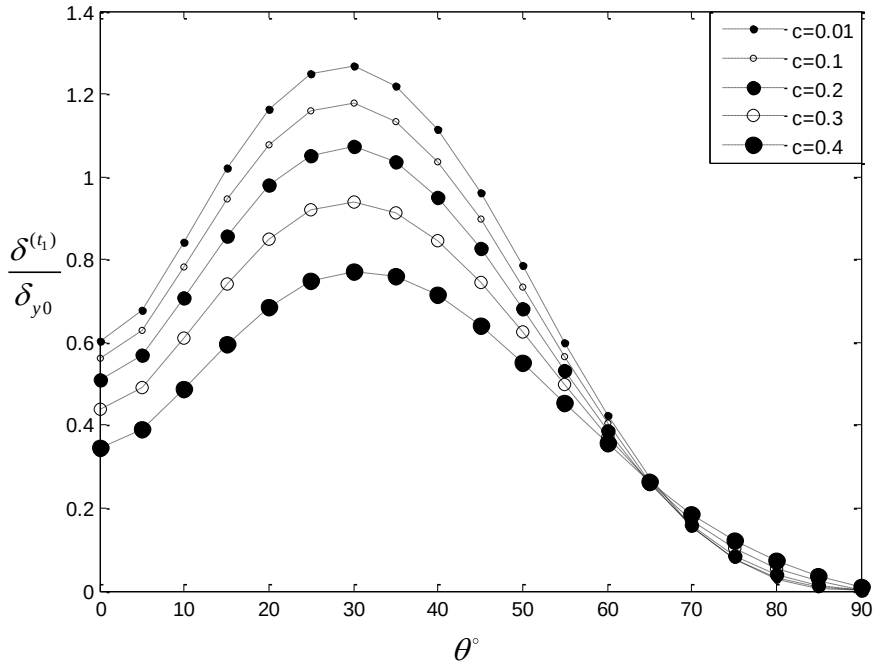
c=0.01
c=0.1
c=0.2
c=0.3
c=0.4
$\frac{\delta^{(t_1)}}{\delta_{y0}}$
θ°

6.4(c)

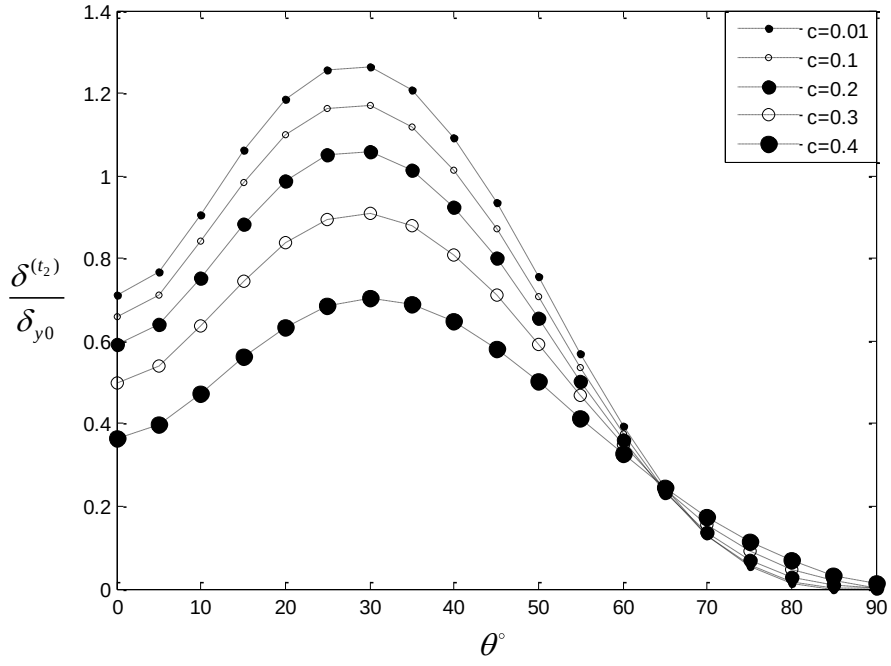

6.4(d)

Fig. 6.4 Effect of the crack orientation angle and fiber concentration on the normalized PZS and normalized CTOD with $\mu_1/\mu_2 = 15,\ (t_1 - a)/a_c = 4/3,\ a/a_c = 20/3$: (a) The normalized PZS at the left crack tip; (b) The normalized PZS at the right crack tip; (c) The normalized CTOD at the left crack tip; (d) The normalized CTOD at the right crack tip.

The curves of normalized plastic zone size ($\frac{r_y^{(t_m)}}{r_{y0}}$) and normalized CTOD ($\frac{\delta^{(t_m)}}{\delta_{y0}}$) are shown in Fig. 6.4. Based on Eqs. (6.12), (6.13), (6.16) and (6.23), we have

$$\frac{r_y^{(t_m)}}{r_{y0}} = \frac{(1-2\nu_2)^2\left(K_I^{(t_m)}\right)^2 + 3\left(K_{II}^{(t_m)}\right)^2}{(1-2\nu_2)^2 K_0^2}, \quad \frac{\delta^{(t_m)}}{\delta_{y0}} = \frac{K_I^{(t_m)}}{K_0}\sqrt{\frac{r_y^{(t_m)}}{r_{y0}}}. \tag{6.24}$$

The results show that under the conditions of plain strain and mixed mode loading, the Poisson's ratio of the matrix ν_2 magnifies the influence of $K_{II}^{(t_m)}$ on the normalized plastic zone size and normalized CTOD. Figs. 6.4(a) and 6.4(b) show the influence of orientation angle θ and the fiber concentration c on the

normalized plastic zone sizes of the both crack tips. We can find that the normalized plastic zone size at the both crack tips approach the maximum values at $\theta = 45^{\circ}$, since the traction component $\sigma_{xy}(x,\theta)$ reaches its maximum value at this point. Owing to the influence of ν_2, the value of $\frac{r_y^{(t_m)}}{r_{y0}}$ could be much larger than 1 in some θ values as shown in the figures. Figures 6.4(c) and 6.4(d) illustrate the curves of the normalized CTOD. At the both crack tips, the normalized CTOD increases first and then decreases with the increasing angle θ. Furthermore, increasing the fiber concentration $c, \left(c = (a/b)^2\right)$, which means the influence of the inclusion (phase 1) and the equivalent media (phase 3) are easier to be felt by the crack, the normalized plastic zone size and normalized CTOD decrease accordingly.

By comparisons among Figs. 6.4(a) and 6.4(b), 6.4(c) and 6.4(d), the curves of the normalized values at the left crack tip (t_1) and the right crack tip (t_2) share similar characteristics and traits. As a consequence, only the results at the left crack tip (t_1) are demonstrated in the subsequent numerical examples.

6.3.2. Influence of shear modulus ratio and fiber concentration

To study the effect of the materials properties on the crack, the influence of the shear modulus ratio μ_1/μ_2 (inclusion/matrix) and fiber concentration c on the crack are examined. The other parameters are set as: $(t_1 - a)/a_c = 4/3$, $a/a_c = 20/3, \theta = 10^{\circ}$.

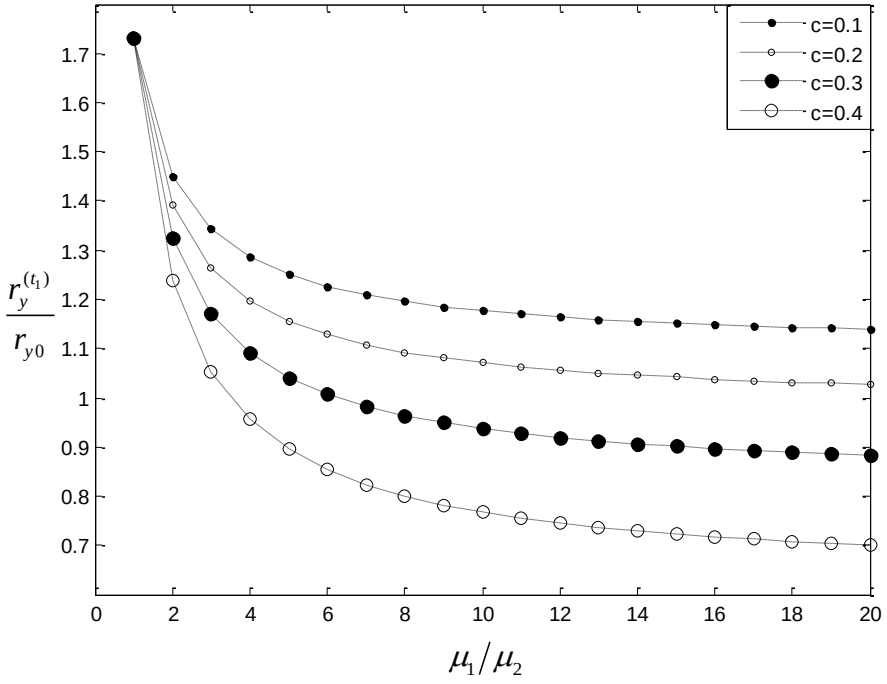

6.5(a)

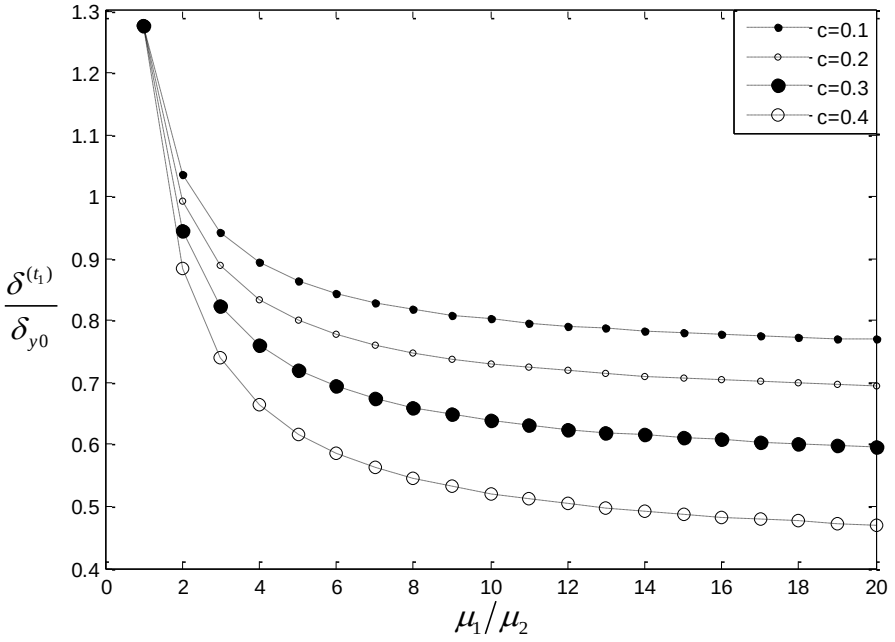

6.5(b)

Fig. 6.5 Effect of the shear modulus ratio and fiber concentration on the normalized PZS and normalized CTOD for a "harder" inclusion ($\mu_1 > \mu_2$), with $\theta = 10^\circ$, $(t_1 - a)/a_c = 4/3$, $a/a_c = 20/3$: (a) The normalized PZS at the left crack tip; (b) The normalized CTOD at the left crack tip.

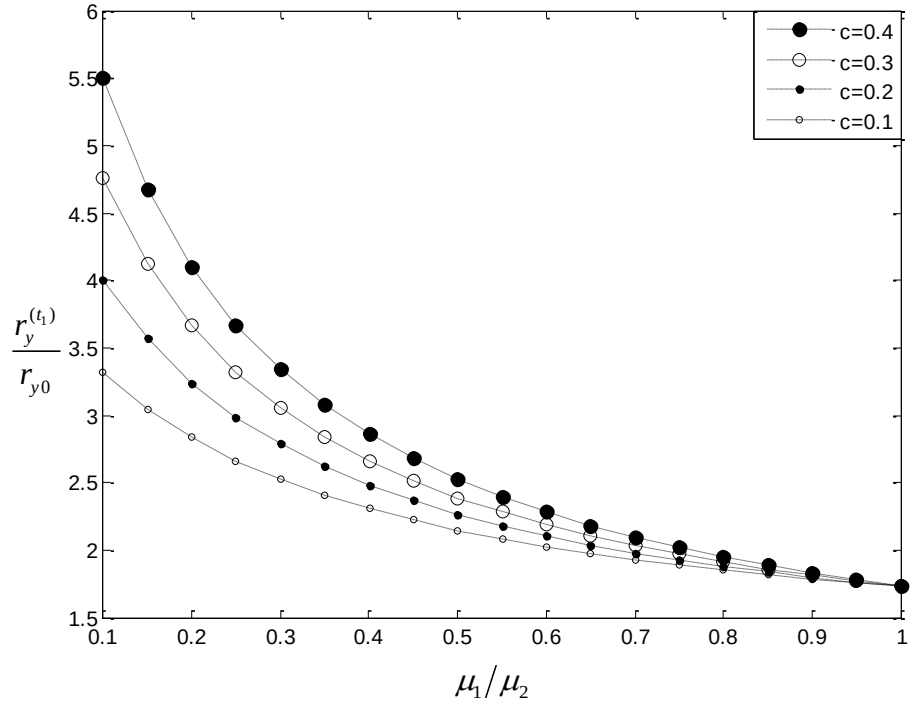

6.6(a)

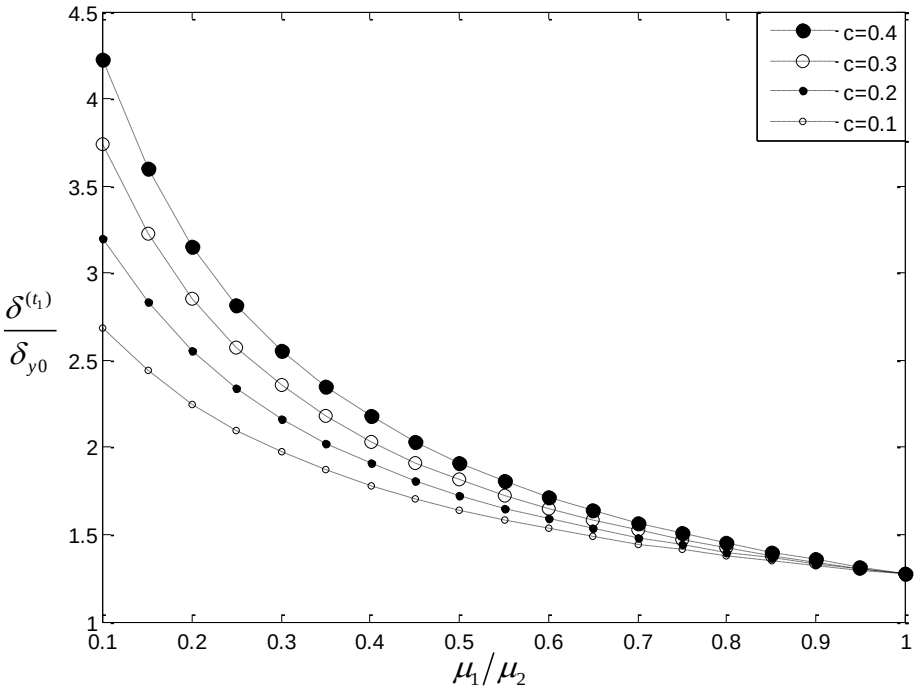

6.6(b)

Fig. 6.6 Effect of the shear modulus ratio and fiber concentration on the normalized PZS and normalized CTOD for a "softer" inclusion ($\mu_1 < \mu_2$),with $\theta = 10^{\circ}$, $(t_1 - a)/a_c = 4/3$, $a/a_c = 20/3$: (a) The normalized PZS at the left crack tip; (b) The normalized CTOD at the left crack tip.

The normalized plastic zone size and normalized CTOD are depicted in Figs.

6.5(a) to 6.5(b), respectively, for the left crack tip when the inclusion is "harder" than the matrix ($\mu_1/\mu_2 > 1$). According to the curves, we can find that the normalized values $\frac{r_y^{(t_m)}}{r_{y0}}$ and $\frac{\delta^{(t_m)}}{\delta_{y0}}$ decrease with the increasing modulus ratio μ_1/μ_2 . It means that a "harder" inclusion is able to shield the crack from propagation. On the other hand, when the inclusion is "softer" than the matrix ($\mu_1/\mu_2 < 1$) as shown in Figs. 6.6(a)-6.6(b), both the normalized values $\frac{r_y^{(t_m)}}{r_{y0}}$ and $\frac{\delta^{(t_m)}}{\delta_{y0}}$ increase. Hence, a "softer" inclusion makes the crack easier to propagate.

Moreover, our numerical results also show that a higher fiber concentration c decreases the normalized plastic zone size and normalized CTOD in the case of "harder" inclusions. Physically, a higher concentration of strong fibers increases the fracture toughness. For the "softer" inclusion case (the fiber is weaker than the matrix in terms of shear modulus), the influence of higher fiber concentration is negative: increasing the fiber concentration c leads to larger normalized plastic zone size and normalized CTOD.

6.3.3. Normalized CTOD for porous materials at different concentrations and verification

The normalized CTOD for an extreme case: porous medium ($\mu_1/\mu_2 = 0$) is given in Table 6.1. The orientation angle θ is zero here. Other parameters keep consistent with the previous cases. According to the table, we can find that for the case of porous medium, a higher concentration of porosities could result to

larger normalized CTOD, which is similar to the conclusion given in Sect. 6.3.2., in the case of "softer" inclusion. This is due to the fact that the porosities decrease the strength of the equivalent media (phase 3).

b/a		4	3	2.2	1.7
C		0.0625	0.1111	0.2066	0.3460
$\frac{\delta^{(t_1)}}{\delta_{y0}}$	Current	2.7660	3.1152	3.9530	5.0488
	Hoh[119]	2.4878	2.8308	3.6647	4.7010
$\frac{\delta^{(t_2)}}{\delta_{y0}}$	Current	2.2467	2.5172	3.0882	3.2745
	Hoh[119]	1.9923	2.2467	2.8191	2.9710

Table 6.1 Normalized CTOD value $\delta^{(t_m)}/\delta_{y0}$ for the porous cases: $\mu_1/\mu_2 = 0, \theta = 0,$ $(t_1 - a)/a_c = 4/3, a/a_c = 20/3.$

In the table, comparison has been made between the current work and Hoh's work[119] which is based on the Dugdale model. The table shows that our results obtained from the generalized Irwin model can match well with the results from Dugdale model. But the current generalized Irwin model is much more efficient than Dugdale model in terms of computation time.

6.3.4. The influence of crack orientation angle and fiber concentration on the normalized effective stress intensity factors

The effective stress intensity factor is obtained by the iterative method given in Section 6.2.3. as shown in Eq. (6.22). The plastic zone correction is considered at both crack tips with the first order estimation. In this section, The SIFs are normalized as $\frac{K_I^{eff,(t_m)}}{K_I^{(t_m)}}$ and $\frac{K_{II}^{eff,(t_2)}}{K_{II}^{(t_2)}}$ to explore the difference between the elastic results without plastic zone correction and the current results. The

other parameters are set as: $\mu_1 = 15\mu_2$ ("harder" inclusion case), $a/a_c = 20/3$, $(t_1 - a)/a_c = 4/3$, while $c = 0.1 \sim 0.4$ and orientation angle θ varies from 0° to 90°.

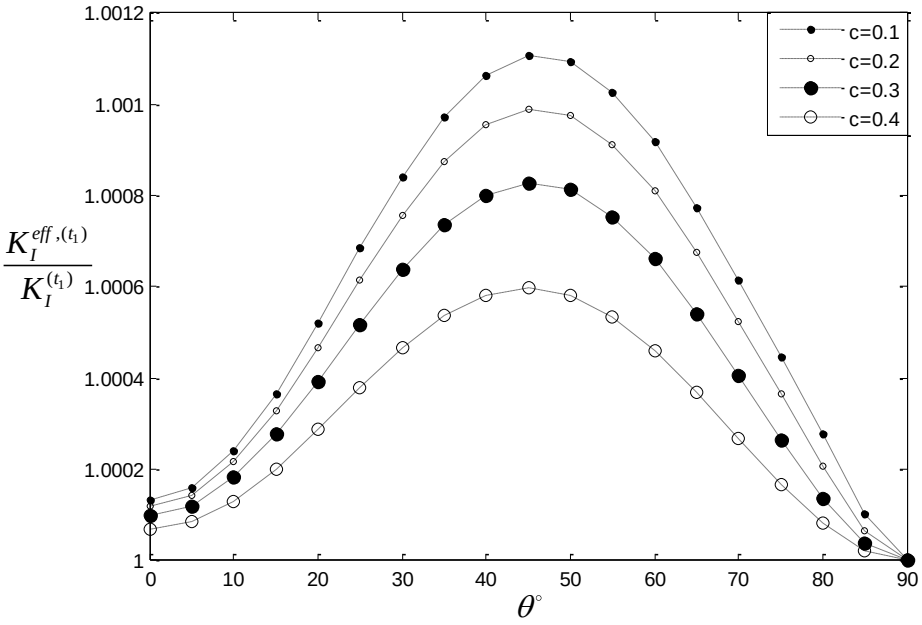

6.7(a)

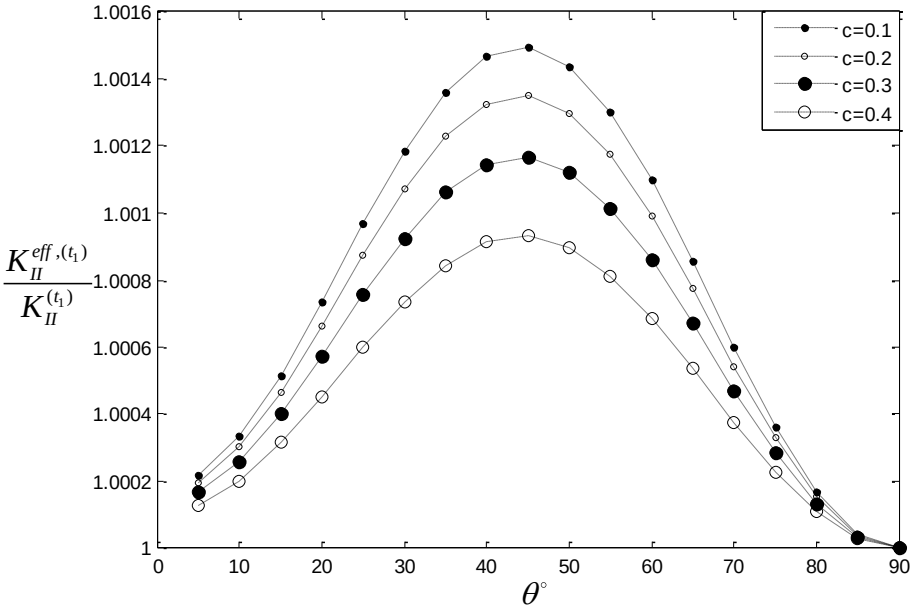

6.7(b)

Fig.6.7 Variation of the effective stress intensity factors with $\mu_1 = 15\mu_2$, $(t_1 - a)/a_c = 4/3$, $a/a_c = 20/3$: (a) Effective stress intensity factor (mode I) at the left crack tip; (b) Effective stress intensity factor (mode II) at the left crack tip.

The normalized effective mode I and mode II stress intensity factors at the left crack tips are given in Figs. 6.7(a) and 6.7(b). At $\theta = 45^{\circ}$, the orientation angle has the greatest influence on the normalized values and the maximum values of the SIFs.

6.4. Conclusions

In this chapter, the problem of a matrix crack interacting with multiple inclusions in fiber-reinforced composites has been investigated by using the generalized Irwin approach. Various numerical examples are presented to explore the influence of the crack orientation angle, shear modulus ratio of the inclusion and matrix, as well as the fiber concentration, on the normalized values of plastic zone size and crack tip opening displacement. It is found that the crack orientation angle has great effect on the plastic zone size and CTOD. As for the fiber concentration and shear modulus ratio, for a "softer" inclusion ($\mu_1 < \mu_2$), the effect of the inclusions on the crack tips is anti-shielding, which means when the shear modulus ratio (μ_1/μ_2) decreases, the normalized plastic zone size and normalized CTOD will increase. In the meantime, a lager fiber concentration c will induce to larger normalized values of CTOD. In contrast, for a "harder" inclusion ($\mu_1 > \mu_2$), both the plastic zone size and CTOD will decrease with increasing either the shear modulus ratio or the fiber concentration. In other words, "harder" inclusions shield the crack from propagation.

Chapter 7 Fracture Behavior Investigation for a Pileup of Edge Dislocations Interacting with a Nanoscale Inhomogeneity with Interface and Size Effects

7.1. Introduction

In the previous chapters, crack-inclusion interaction problems in fibers-reinforced composite materials have been investigated for the cases when the crack is in inclusion/matrix system (2-phase), coated inclusion/matrix system (3-phase) and multiple inclusion/matrix system, in which the interface effect of the inclusion is not considered as the composite structure has a relative large configuration (in micro level). In this chapter, the elastic-plastic fracture behavior of a Zener-Stroh crack near a nano-sized circular inclusion is investigated. The plastic zone size and CTOD are estimated by considering the interface effect of the inclusion/matrix and the inclusion size. In certain situations, such as solids with smaller grain size, micro cracks in terms of Zener-Stroh cracks are often initiated due to dislocations pie-up at grain boundaries. High-density ensembles of grain boundaries lead to frequent occurrences of dislocation pile-up which are the potential sources of crack nucleuses; Besides, at each boundary, the amount of possible pile up of dislocations are small. It becomes harder for dislocations to be repelled by overcoming the energy barrier across a boundary for diffusion. To study Zener-Stroh cracks' behaviors in nano-scale structures is thus very important for failure analysis and prevention purpose of nano composites. For a

nanoscale inhomogeneity (inclusion), the size and interface properties have great influence on the fracture behavior of the crack, which is completely different to a classical crack-inclusion interaction problem. In this chapter, the influence of inclusion/matrix interface and inclusion size on the PZS and CTOD are investigated by the generalized Irwin model. The effect of sharp crack tip position (where the crack propagation usually occurs) is emphasized.

7.2. Problem description

The physical problem to be investigated is shown in Figure 7.1, where an infinite elastic medium contains a circular nanoscale inhomogeneity and a nearby Zener-Stroh crack nucleated by pileup of distributed edge dislocations. The crack is located in the matrix (μ_2, κ_2) from t_1 to t_2 with a crack length $2a_c$ along the *x*-axis. The circular nanoscale inhomogeneity has a radius *R* with material properties (μ_1, κ_1), where $\mu_j\ (j=1,2)$ is the shear modulus and $\kappa_j = 3-4\nu_j$ for plain strain state, ν_j is the Poisson's ratio of each material. The interface effects must be considered for this nanoscale problem.

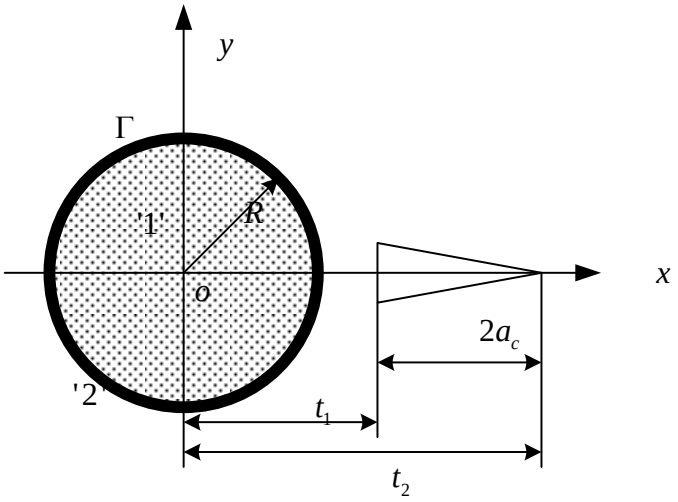

Fig. 7.1 The current physical problem: A Zener-Stroh crack near a nano inhomogeneity with interface effect

7.2.1. The stress field for a single edge dislocation near a nano inhomogeneity

An edge dislocation with Burgers vector $\left(b_x^T, b_y^T\right)$ located at $z_0 = x_0 + iy_0$ near a nano inhomogeneity is shown in Fig. 7.2. The regions occupied by the inhomogeneity and the matrix are denoted by S^+ and S^-, respectively. Noting that the inclusion/matrix interface effect cannot be ignored, we apply the Gurtin-Murdoch model [121-123]. The elastic field of the bulk solid is described by the differential equations of classical elasticity, and the interface has its own elastic constants: μ^0 and λ^0 which are the interface Lame constants, and is characterized by an additional constitutive law:

$$\sigma_{\theta\theta}^0 = \left(2\mu^0 + \lambda^0\right)\varepsilon_{\theta\theta}^0, \tag{7.1}$$

where $\sigma_{\theta\theta}^0$ and $\varepsilon_{\theta\theta}^0$ are the interface stress and strain respectively. Meanwhile, as a plane elasticity problem, the interface conditions on the interface can be summarized as:

$$u_{x1}^+(t) = u_{x2}^-(t), u_{y1}^+(t) = u_{y2}^-(t), \tag{7.2}$$

$$\sigma_{rr1}^{+}(t)-\sigma_{rr2}^{-}(t)=-\frac{\sigma_{\theta\theta}^{0}}{R},\sigma_{r\theta1}^{+}(t)-\sigma_{r\theta2}^{-}(t)=\frac{1}{R}\frac{\partial\sigma_{\theta\theta}^{0}}{\partial\theta}. \tag{7.3}$$

Here, u_x and u_y are displacement components in the Cartesian coordinate and $\sigma_{rr},\sigma_{r\theta}$ are the stress components in polar coordinate, respectively. The subscript '1' represent the inhomogeneity and '2' represents the matrix, respectively.

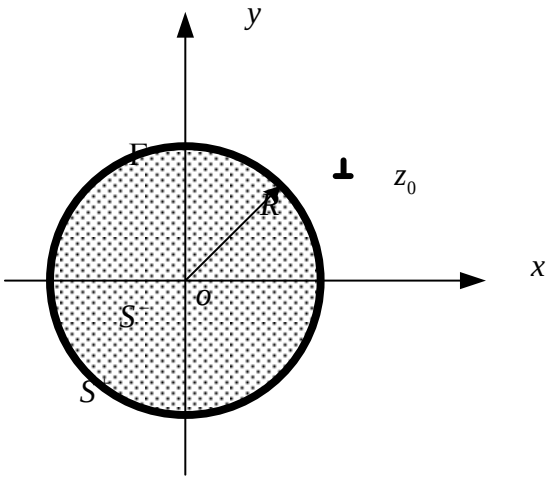

Fig. 7.2 A single edge dislocation interacting with a nano inhomogeneity

The present interface Γ is assumed to be a coherent interface [124] so that the interface strain $\varepsilon_{\theta\theta}^{0}$ equals to that of the bulk material:

$$\varepsilon_{\theta\theta}^{0}=\varepsilon_{\theta\theta1}=\frac{\lambda_1+2\mu_1}{4\mu_1(\lambda_1+\mu_1)}\sigma_{\theta\theta1}-\frac{\lambda_1}{4\mu_1(\lambda_1+\mu_1)}\sigma_{rr1}. \tag{7.4}$$

Equation (7.4) is the constitutive equation for the bulk material (inhomogeneity). Substituting Eq. (7.4) into (7.3), we have:

$$\begin{aligned}\sigma_{rr1}^{+}(t)-\sigma_{rr2}^{-}(t)&=-\frac{\sigma_{\theta\theta}^{0}}{R}=-\frac{1}{R}\frac{2\mu^0+\lambda^0}{4\mu_1(\lambda_1+\mu_1)}\left[(\lambda_1+2\mu_1)\sigma_{\theta\theta1}-\lambda_1\sigma_{rr1}\right],\\ \sigma_{r\theta1}^{+}(t)-\sigma_{r\theta2}^{-}(t)&=\frac{1}{R}\frac{\partial\sigma_{\theta\theta}^{0}}{\partial\theta}=\frac{1}{R}\frac{2\mu^0+\lambda^0}{4\mu_1(\lambda_1+\mu_1)}\left[(\lambda_1+2\mu_1)\frac{\partial\sigma_{\theta\theta1}}{\partial\theta}-\lambda_1\frac{\partial\sigma_{rr1}}{\partial\theta}\right].\end{aligned} \tag{7.5}$$

This is the stress discontinuity conditions along the interface. λ_1 is the Lame

constant of the inhomogeneity.

The stress and displacement components can be expressed in term of two holomorphic complex potentials $\Phi(z)$ and $\Psi(z)$ [106]:

$$\sigma_{rr}+\sigma_{\theta\theta}=2\left[\Phi(z)+\overline{\Phi(z)}\right], \tag{7.6}$$

$$\sigma_{rr}+i\sigma_{r\theta}=\Phi(z)+\overline{\Phi(z)}-\bar{z}\overline{\Phi'(z)}-\frac{\bar{z}}{z}\Psi(z), \tag{7.7}$$

$$2\mu\left(u_x'+iu_y'\right)=iz\left[\kappa\Phi(z)-\overline{\Phi(z)}+\bar{z}\overline{\Phi'(z)}+\frac{\bar{z}}{z}\Psi(z)\right], \tag{7.8}$$

where $u_x'=\partial u_x/\partial\theta, u_y'=\partial u_y/\partial\theta, \Phi'(z)=d\left[\Phi(z)\right]/dz,$ the over bar is the complex conjugated. Solving Eqs. (7.6) to (7.8) with the help of (7.1) to (7.5), the holomorphic complex potentials $\Phi(z)$ and $\Psi(z)$ for the matrix can be obtained [125]:

$$\Phi_2(z)=\frac{\mu_2}{\mu_1\kappa_2}\sum_{k=1}^{+\infty}B_{-k}z^{-k}+\frac{\gamma_2}{z-z_0}+\frac{1}{\kappa_2}\left[\frac{\gamma_2}{z-z^*}-\frac{\gamma_2}{z}-\frac{\bar{\gamma}_2 z^*\left(z_0-z^*\right)}{\bar{z}_0\left(z-z^*\right)^2}\right], |z|>R, \tag{7.9}$$

$$\Psi_2(z)=\frac{R^2}{z^2}\left[\Phi_2(z)-z\Phi_2'(z)\right]+\frac{R^2}{z^2}\left\{\frac{\mu_2\kappa_1}{\mu_1}\left[\sum_{k=1}^{+\infty}\bar{A}_k\left(\frac{R^2}{z}\right)^k-\frac{\mu_1(1+\kappa_2)}{\mu_2\kappa_1+\mu_1(1+b)}\frac{\bar{\gamma}_2}{\bar{z}_0}\right]\right.$$
$$\left.-\frac{\kappa_2\bar{\gamma}_2 z}{R^2-z\bar{z}_0}+\frac{\bar{\gamma}_2 z z_0}{R^2(z-z_0)}+\frac{\bar{\gamma}_2 z}{R^2}+\frac{\gamma_2\overline{z^*}\left(\bar{z}_0-\overline{z^*}\right)z_0 z^2}{R^4(z-z_0)^2}-\frac{\mu_2(1+\kappa_1)(1+b)A_0}{\mu_2\kappa_1+\mu_1(1+b)}\right\}, \tag{7.10}$$

where $z^*=R^2/\bar{z}_0$, $\gamma_2=\frac{\mu_2}{\pi(1+\kappa_2)}\left(b_y^T-ib_x^T\right)$. Other coefficients in Eqs. (7.9) and (7.10) are given by Fang and Liu [125] as:

$$A_0=\frac{c_1}{(c_2)^2-1}\left(\frac{c_2\bar{\gamma}_2}{\bar{z}_0}+\frac{\gamma_2}{z_0}\right), B_0=-\bar{A}_0=-\frac{c_1}{(c_2)^2-1}\left(\frac{\bar{\gamma}_2}{\bar{z}_0}+\frac{c_2\gamma_2}{z_0}\right), \tag{7.11}$$

$$A_k = -\frac{1+\kappa_2}{c_3}\frac{\gamma_2}{\left(z_0\right)^{k+1}} + \frac{c_4}{c_3}\Big[\overline{\gamma}_2\left(\overline{z^*}\right)^{k-1}R^{-2k} - \overline{\gamma}_2 R^{-2k}\delta_{1k} - \frac{\gamma_2\overline{z^*}\left(\overline{z}_0 - \overline{z^*}\right)R^{-2k}\left(k-1\right)\left(\overline{z^*}\right)^{k-2}}{z_0}\Big], \quad k \geq 1, \tag{7.12}$$

$$B_{-k} = -\frac{c_6}{c_5}\frac{\overline{\gamma}_2 R^{2k}}{\left(\overline{z}_0\right)^{k+1}} - \frac{1+\kappa_2}{c_5\kappa_2}\Big[\gamma_2\left(z^*\right)^{k-1} - \gamma_2\delta_{1k} - \frac{\overline{\gamma}_2 z^*\left(z_0 - z^*\right)\left(k-1\right)\left(z^*\right)^{k-2}}{\overline{z}_0}\Big], \quad k \geq 1, \tag{7.13}$$

where

$$\begin{aligned}
&c_1 = \frac{\mu_1\left(1+\kappa_2\right)}{\mu_2\kappa_1 + \mu_1\left(1+b\right)}, c_2 = \frac{\mu_2 - \mu_1\left(1+b\right)}{\mu_2\kappa_1 + \mu_1\left(1+b\right)},\\
&c_3 = 1 + \left(a+b\right)\left(k+1\right) + \frac{\mu_1\kappa_1}{\mu_2} + \frac{a\left(a+b\right)\left(1+k\right)\left(1-k\right)}{1-a+ka+\mu_2/\left(\kappa_2\mu_1\right)},\\
&c_4 = \frac{\left(1+\kappa_2\right)a\left(1+k\right)}{\kappa_2\left[1-a+ka+\mu_2/\left(\kappa_2\mu_1\right)\right]}, c_6 = \frac{\left(1+\kappa_2\right)\left(a+b\right)\left(1-k\right)}{1+\left(a+b\right)\left(k+1\right)+\mu_2\kappa_1/\mu_1},\\
&c_5 = 1 + a\left(k-1\right) + \frac{\mu_2}{\mu_1\kappa_2} + \frac{a\left(a+b\right)\left(1+k\right)\left(1-k\right)}{1+\left(a+b\right)\left(k+1\right)+\mu_2\kappa_1/\mu_1},\\
&a = \frac{2\mu^0+\lambda^0}{4R\mu_1}, b = \frac{2\mu_1\left(2\mu^0+\lambda^0\right)}{4R\mu_1\left(\lambda_1+\mu_1\right)}, \delta_{ij} = \begin{cases}1, i = j\\ 0, i \neq j\end{cases}.
\end{aligned} \tag{7.14}$$

From Eqs. (7.9) and (7.10), the stress field due to a single edge dislocation at point z_0 can be obtained. Rewrite Eqs. (7.6) to (7.8) into Cartesian coordinate, the stress components in the matrix induced by the edge dislocation can be expressed as:

$$\begin{aligned}
\sigma_{xx}^{(2)} &= \mathrm{Re}\left[2\Phi_2(\mathrm{z}) - \overline{\mathrm{z}}\,\Phi_2'(\mathrm{z}) - \Psi_2\left(z\right)\right],\\
\sigma_{yy}^{(2)} &= \mathrm{Re}\left[2\Phi_2(\mathrm{z}) + \overline{\mathrm{z}}\,\Phi_2'(\mathrm{z}) + \Psi_2\left(z\right)\right],\\
\sigma_{xy}^{(2)} &= \mathrm{Im}\left[\overline{\mathrm{z}}\,\Phi_2'(\mathrm{z}) + \Psi_2\left(z\right)\right].
\end{aligned} \tag{7.15}$$

7.2.2. A Zener-Stroh crack near a nano inhomogeneity

The stress components due to a single edge dislocation near a nano inhomogeneity have been given in Eq. (7.15), which is used as a Green function solution for our current crack-inhomogeneity interaction problem. The Zener-Stroh crack is simulated by distributed dislocations. The crack is located along the *x*-axis, the complex variables in section 7.2.1 is simplified as:

$$z = x,\ z_0 = x_0,\ z^* = R^2/x_0 = x^*. \tag{7.16}$$

Substituting Eq. (7.16) into (7.9) and (7.10), we have:

$$\Phi_2(x) = \frac{\mu_2}{\mu_1\kappa_2}\sum_{k=1}^{+\infty} B_{-k}x^{-k} + \frac{\gamma_2}{x-x_0} + \frac{1}{\kappa_2}\left[\frac{\gamma_2}{x-x^*} - \frac{\gamma_2}{x} - \frac{\overline{\gamma}_2 x^*\left(x_0 - x^*\right)}{x_0\left(x-x^*\right)^2}\right], |x| > R, \tag{7.17}$$

$$\Psi_2(x) = \frac{R^2}{x^2}\left[\Phi_2(x) - x\Phi_2'(x)\right] + \frac{R^2}{x^2}\left\{\frac{\mu_2\kappa_1}{\mu_1}\left[\sum_{k=1}^{+\infty}\overline{A}_k\left(\frac{R^2}{x}\right)^k - \frac{\mu_1(1+\kappa_2)}{\mu_2\kappa_1+\mu_1(1+b)}\frac{\overline{\gamma}_2}{x_0}\right]\right.$$
$$\left. - \frac{\kappa_2\overline{\gamma}_2 x}{R^2 - xx_0} + \frac{\overline{\gamma}_2 x x_0}{R^2(x-x_0)} + \frac{\overline{\gamma}_2 x}{R^2} + \frac{\gamma_2 x^*\left(x_0 - x^*\right)x_0 x^2}{R^4\left(x-x_0\right)^2} - \frac{\mu_2(1+\kappa_1)(1+b)A_0}{\mu_2\kappa_1+\mu_1(1+b)}\right\}, \tag{7.18}$$

$$\Phi_2'(x) = \frac{\mu_2}{\mu_1\kappa_2}\sum_{k=1}^{+\infty}(-k)B_{-k}x^{-k-1} - \frac{\gamma_2}{\left(x-x_0\right)^2} + \frac{1}{\kappa_2}\left[-\frac{\gamma_2}{\left(x-x^*\right)^2} + \frac{\gamma_2}{x^2} + 2\frac{\overline{\gamma}_2 x^*\left(x_0 - x^*\right)}{x_0\left(x-x^*\right)^3}\right]. \tag{7.19}$$

Thus the Cartesian stress components in the matrix are:

$$\begin{aligned}\sigma_{xx}^{(2)}(x,0) &= \mathrm{Re}\left[2\Phi_2(x) - x\Phi_2'(x) - \Psi_2(x)\right] \\ &= H_{xx1}(x,x_0)\left(\frac{b_y^T}{x-x_0}\right) + H_{xx2}(x,x_0)b_y^T,\end{aligned} \tag{7.20}$$

$$\begin{aligned}\sigma_{yy}^{(2)}(x,0) &= \mathrm{Re}\left[\Phi_2(x)+x\Phi_2'(x)+\Psi_2(x)\right]\\ &= H_{yy1}(x,x_0)\frac{b_y^T}{x-x_0}+H_{yy2}(x,x_0)b_y^T\end{aligned} \tag{7.21}$$

$$\begin{aligned}\sigma_{xy}^{(2)}(x,0) &= \mathrm{Im}\left[x\Phi_2'(x)+\Psi_2(x)\right]\\ &= H_{xy1}(x,x_0)\frac{b_x^T}{x-x_0}+H_{xy2}(x,x_0)b_x^T.\end{aligned} \tag{7.22}$$

The coefficient functions are given as:

$$\begin{aligned}H_{xx1}(x,x_0) &= \left(3-\frac{R^2}{x^2}-\frac{x_0}{x}+\frac{x^*}{x}\right),\\ H_{xx2}(x,x_0) &= \left(2-\frac{R^2}{x^2}\right)\left(\frac{\mu_2}{\mu_1\kappa_2}\sum_{k=1}^{+\infty}B_{-k}^R x^{-k}+\frac{1}{\kappa_2}\left[\frac{1}{x-x^*}-\frac{1}{x}-\frac{x^*\left(x_0-x^*\right)}{x_0\left(x-x^*\right)^2}\right]\right)\\ &-\left(x-\frac{R^2}{x}\right)\left(\frac{\mu_2}{\mu_1\kappa_2}\sum_{k=1}^{+\infty}(-k)B_{-k}^R x^{-k-1}+\frac{1}{\kappa_2}\left[-\frac{1}{\left(x-x^*\right)^2}+\frac{1}{x^2}+2\frac{x^*\left(x_0-x^*\right)}{x_0\left(x-x^*\right)^3}\right]\right)\\ &-\frac{R^2}{x^2}\left\{\frac{\mu_2\kappa_1}{\mu_1}\left[\sum_{k=1}^{+\infty}\bar{A}_k^R\left(\frac{R^2}{x}\right)^k-\frac{\mu_1(1+\kappa_2)}{\mu_2\kappa_1+\mu_1(1+b)}\frac{1}{x_0}\right]-\frac{\kappa_2 x}{R^2-xx_0}+\frac{x}{R^2}-\frac{\mu_2(1+\kappa_1)(1+b)A_0^R}{\mu_2\kappa_1+\mu_1(1+b)}\right\},\end{aligned} \tag{7.23}$$

$$\begin{aligned}H_{yy1}(x,x_0) &= \left(1+\frac{R^2}{x^2}+\frac{x_0}{x}-\frac{x^*}{x}\right),\\ H_{yy2}(x,x_0) &= \left(2+\frac{R^2}{x^2}\right)\left(\frac{\mu_2}{\mu_1\kappa_2}\sum_{k=1}^{+\infty}B_{-k}^R x^{-k}+\frac{1}{\kappa_2}\left[\frac{1}{x-x^*}-\frac{1}{x}-\frac{x^*\left(x_0-x^*\right)}{x_0\left(x-x^*\right)^2}\right]\right)\\ &+\left(x-\frac{R^2}{x}\right)\left(\frac{\mu_2}{\mu_1\kappa_2}\sum_{k=1}^{+\infty}(-k)B_{-k}^R x^{-k-1}+\frac{1}{\kappa_2}\left[-\frac{1}{\left(x-x^*\right)^2}+\frac{1}{x^2}+2\frac{x^*\left(x_0-x^*\right)}{x_0\left(x-x^*\right)^3}\right]\right)\\ &+\frac{R^2}{x^2}\left\{\frac{\mu_2\kappa_1}{\mu_1}\left[\sum_{k=1}^{+\infty}\bar{A}_k^R\left(\frac{R^2}{x}\right)^k-\frac{\mu_1(1+\kappa_2)}{\mu_2\kappa_1+\mu_1(1+b)}\frac{1}{x_0}\right]-\frac{\kappa_2 x}{R^2-xx_0}+\frac{x}{R^2}-\frac{\mu_2(1+\kappa_1)(1+b)A_0^R}{\mu_2\kappa_1+\mu_1(1+b)}\right\},\end{aligned} \tag{7.24}$$

$$H_{xy1}\left(x,x_0\right)=\left(\frac{x_0}{x}-\frac{R^2}{x^2}+1+\frac{x^*}{x}\right),$$

$$H_{xy2}\left(x,x_0\right)=\frac{R^2}{x^2}\left(\frac{\mu_2}{\mu_1\kappa_2}\sum_{k=1}^{+\infty}B_{-k}^L x^{-k}+\frac{1}{\kappa_2}\left[-\frac{1}{x-x^*}+\frac{1}{x}-\frac{x^*\left(x_0-x^*\right)}{x_0\left(x-x^*\right)^2}\right]\right)$$

$$+\left(x-\frac{R^2}{x}\right)\left(\frac{\mu_2}{\mu_1\kappa_2}\sum_{k=1}^{+\infty}\left(-k\right)B_{-k}^L x^{-k-1}+\frac{1}{\kappa_2}\left[\frac{1}{\left(x-x^*\right)^2}-\frac{1}{x^2}+2\frac{x^*\left(x_0-x^*\right)}{x_0\left(x-x^*\right)^3}\right]\right)$$

$$+\frac{R^2}{x^2}\left\{\frac{\mu_2\kappa_1}{\mu_1}\left[\sum_{k=1}^{+\infty}\bar{A}_k^L\left(\frac{R^2}{x}\right)^k-\frac{\mu_1\left(1+\kappa_2\right)}{\mu_2\kappa_1+\mu_1\left(1+b\right)}\frac{1}{x_0}\right]-\frac{\kappa_2 x}{R^2-xx_0}+\frac{x}{R^2}-\frac{\mu_2\left(1+\kappa_1\right)\left(1+b\right)A_0^L}{\mu_2\kappa_1+\mu_1\left(1+b\right)}\right\},$$

(7.25)

where $B_{-k}^R=\mathrm{Re}\left[B_{-k}\right]/b_y^T$, $\bar{A}_k^R=\mathrm{Re}\left[\bar{A}_k\right]/b_y^T$, $A_0^R=\mathrm{Re}\left[A_0\right]/b_y^T$, and $B_{-k}^L=\mathrm{Im}\left[B_{-k}\right]/b_x^T$, $\bar{A}_k^L=\mathrm{Im}\left[\bar{A}_k\right]/b_x^T$, $A_0^L=\mathrm{Im}\left[A_0\right]/b_x^T$.

From the above equations, it is found that the normal stress σ_{yy} is related to the total Burger's vector b_Y^T only, and the shear stress σ_{xy} is related to b_X^T only. Based on the distributed dislocation technique, the singular integral equation of the current Zener-Stroh crack with Cauchy terms are given as:

$$\begin{aligned}\int_{t_1}^{t_2}\frac{B_y\left(x_0\right)}{x-x_0}H_{yy1}\left(x,x_0\right)dx_0+\int_{t_1}^{t_2}B_y\left(x_0\right)H_{yy2}\left(x,x_0\right)dx_0=0,\\ \int_{t_1}^{t_2}\frac{B_x\left(x_0\right)}{x-x_0}H_{xy1}\left(x,x_0\right)dx_0+\int_{t_1}^{t_2}B_x\left(x_0\right)H_{xy2}\left(x,x_0\right)dx_0=0,\end{aligned}\tag{7.26}$$

where the dislocation density components B_x and B_y satisfy the following condition:

$$\int_{t_1}^{t_2}B_y\left(x_0\right)dx_0=b_Y^T,\int_{t_1}^{t_2}B_x\left(x_0\right)dx_0=b_X^T.\tag{7.27}$$

The total sums of Burger Vectors b_Y^T and b_X^T are the factors inducing the Zener-Stroh crack. The singular integral equations (7.26) and (7.27) can be solved numerically [80] by assuming: .

$$B_y(x)=\omega(x)F_y(x),\ B_x(x)=\omega(x)F_x(x), \tag{7.28}$$

where $F_y(x)$ and $F_x(x)$ are non-singular smooth functions in $t_1 \le x \le t_2$, and

$$\omega(x)=\left(x-t_1\right)^{-1/2}\left(t_2-x\right)^{-1/2}, \tag{7.29}$$

is the fundamental function of the integral equation.

By letting

$$\begin{aligned} x&=\frac{t_2-t_1}{2}t+\frac{t_2+t_1}{2},\\ x_0&=\frac{t_2-t_1}{2}s+\frac{t_2+t_1}{2}, \end{aligned} \tag{7.30}$$

the singular integral equations in (7.26) and (7.27) is rewritten as:

$$\begin{aligned} &\sum_{k=1}^{n}\frac{1}{n}F_y\left(s_k\right)\left[\frac{H_{yy1}\left(u_r,s_k\right)}{u_r-s_k}+\frac{t_2-t_1}{2}H_{yy2}\left(u_r,s_k\right)\right]=0,\\ &\sum_{k=1}^{n}\frac{1}{n}F_x\left(s_k\right)\left[\frac{H_{xy1}\left(u_r,s_k\right)}{u_r-s_k}+\frac{t_2-t_1}{2}H_{xy2}\left(u_r,s_k\right)\right]=0, \end{aligned} \tag{7.31}$$

$$\begin{aligned} \sum_{k=1}^{n}\frac{1}{n}F_y\left(s_k\right)&=\frac{2b_Y^T}{\pi\left(t_2-t_1\right)},\\ \sum_{k=1}^{n}\frac{1}{n}F_x\left(s_k\right)&=\frac{2b_X^T}{\pi\left(t_2-t_1\right)}. \end{aligned} \tag{7.32}$$

where

$$\begin{aligned} s_k&=\cos\frac{\pi\left(2k-1\right)}{2n},\ k=1,2,3,...,n,\\ u_r&=\cos\frac{\pi r}{n},\ r=1,2,3,...,n-1. \end{aligned} \tag{7.33}$$

With the numerical solution of the dislocation density function, the Mode I and Mode II stress intensity factors on the left (the blunt) and right (the sharp) crack tips are given by [15]:

$$
\begin{aligned}
K_I^{(t_1)} &= \lim_{\xi\to t_1}\frac{-2\mu_2\sqrt{2\pi}}{\kappa_2+1}\sqrt{\xi-t_1}B_y(x) = -\frac{2\mu_2}{\kappa_2+1}\frac{b_Y^T}{\sqrt{\pi(t_2-t_1)/2}}F_y(-1),\\
K_I^{(t_2)} &= \lim_{\xi\to t_2}\frac{2\mu_2\sqrt{2\pi}}{\kappa_2+1}\sqrt{t_2-\xi}B_y(x) = \frac{2\mu_2}{\kappa_2+1}\frac{b_Y^T}{\sqrt{\pi(t_2-t_1)/2}}F_y(1).
\end{aligned}
\tag{7.34}
$$

$$
\begin{aligned}
K_{II}^{(t_1)} &= \lim_{\xi\to t_1}\frac{-2\mu_2\sqrt{2\pi}}{\kappa_2+1}\sqrt{\xi-t_1}B_x(x) = -\frac{2\mu_2}{\kappa_2+1}\frac{b_X^T}{\sqrt{\pi(t_2-t_1)/2}}F_y(-1),\\
K_{II}^{(t_2)} &= \lim_{\xi\to t_2}\frac{2\mu_2\sqrt{2\pi}}{\kappa_2+1}\sqrt{t_2-\xi}B_x(x) = \frac{2\mu_2}{\kappa_2+1}\frac{b_X^T}{\sqrt{\pi(t_2-t_1)/2}}F_y(1).
\end{aligned}
\tag{7.35}
$$

In the above equations, K_I and K_{II} represent the Mode I and Mode II stress intensity factors, (t_1) and (t_2) represent the left and right crack tips, respectively.

7.2.3. Estimations of the plastic zone size and CTOD by generalized Irwin model

For engineering structures made by composite materials, particularly for metal-matrix composites which can undergo large plastic deformation around the crack tips, plastic zone corrections at the crack tips should be considered in failure analysis. To estimate the plastic zone size (PZS) and CTOD of the current Zener-Stroh crack, the generalized Irwin model for mixed loading problem is employed. Based on the work of Anderson [13], the stress field ahead each crack tip along the crack line can be written as:

$$
\sigma_{xx}^{(t_m)} = \sigma_{yy}^{(t_m)} = \frac{K_I^{(t_m)}}{\sqrt{2\pi r^{(t_m)}}}, \sigma_{xy}^{(t_m)} = \frac{K_{II}^{(t_m)}}{\sqrt{2\pi r^{(t_m)}}}, \sigma_{zz}^{(t_m)} = \frac{2\nu_2 K_I^{(t_m)}}{\sqrt{2\pi r^{(t_m)}}}, \quad m=1,2. \tag{7.36}
$$

To judge if yielding occurs in the plastic zone, the stress components must satisfy Von Mises criterion:

$$\sigma_e^{(t_m)}=\sqrt{\frac{\left(\sigma_{xx}^{(t_m)}-\sigma_{yy}^{(t_m)}\right)^2+\left(\sigma_{xx}^{(t_m)}-\sigma_{zz}^{(t_m)}\right)^2+\left(\sigma_{yy}^{(t_m)}-\sigma_{zz}^{(t_m)}\right)^2+6\left(\sigma_{xy}^{(t_m)2}\right)}{2}}=\sigma_{ys}, \qquad (7.37)$$

where σ_{ys} is the yielding stress of the matrix material. Substituting Eq. (7.36) into (7.37), we have:

$$\sigma_e^{(t_m)}=\frac{K_e^{(t_m)}}{\sqrt{2\pi r^{(t_m)}}}, \qquad (7.38)$$

where $K_e^{(t_m)}=\sqrt{\left(1-2\nu_2\right)^2\left(K_I^{(t_m)}\right)^2+3\left(K_{II}^{(t_m)}\right)^2}$, is a constant related to Mode I and Mode II stress intensity factors at each crack tip. From Eq.(7.38), the first order estimation of plastic zone size can be obtained:

$$r_y^{(t_m)}=\frac{1}{2\pi}\left(\frac{K_e^{(t_m)}}{\sigma_{ys}}\right)^2. \qquad (7.39)$$

Furthermore, the crack tip opening displacement (CTOD) at the sharp tip of the Zener-Stroh crack is given as (the sharp tip is at the right-hand side):

$$\delta^{(t_2)}=\frac{4}{\pi}\frac{K_I^{(t_2)}K_e^{(t_2)}}{E'\,\sigma_{ys}}. \qquad (7.40)$$

$E'=E_2\big/\left(1-\nu_2^2\right)$ for plane strain. In the current work, only the sharp tip (right tip) CTOD is given since the crack propagation always occurs from the sharp tip for a Zener-Stroh crack, as shown in Fig. 7.3.

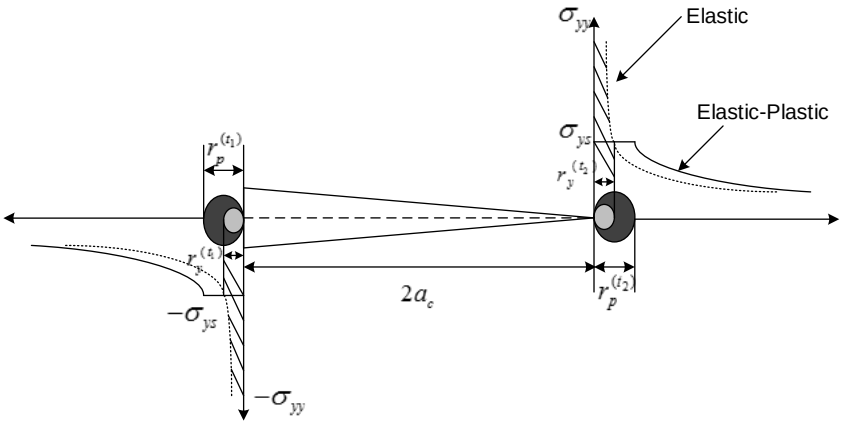

7.3(a)

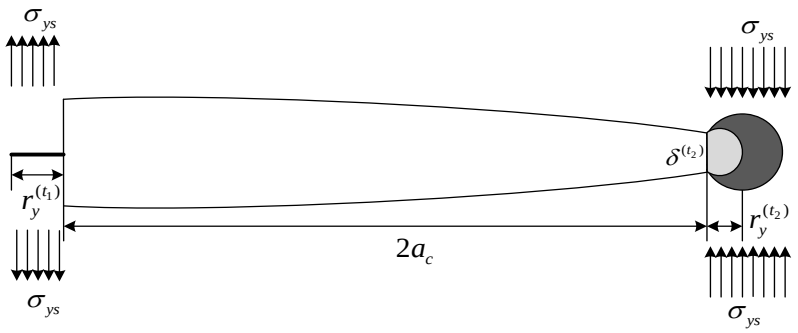

7.3 (b)

Fig. 7.3 (a) Irwin Plastic Zone Model: plastic zones of sizes r_y and r_p ahead of a crack tip; (b) The crack tip opening displacement δ and the corresponding loading conditions.

7.3. Numerical examples and discussions

In the above process, the stress field ahead the crack tips, the stress intensity factor (SIF), plastic zone size (PZS), and CTOD have been analyzed. The influence of material mismatch and interface effect on the SIF, PZS and CTOD are going to be examined. The above quantities are normalized by the corresponding SIF, PZS and CTOD when the crack is located in a homogeneous material as follows:

$$K_0^I = \frac{2\mu_2}{1+\kappa_2}\frac{b_y^T}{\sqrt{\pi a_c}},\ K_0^{II} = \frac{2\mu_2}{1+\kappa_2}\frac{b_x^T}{\sqrt{\pi a_c}},$$
$$\rho_0 = \frac{1}{2\pi}\left(\frac{K_e}{\sigma_{ys}}\right)^2,\ \delta_0 = \frac{4}{\pi}\frac{K_0^I K_e}{E'\sigma_{ys}}, \tag{7.41}$$

where a_c is the half crack length, $K_e = \sqrt{(1-2\nu_2)^2\left(K_0^I\right)^2 + 3\left(K_0^{II}\right)^2}$. Noting that the Zener-Stroh crack always propagate from the sharp tip, only the results of the sharp tip are given in the present work. The interface Lame constants μ^0 and λ^0 are associated to the inhomogeneity by constants α and β, where $\alpha = \mu^0/\mu_1$, $\beta = \lambda^0/\mu_1$, respectively. One difficult point to consider interface effect is that no exact values of μ^0 and λ^0 can be found in open literature, Fang and Liu [125] pointed out that the absolute values of intrinsic lengths α and β are around 0.1 based on the work of Miller and Shenoy [126], who computed the free surface properties for aluminum and silicon by the embedded atom method. These results are used here. In our numerical examples, the values of α and β are taken around 0.1. To investigate the influence of the Zener-Stroh crack sharp tip position on the fracture behavior, two cases are studied in the following section:

Case I: The sharp crack tip is at the right-hand side of the crack, away from the inclusion;

Case II: The sharp crack tip is at the left-hand side of the crack, close to the inclusion.

7.3.1. The effect of inhomogeneity size on the SIF, PZS and CTOD.

In nano scale, the size of the inclusion (inhomogeneity) has great effect on

the stress field of the edge dislocations. Evidence from both experiment [127] and theory [128] exists. It indicates that the deformation behavior of an elastic element with nanoscale characteristic dimension is essentially size-dependent. The variation of the normalized Mode I and Mode II stress intensity factors, normalized PZS and normalized CTOD are depicted in Figs. 7.4 and 7.5, separately. Two sets of interface moduli are used here based on the work of Fang and Liu [125]. Namely, the intrinsic lengths are $\alpha = -0.17915, \beta = 0.1005$ and $\alpha = -0.0108, \beta = 0.197132$. The left crack tip is at the position of $t_1 = 1.15R$ and the right crack tip at $t_2 = 1.25R$. The shear modulus ratio between the inhomogeneity and the matrix is set as $\mu_2 / \mu_1 = 0.9$.

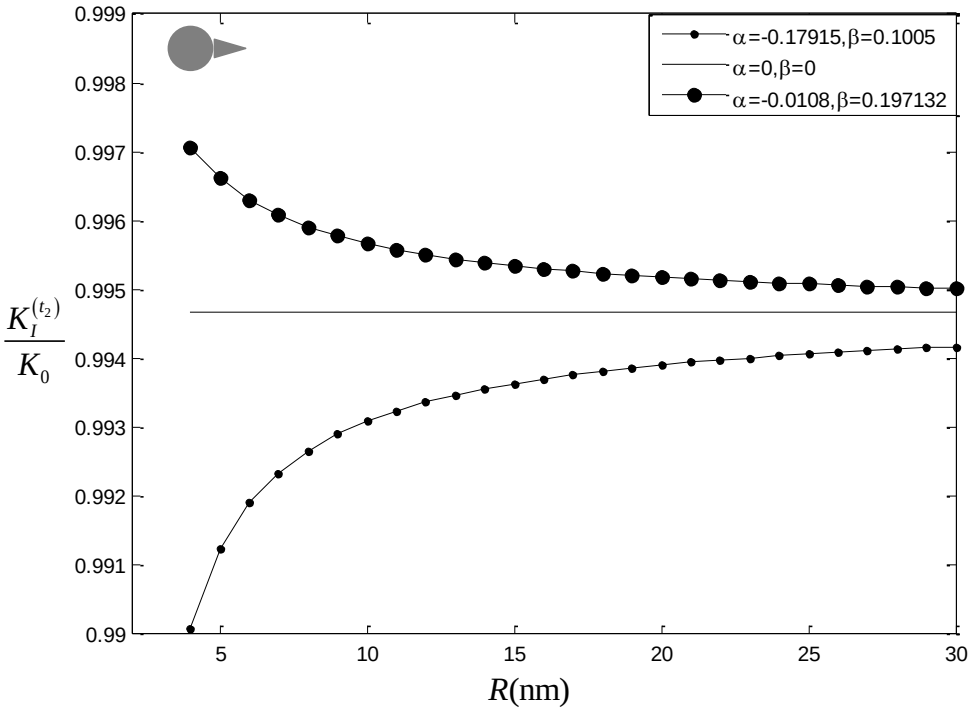

7.4(a)

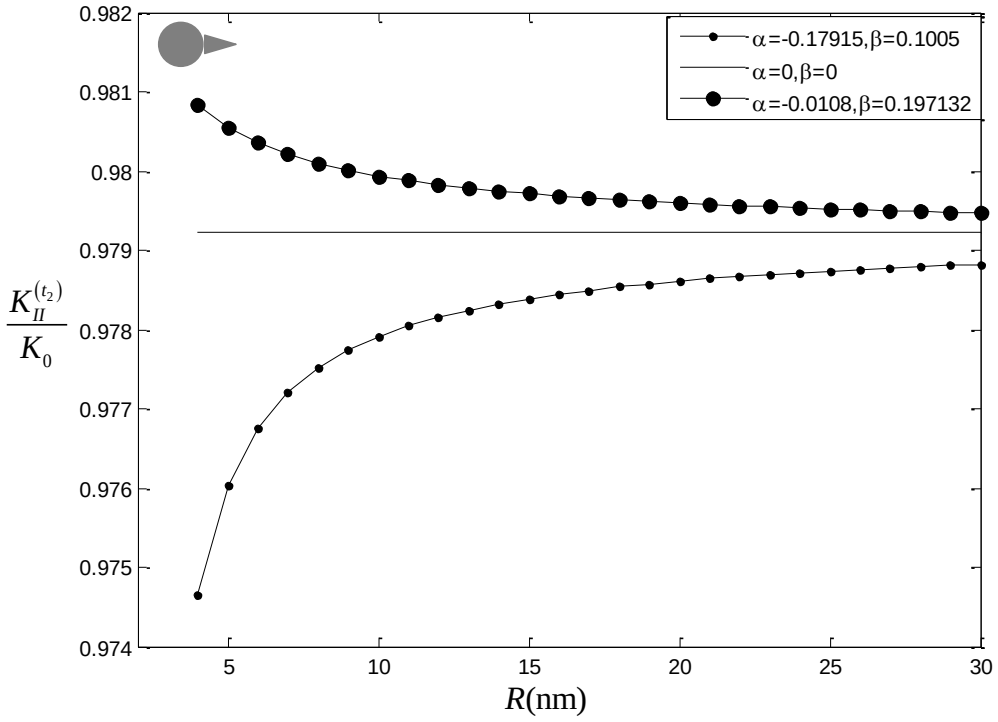
α=-0.17915,β=0.1005
α=0,β=0
α=-0.0108,β=0.197132
$\frac{K_{II}^{(t_2)}}{K_0}$
0.982
0.981
0.98
0.979
0.978
0.977
0.976
0.975
0.974
5
10
15
20
25
30
R(nm)

7.4(b)

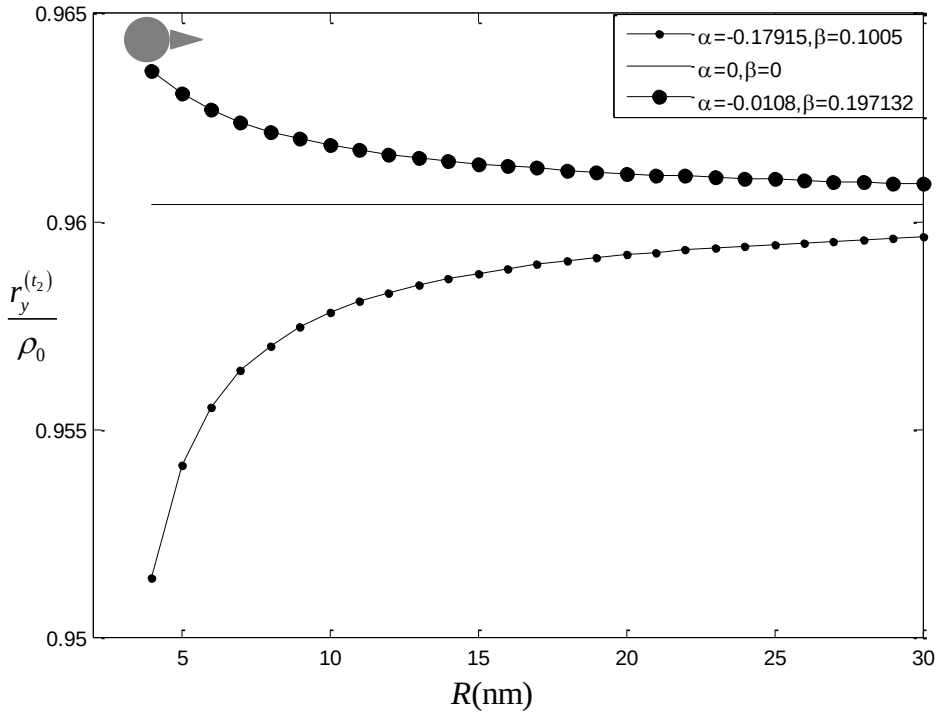
α=-0.17915,β=0.1005
α=0,β=0
α=-0.0108,β=0.197132
$\frac{r_y^{(t_2)}}{\rho_0}$
0.965
0.96
0.955
0.95
5
10
15
20
25
30
R(nm)

7.4(c)

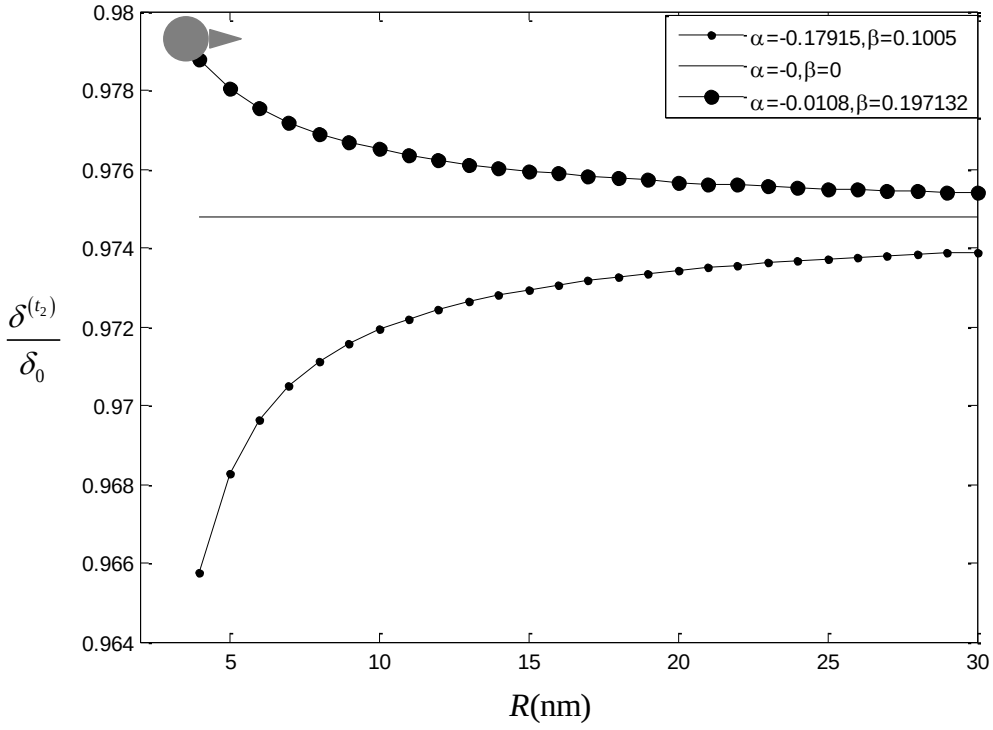

7.4(d)

Fig. 7.4 The effect of inhomogeneity size on the SIF, PZS and CTOD with $\nu_1 = \nu_2 = 0.3$, $t_1 = 1.15R$, $t_2 = 1.25R$, $b_X^T / b_Y^T = 1$ and $\mu_2 / \mu_1 = 0.9$ when the sharp tip is on the right. (a). The normalized Mode I stress intensity factor at the sharp tip; (b) The normalized Mode II stress intensity factor at the sharp tip; (c) The normalized PZS at the sharp tip; (d) The normalized CTOD at the sharp tip.

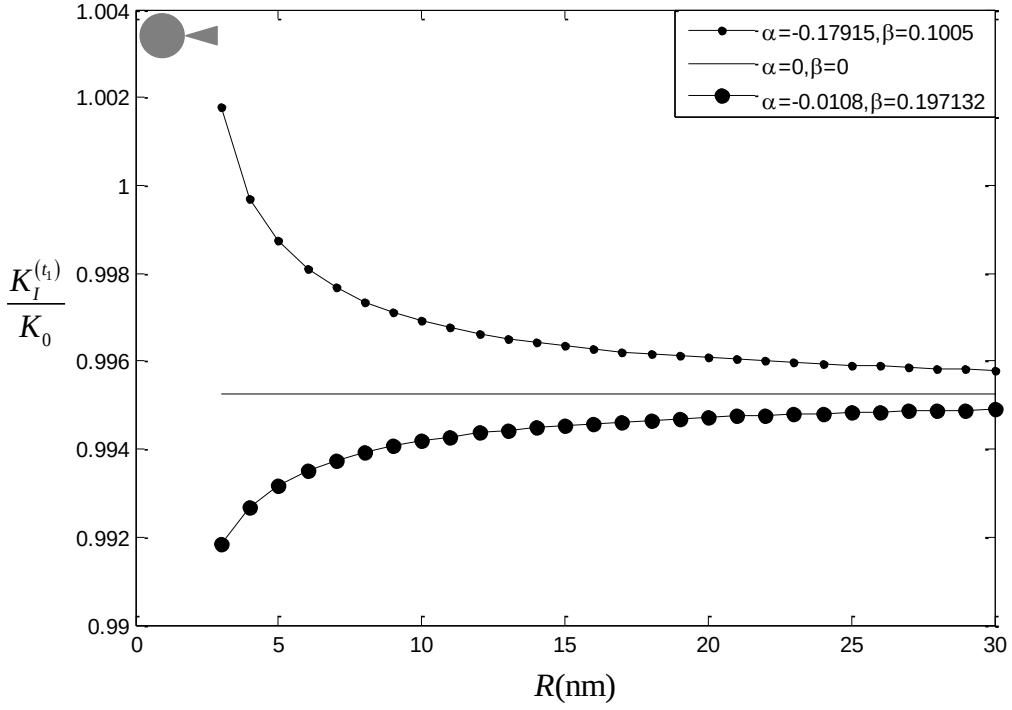
α=-0.17915,β=0.1005
α=0,β=0
α=-0.0108,β=0.197132
$\frac{K_I^{(t_1)}}{K_0}$
1.004
1.002
1
0.998
0.996
0.994
0.992
0.99
0
5
10
15
20
25
30
R(nm)

7.5(a)

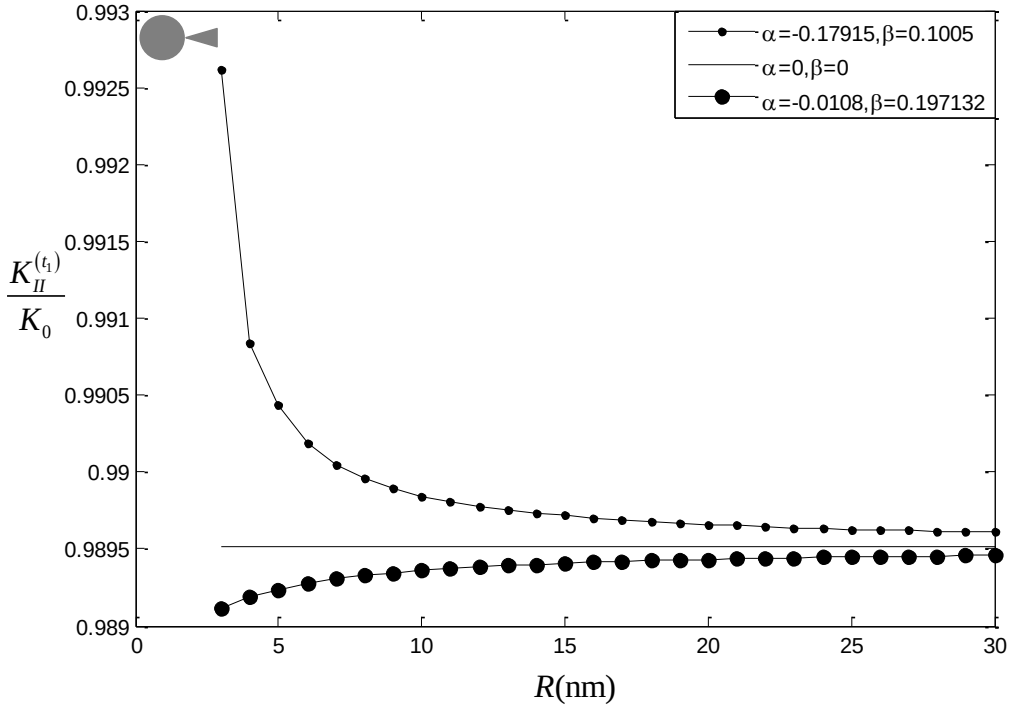
α=-0.17915,β=0.1005
α=0,β=0
α=-0.0108,β=0.197132
$\frac{K_{II}^{(t_1)}}{K_0}$
0.993
0.9925
0.992
0.9915
0.991
0.9905
0.99
0.9895
0.989
0
5
10
15
20
25
30
R(nm)

7.5(b)

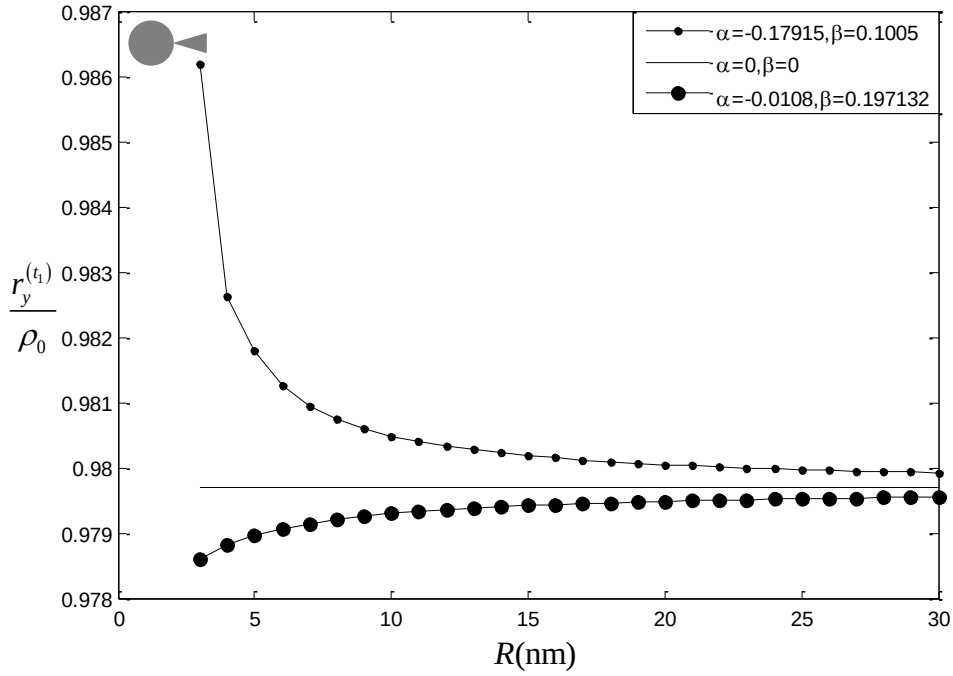

7.5(c)

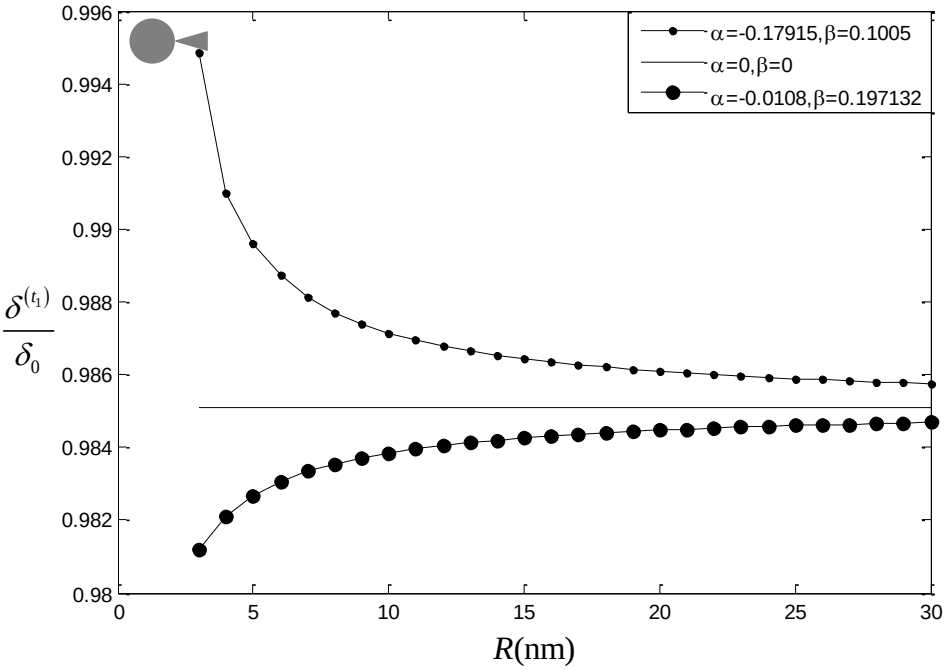

7.5(d)

Fig. 7.5 The effect of inhomogeneity size on the SIF, PZS and CTOD with $\nu_1 = \nu_2 = 0.3$, $t_1 = 1.15R$, $t_2 = 1.25R$, $b_X^T / b_Y^T = 1$ and $\mu_2 / \mu_1 = 0.9$, when the sharp tip is on the left. (a). The normalized Mode I stress intensity factor at the sharp tip; (b) The normalized Mode II stress intensity factor at the sharp tip; (c) The normalized PZS at the sharp tip; (d) The normalized CTOD at the sharp tip.

From the figures, it is clear that when the inclusion radius R is smaller than 20, the influence of inclusion radius is really significant on the normalized SIFs, PZS and CTOD for both cases of sharp crack tip position. For different combinations of intrinsic length, the responses of the values to the increasing inclusion radius are also different. From the figures, if $\alpha = \beta = 0,$ which means the interface effect is ignored, increasing the inhomogeneity size does not have great influence on the crack behavior. However, if $\alpha = -0.17915, \beta = 0.1005,$ the normalized SIFs, PZS and CTOD increase with the increasing inclusion radius for case I, and decrease with the increasing inclusion radius for case II. When $\alpha = -0.0108, \beta = 0.197132,$ the normalized SIFs, PZS and CTOD decrease with the increasing R for case I, and increase for case II, respectively.

7.3.2. The effect of crack-inhomogeneity distance on the SIF, PZS and CTOD.

To examine the influence of the crack-inhomogeneity distance on the crack elastic-plastic behavior, the crack length is taken as $a_c = 0.1R$, $R = 20$. Other parameters are set as: $b_X^T / b_Y^T = 1,\ v_1 = v_2 = 0.3.$ The curves of normalized SIFs, PZS and CTOD at the sharp tip are plotted in Figs. 7.6 and 7.7, respectively. Comparisons have been made between two combinations of intrinsic parameters, $\alpha = \beta = 0.1$ and $\alpha = \beta = 0$ to indicate the difference between nanoscale problem with interface effects and the classical case without interface effects.

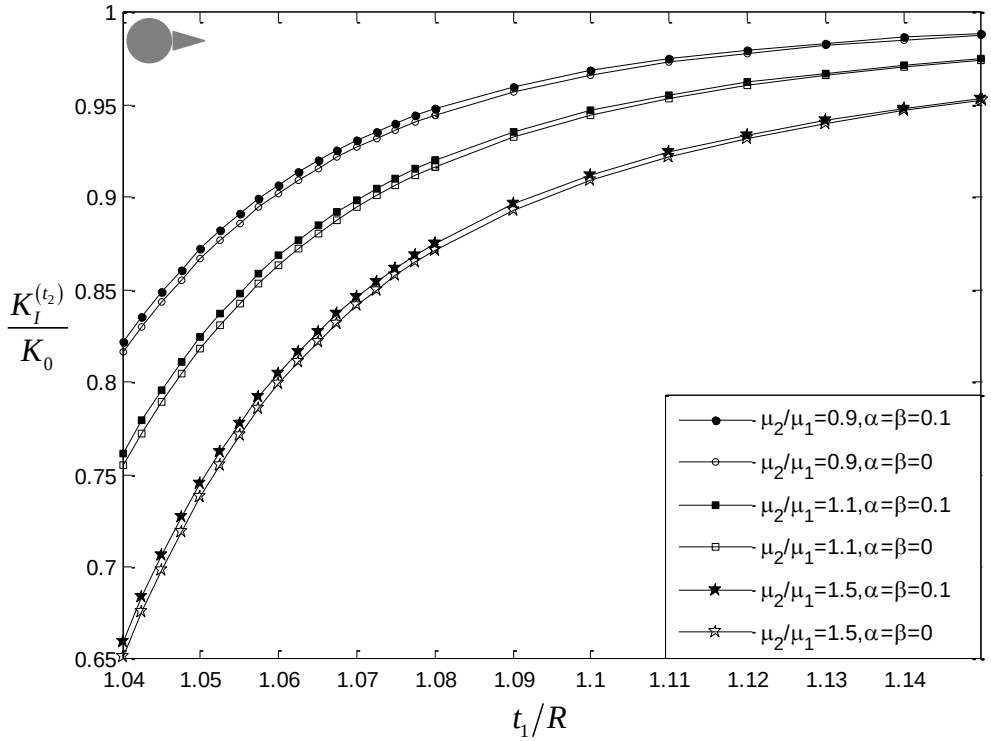
$\frac{K_I^{(t_2)}}{K_0}$
t_1/R
μ2/μ1=0.9,α=β=0.1
μ2/μ1=0.9,α=β=0
μ2/μ1=1.1,α=β=0.1
μ2/μ1=1.1,α=β=0
μ2/μ1=1.5,α=β=0.1
μ2/μ1=1.5,α=β=0

7.6(a)

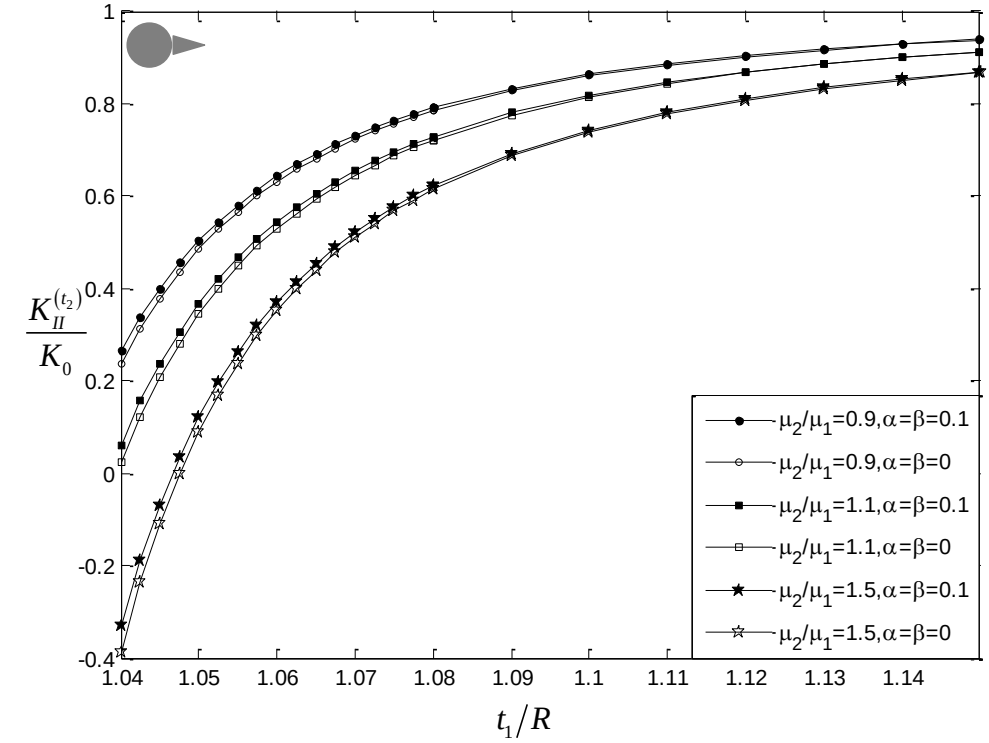
$\frac{K_{II}^{(t_2)}}{K_0}$
t_1/R
μ2/μ1=0.9,α=β=0.1
μ2/μ1=0.9,α=β=0
μ2/μ1=1.1,α=β=0.1
μ2/μ1=1.1,α=β=0
μ2/μ1=1.5,α=β=0.1
μ2/μ1=1.5,α=β=0

7.6(b)

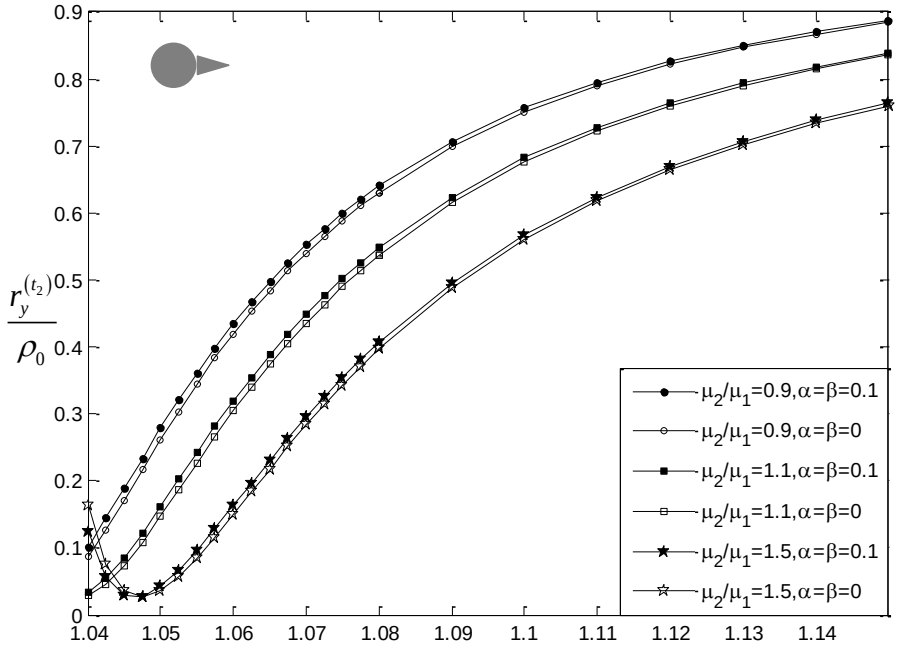

7.6(c)

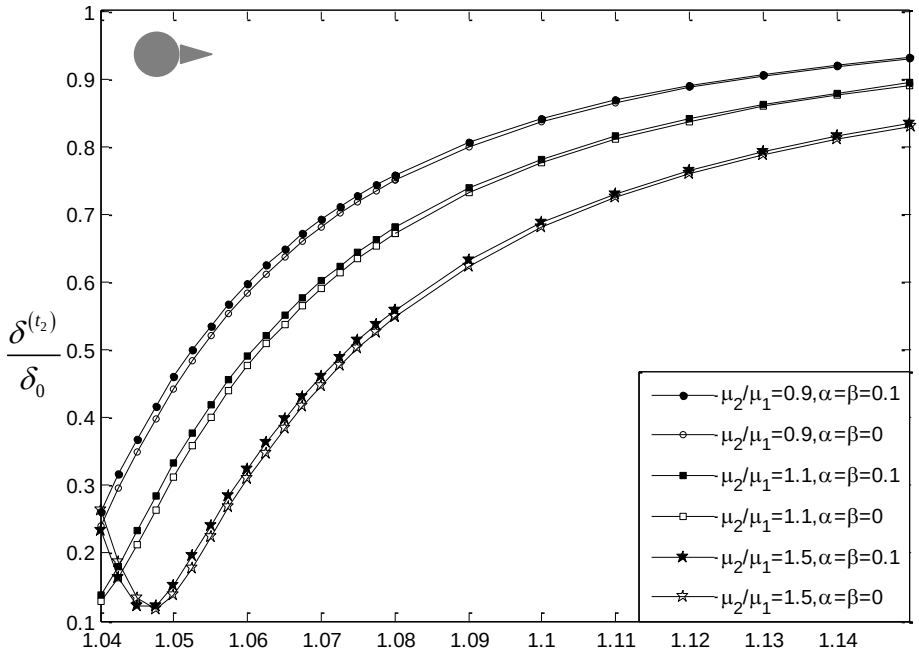

7.6(d)

Fig. 7.6 The effect of crack-inhomogeneity distance on the SIF, PZS and CTOD with $\nu_1 = \nu_2 = 0.3$, $R = 20$, $a_c = 0.1R$ and $b_X^T / b_Y^T = 1$, when the sharp tips on the right. (a). The normalized Mode I stress intensity factor at the sharp tip; (b) The normalized Mode II stress intensity factor at the sharp tip; (c) The normalized PZS at the sharp tip; (d) The normalized CTOD at the sharp tip.

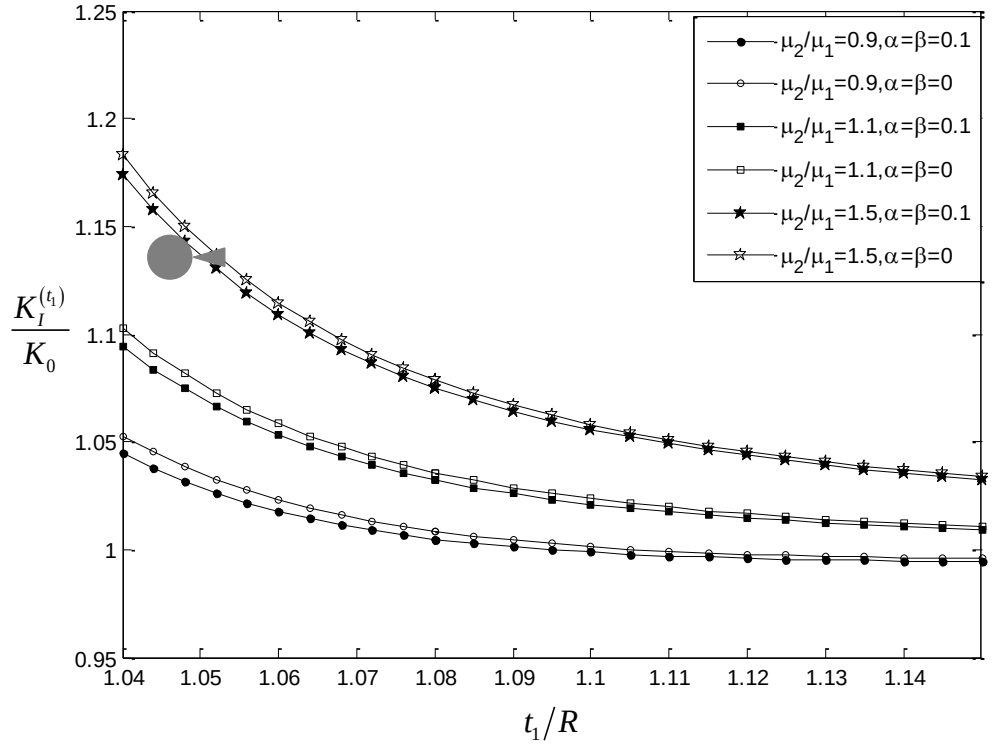
μ2/μ1=0.9,α=β=0.1
μ2/μ1=0.9,α=β=0
μ2/μ1=1.1,α=β=0.1
μ2/μ1=1.1,α=β=0
μ2/μ1=1.5,α=β=0.1
μ2/μ1=1.5,α=β=0
$\frac{K_I^{(t_1)}}{K_0}$
t_1/R

7.7(a)

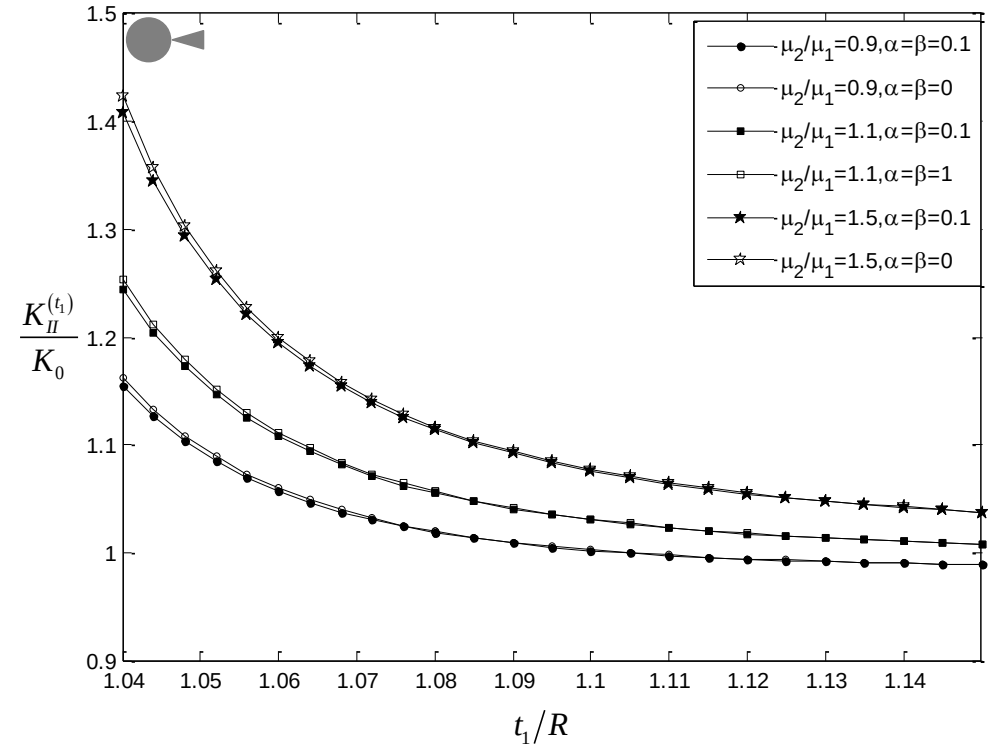
μ2/μ1=0.9,α=β=0.1
μ2/μ1=0.9,α=β=0
μ2/μ1=1.1,α=β=0.1
μ2/μ1=1.1,α=β=1
μ2/μ1=1.5,α=β=0.1
μ2/μ1=1.5,α=β=0
$\frac{K_{II}^{(t_1)}}{K_0}$
t_1/R

7.7(b)

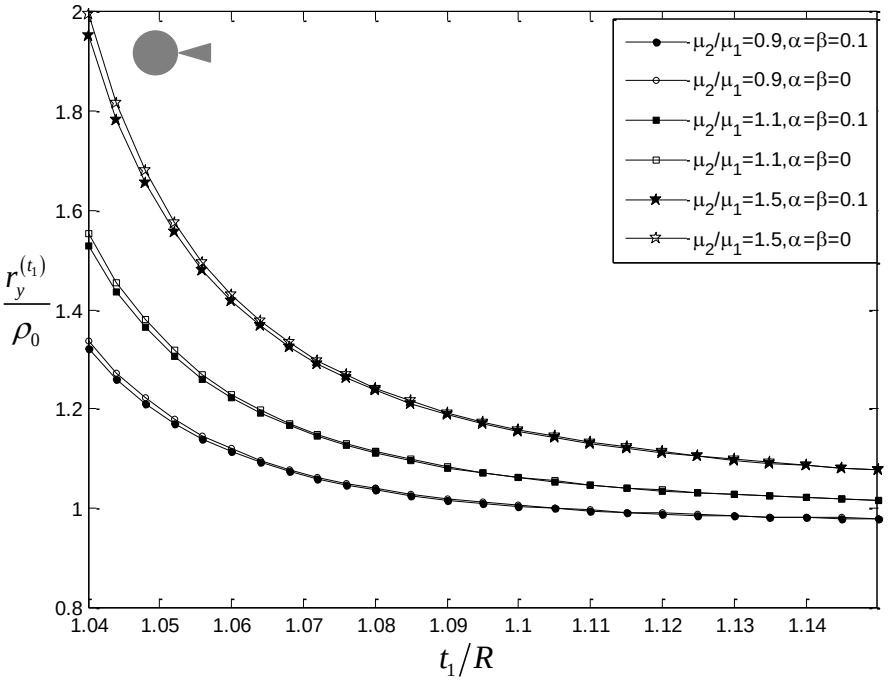

7.7(c)

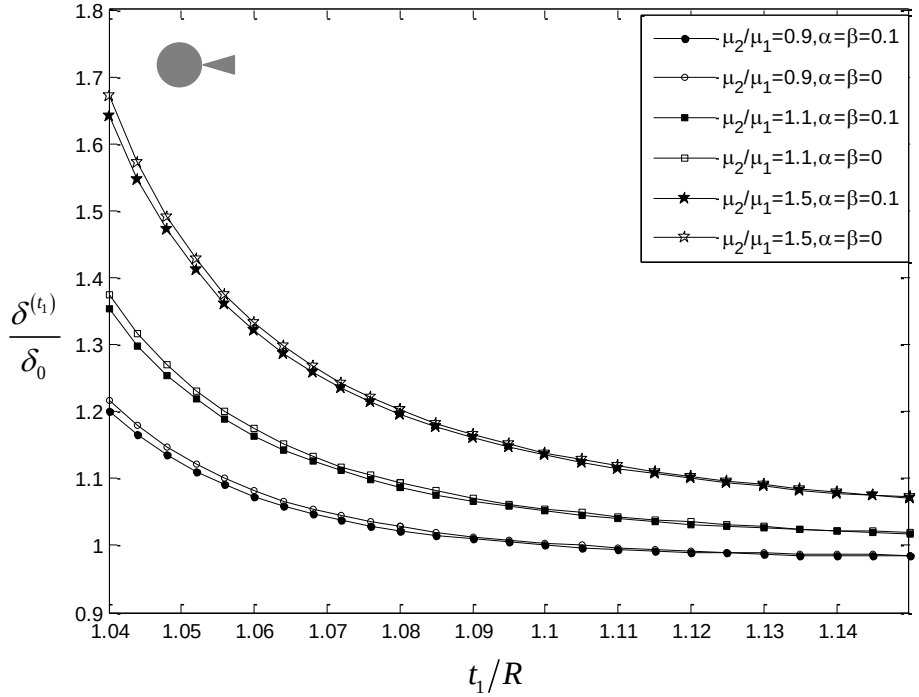

7.7(d)

Fig. 7.7 The effect of crack-inhomogeneity distance on the SIF, PZS and CTOD with $\nu_1 = \nu_2 = 0.3$, $R = 20$, $a_c = 0.1R$ and $b_X^T / b_Y^T = 1$, when the sharp tip is on the left. (a). The normalized Mode I stress intensity factor at the sharp tip; (b) The normalized Mode II stress intensity factor at the sharp tip; (c) The normalized PZS at the sharp tip; (d) The normalized CTOD at the sharp tip.

For case I, with the increasing inhomogeneity-crack distance t_1/R, the

normalized SIFs increase accordingly while the normalized PZS and CTOD decrease first and then increase for some shear modulus ratio. When the distance t_1/R is larger than 1.2, all the normalized values are close to 1, and the problem can be reduced to a classical problem without the influence of interface effect and inhomogeneity size. The effect of the shear modulus ratio μ_2/μ_1 is also depicted here. From 0.9 to 1.5, we can see that when the shear modulus ratio (matrix/inhomogeneity) increases, the normalized SIFs, PZS and CTOD decrease accordingly. It means for the current nanoscale crack-inhomogeneity interaction problem, a "stiffer" matrix is better in avoiding structure failure and crack propagation. In addition, by considering the interface effect with $\alpha = \beta = 0.1$, the normalized SIFs, PZS and CTOD are slightly larger than the case $\alpha = \beta = 0.$ The responses of normalized SIFs, PZS and CTOD to the increasing crack-inhomogeneity distance in Case II will be different comparing against Case I, which can be found from Figs. 7.7 (a) to (d), respectively.

7.3.3. The effect of dislocation loading on the normalized PZS and CTOD

As mentioned before, the cracks in composites are usually in the form of Zener-Stroh crack at the early stage. In this chapter, it is assumed that the crack is induced by pure dislocation loading b_X^T and b_Y^T. As a mixed mode loading problem, it is worth to understand the influence of each loading on the plastic zone size and CTOD. From Eqs. (7.34) and (7.35), we know that the Mode I and Mode II stress intensity factors are independent to each other. But to judge if

yielding occurs within the plastic zone, both the normal and shear traction component contribute to the plastic zone size, as given in Eq. (7.37). To study the influence of each loading, the parameters are set as $\nu_1 = \nu_2 = 0.3$, $a_c = 0.1R$, $\mu_2/\mu_1 = 0.9$, $\alpha = \beta = 0.1$. From Figs. 7.8(a) to (d), we can see when the ratio b_X^T/b_Y^T is zero, the case I/case II normalized PZS and CTOD are significantly larger/smaller than the corresponding values for $b_X^T/b_Y^T = 0.5, 1, 2, 5$. Increasing the dislocation loading b_X^T, the normalized PZS and CTOD decrease/increase for the right/left sharp crack tip, respectively.

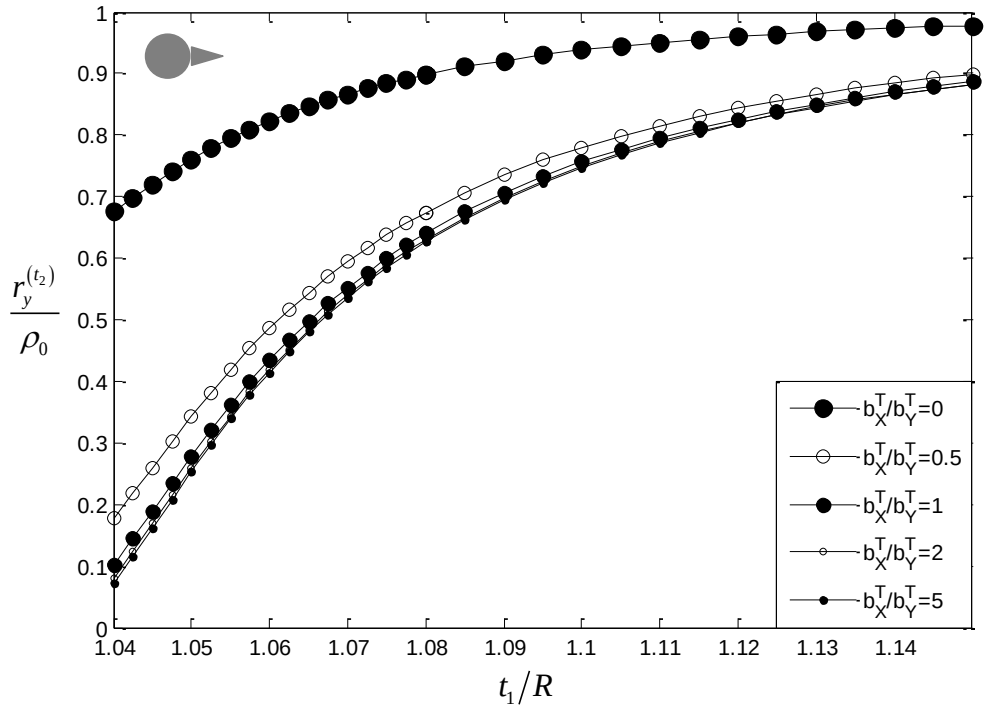

7.8(a)

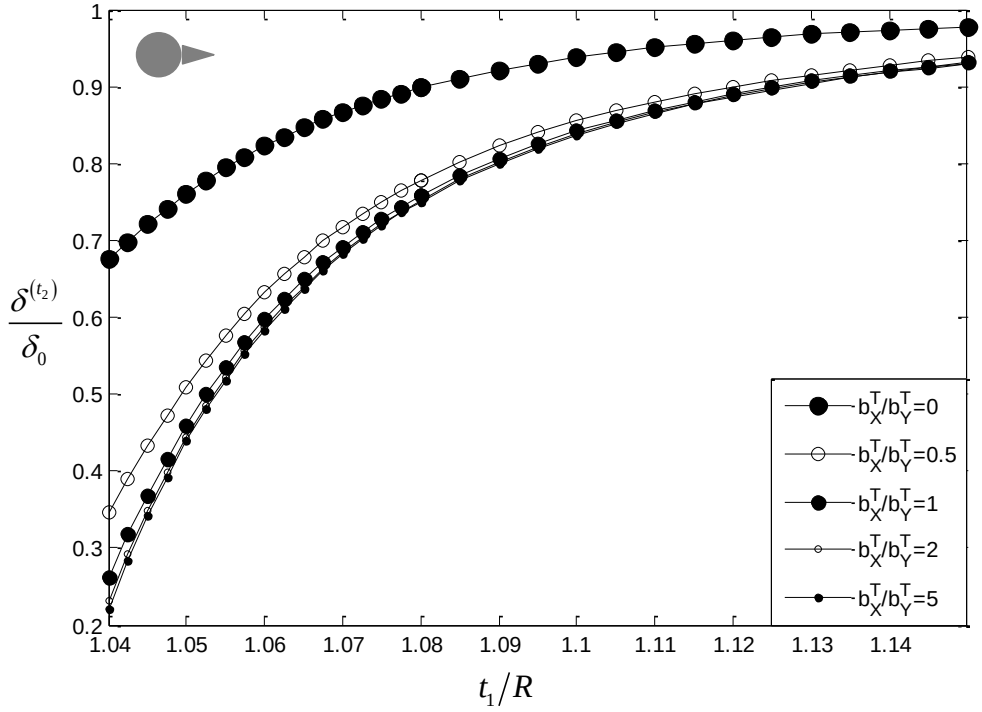
$\frac{\delta^{(t_2)}}{\delta_0}$
t_1/R
b_X^T/b_Y^T=0
b_X^T/b_Y^T=0.5
b_X^T/b_Y^T=1
b_X^T/b_Y^T=2
b_X^T/b_Y^T=5

7.8(b)

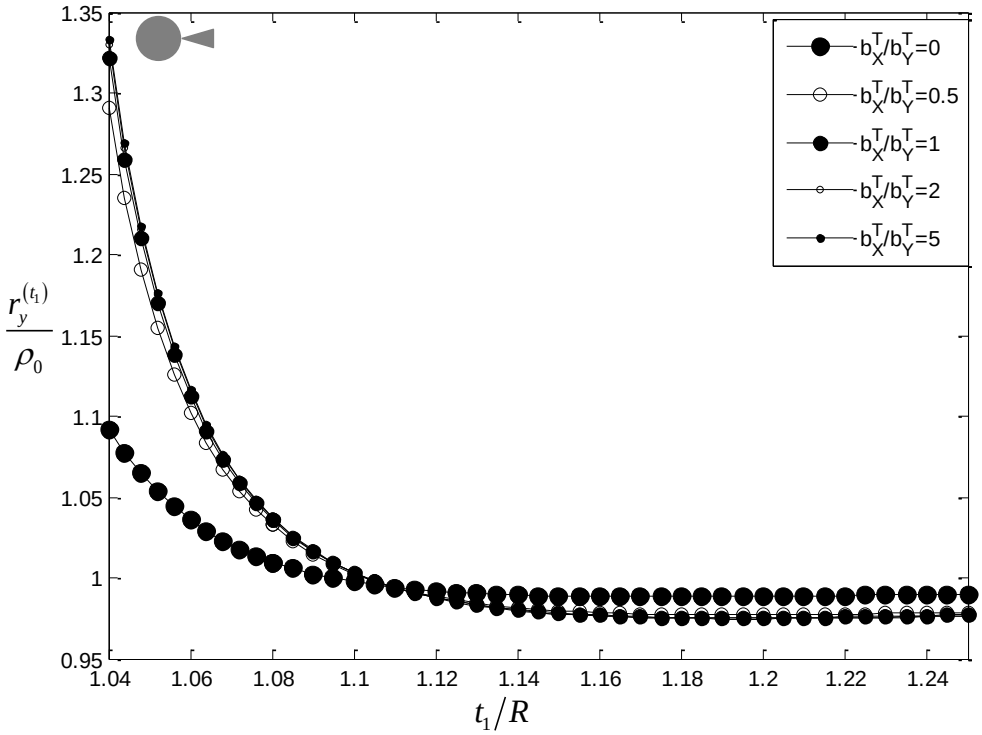
$\frac{r_y^{(t_1)}}{\rho_0}$
t_1/R
b_X^T/b_Y^T=0
b_X^T/b_Y^T=0.5
b_X^T/b_Y^T=1
b_X^T/b_Y^T=2
b_X^T/b_Y^T=5

7.8(c)

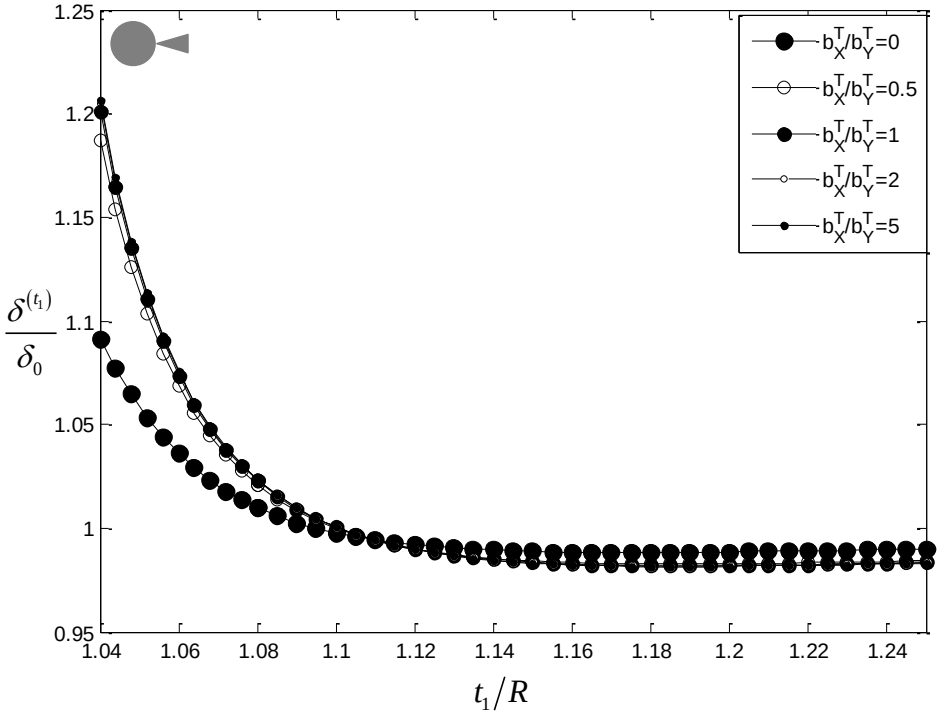

7.8(d)

Fig. 7.8 The effect of dislocation loading b_X^T/b_Y^T on the PZS and CTOD with $\nu_1=\nu_2=0.3$, $a_c=0.1R$, $R=20$, $\mu_2/\mu_1=0.9$, $\alpha=\beta=0.1$. (a) The normalized PZS at the right sharp tip; (b) The normalized CTOD at the right sharp tip; (c) The normalized PZS at the left sharp tip; (d) The normalized CTOD at the left sharp tip.

7.4. Conclusions

In nano composites, the inclusion (inhomogeneity) size and inclusion/matrix interface have significant influence on the fracture behavior of the composites, especially when a crack is initiated close to the nano inhomogeneity. Through the current study, it is found that for different intrinsic lengths, the normalized SIF, PZS and CTOD are quite different. When the crack is closer to the inhomogeneity (the inclusion), the influence of the inclusion/matrix interface becomes more significant. If the crack is far away from the inclusion, the normalized SIFs, PZS and CTOD trend to be 1, the problem is reduced to a classical homogenous crack case.

Chapter 8 Conclusions, Limitations and Future Work

8.1. Introduction

In the current PhD study, the problems of an arc-shaped interface crack along a circular inclusion and a matrix, the interaction between a Griffith/Zener-Stroh crack and a coated inclusion, the interaction between a Griffith crack and its nearby inclusions in a three-phase composite model, as well as a Zener-Stroh crack interacting with a nano-sized inclusion have been investigated. In this chapter, a brief summary is given for the PhD research work by emphasizing some important findings and conclusions of each physical problem solved. The limitation of the current work is analyzed. Some potential ways in which the fracture mechanics analysis can be improved in the future work are discussed.

8.2. Conclusions

To conduct plastic zone correction analysis for the interface crack due to debonding and matrix crack problems in fiber-reinforced composites, two approaches were employed in the work. The mixed-mode Dugdale model was introduced to deal with the interface crack problem while the generalized Irwin model was applied to solving the crack-inclusion (coated inclusion and multiple-inclusion) problems. The cracks were simulated by distributed dislocation method. The formulated singular integral equations are solved numerically in

order to obtain the plastic zone size (PZS) and crack tip opening displacement (CTOD). Throughout the study, we found that:

1. For the curved (arc-shaped) interface crack, the half debonding angle has great influence on the normalized SIF, PZS and CTOD, so as the inclusion/matrix shear modulus ratio. When the ratio is smaller than 1, or the inclusion is "softer" than or close to the matrix, the influence of the inclusion/matrix shear modulus ratio on the SIF, PZS and CTOD is significant. When the ratio approaches to infinity (the inclusion is rigid), the SIF, PZS and CTOD tend to be stabilized. Under uniaxial tension, the maximum half debonding angle cannot exceed 77°, which means the inclusion can only be partially debonded from the matrix under pure tensile loading. Further study shows that if the remote loading is hydrostatic tension, the inclusion could be completely debonded.
2. For the problem of a radial Griffith crack interacting with a coated circular inclusion, it is found that the orientation angle has great effect on the normalized PZS and CTOD, while the influence of coating phase thickness and crack-inclusion distance is more significant than the shear modulus ratio (the coating phase/the matrix). For the problem of a Zener-Stroh crack interacting with a coated inclusion, since it has been assumed that the crack is induced by dislocation pile-up only, the influence of orientation angle is not considered. But it has been found that the influence of coating phase thickness and crack-inclusion distance highly depend on the shear modulus

ratio of the inclusion/coating and coating/matrix. For a Zener-Stroh crack, the sharp crack tip position also has great effect on the elastic-plastic fracture behavior of the crack.

3. To simulate the interaction among a crack and its surrounding inclusions in a composite, the three-phase cylindrical model is introduced by assuming that the crack and the nearest inclusion are embedded in their immediate surrounding pure matrix, while the other inclusions and matrix parts are replaced by an equivalent homogeneous media (the composite material). For a radial Griffith crack in the three-phase model, it is found that the orientation angle has great effect on the plastic zone size and CTOD. As for the fiber concentration and shear modulus ratio inclusion/matrix, for a "softer" inclusion, the effect of the inclusions on the crack tips is anti-shielding, which means decrease the shear modulus ratio, the normalized PZS and normalized CTOD will increase. In the meantime, a lager fiber concentration will induce to larger normalized values of CTOD. On the other hand, for a "harder" inclusion, increase either the shear modulus ratio (inclusion/matrix) or the fiber concentration, both the plastic zone size and CTOD will decrease. In other words, "harder" inclusions shield the crack from propagation.
4. When a micro crack due to dislocation pileup near a nano-sized inhomogeneity (inclusion) at the very early stage, a good way to model the crack behavior is using Zener-Stroh mechanism. In the nano size level, it is found that the size and interface effects of the inclusion on the fracture

behavior become quite significant and cannot be ignored, especially when the crack is close to the nano inhomogeneity. Two new parameters named intrinsic lengths denoted by α and β are used to represent the interface effect of the inclusion during the study. For different combination of α and β, the stress intensity factor, plastic zone size and crack tip opening displacement change drastically, which shows the complexity of fracture behaviors in nano-sized structures.

8.3. Limitations of the current study

In the current research, we focus on introducing a new physical mechanism (the plastic zone correction) to analyze the fracture behaviors of various crack problems in fiber-reinforced composite materials. Some theoretical and technical limitations exist. One difficulty is the gap between traditional linear elastic fracture mechanics (LEFM) and elastic-plastic fracture mechanics (EPFM). In our work, the plastic zone size (PZS) and the crack tip opening displacement (CTOD) are used to characterize the crack tip condition instead of the traditional stress intensity factor (SIF). However, the definition and derivative of PZS and CTOD are still within the LEFM profile by assuming a small plastic zone area ahead the crack tips. Both Dugdale model and Irwin model used in the current work stand upon the LEFM assumptions and only small scale yielding is allowed throughout the analysis.

The technical limitation occurs during the process of solving the governing

equations. Throughout our study, to conduct the plastic zone correction for the crack in composite materials, the mixed-mode Dugdale model and generalized Irwin model are proposed. In the Dugdale model, the plastic zone is treated as a short line segment ahead of the crack (ρ in Fig. 2.6). The solution is obtained by fulfilling the condition that stress intensity factors due to the applied load K_I cancel out those due to the closure stresses K_ρ :

$$K_I + K_\rho = 0. \tag{8.1}$$

The closure stresses in the plastic zone satisfy the Von Mises yield criterion having the form:

$$\sqrt{\sigma_{yy}^2 + 3\tau_{xy}^2} = \sigma_{ys}, \tag{8.2}$$

where, σ_{yy} is the normal stress, τ_{xy} is the shear stress and σ_{ys} is the yield stress of the material. On one hand, the PZS and CTOD can be obtained by solving the above equations through iteration method, which has a very strict requirement of the calculation technique. On the other hand, as we have chosen Gauss-Chebyshev quadrature technique to impose substantial quantities of collocation points to numerically solve the singular integral equations, the density of collocation points plays a very important role in the calculation accuracy. For multiphase composite, the matrix involved in the process is quite complicated which requires a high density of collocation point and thus makes it difficult to solve the singular integral equations efficiently under the current hardware techniques.

Despite these limitations, the mixed mode Dugdale model and generalized

Irwin model do provide important insights in crack-tip plasticity for various crack problems in fiber-reinforced composites. By applying the Von mises yielding criterion, the stress field inside the yielding zone can be evaluated, thus the plastic zone size and crack tip opening displacement can be obtained numerically. The CTOD solution can be used as an advanced fracture criterion compared with the stress intensity factor criterion. The most important of all, comparing with other existing elastic-plastic fracture analyzing techniques, our methodology is easier to be adopted and more computationally effective, thus more practical for engineering applications.

8.4. Future work

There are two approaches used in the current research to deal with the plastic zone corrections for crack problems in fiber-reinforced composites: the mixed-mode Dugdale model and the generalized Irwin model. In both models, the Von Mises yielding criterion is used to judge if yielding occurs in the plastic zone area.

In the future work, the cohesive zone model [129-133] can be used in deciding the plastic zone size. To the knowledge of the author, in a cohesive zone model, a narrow-band of vanishing thickness termed the cohesive zone is assumed to exist ahead of a crack tip to represent the fracture process zone (shown in Fig. 8.1). The upper and lower surfaces of the narrow-band are termed as the cohesive surfaces which are acted by the so-called cohesive traction. The

cohesive traction follows a cohesive constitutive law that relates the cohesive traction to the separation displacement of the cohesive surfaces. Crack growth occurs when the separation at the tail of the cohesive zone (the physical crack tip) reaches a critical value at which the cohesive traction vanishes.

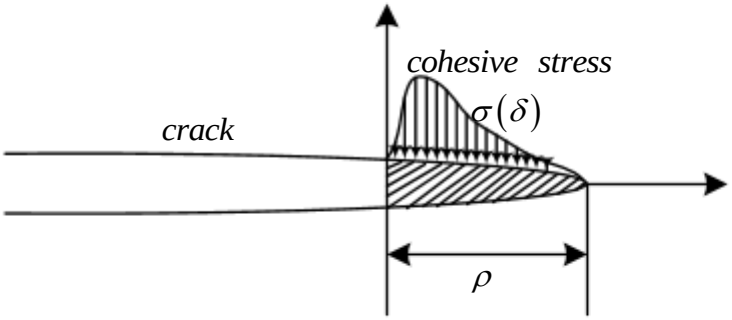

Fig. 8.1 A cohesive zone ahead of a crack

One of the most important advantages of the cohesive zone model is that it can take different constitutive laws to simulate different material behaviors, specifically as shown in Fig. 8.2 [134].

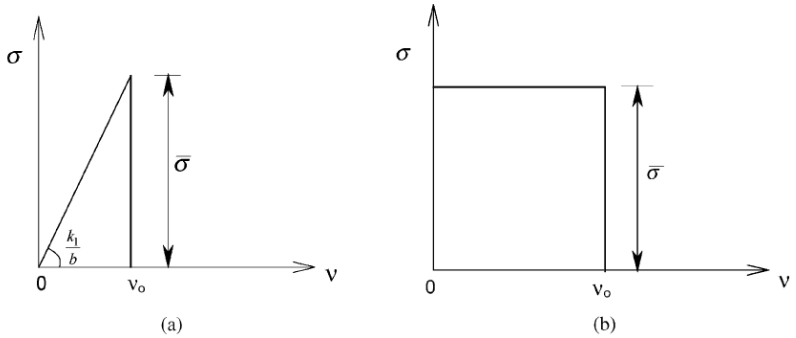

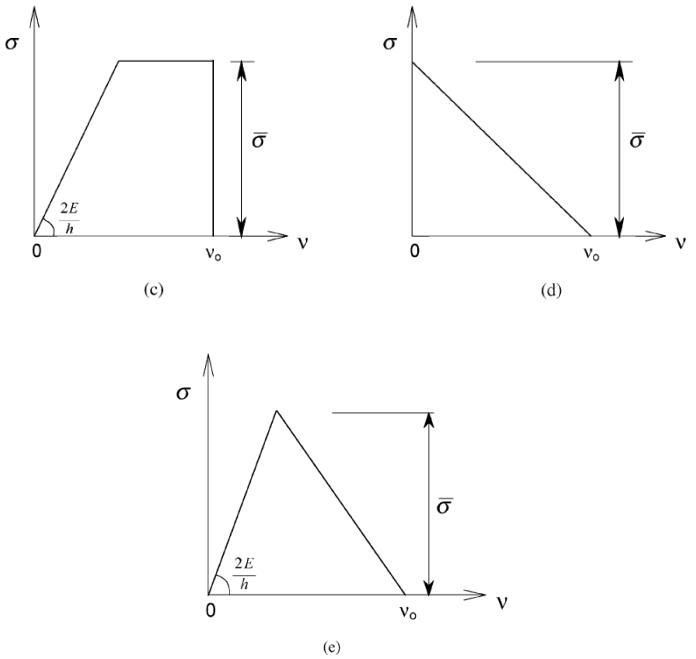

Fig. 8.2 Forms of cohesive zone traction laws; (a) Triangular form. (b) Constant stress form. (c) Elastic-constant stress form. (d) Linear damage form. (e) Elastic-linear damage form.

It is seen from Fig. 8.2 that the current used Dugdale model is a typical case of cohesive model by assuming the cohesive traction to be constant in the whole zone (Fig. 8.2(b)). The cohesive zone approach does not involve crack tip stress singularities of classical fracture mechanics. The material failure is controlled by quantities such as displacements and stresses, which are consistent with the strength of materials theory. In future work, we can explore the best cohesive law for each specific material so that the fracture analysis can be more accurately conducted. One of the major difficulties to apply the cohesive zone model is that the cohesive tractions are related to the crack surface opening displacement in the cohesive zone, so it is very hard to obtain the exact cohesive traction distribution theoretically. Finding a proper way to model the cohesive traction distribution is the biggest challenge for the successful application of the cohesive zone model in our future work.

Reference

[1] B. Harris, *Engineering composite materials [electronic resource] / Bryan Harris*: London : IOM, 1999.2nd ed., 1999.

[2] J. R. Rice, "Mathematical analysis in the mechanics of fracture," *Fracture: An advanced treatise,* vol. 2, pp. 191-311, 1968.

[3] Z. Suo and J. W. Hutchinson, "Interface crack between two elastic layers," *International Journal of Fracture,* vol. 43, pp. 1-18, 1990.

[4] J. W. Hutchinson, M. Mear, and J. R. Rice, "Crack paralleling an interface between dissimilar materials," *Journal of Applied Mechanics,* vol. 54(4), pp 828-832, 1987.

[5] T. Y. Zhang and J. Li, "Interaction of a screw dislocation with an interface crack," *Journal of applied physics,* vol. 70, pp. 744-751, 1991.

[6] J. Qu and Q. Li, "Interfacial dislocation and its applications to interface cracks in anisotropic bimaterials," *Journal of Elasticity,* vol. 26, pp. 169-195, 1991.

[7] D. L. Holt, "Dislocation cell formation in metals," *Journal of applied physics,* vol. 41, pp. 3197-3201, 1970.

[8] Y. Ishida, H. Ishida, K. Kohra, and H. Ichinose, "Determination of the Burgers vector of a dislocation by weak-beam imaging in a HVEM," *Philosophical Magazine A,* vol. 42, pp. 453-462, 1980.

[9] H. Saka, "Burgers vector determination of dislocations in an elastically anisotropic crystal by high-order reflection imaging technique in a HVEM," *Philosophical Magazine A,* vol. 49, pp. 327-339, 1984.

[10] B. A. Bilby, A. H. Cottrell, and K. H. Swinden, "Spread of plastic yield from a notch," *Proceedings of the Royal Society of London Series a-Mathematical and Physical Sciences,* vol. 272, pp. 304-314, 1963.

[11] A. G. Guy and J. J. Hren, *Elements of physical metallurgy / [by] Albert G. Guy and John J. Hren*: Reading, Mass. : Addison-Wesley, [1974] 3d ed.

[12] J. Dundurs, "Elastic interaction of dislocations with inhomogeneities," *Mathematical Theory of Dislocations, ed New York: The American Society of Mechanical Engineers,* pp. 70-115, 1959.

[13] T. L. Anderson, *Fracture mechanics : fundamentals and applications / T.L. Anderson*: Boca Raton, FL : Taylor & Francis, 2005. 3rd ed.

[14] D. A. Hills, *Solution of crack problems : the distributed dislocation technique / by D.A. Hills ... [et al.]*: Dordrecht ; Boston : Kluwer Academic Publishers, 1996.

[15] J. Weertman, *Dislocation based fracture mechanics / Johannes Weertman*: Singapore ; River Edge, N.J. : World Scientific, c1996., 1996.

[16] R. Chao and N. Laws, "Closure of an arc crack in an isotropic homogeneous material due to uniaxial loading," *Quarterly Journal of Mechanics and Applied Mathematics,* vol. 45, pp. 629-640, Nov 1992.

[17] M. Williams, "The stresses around a fault or crack in dissimilar media," *Bulletin of the Seismological Society of America,* vol. 49, pp. 199-204, 1959.

[18] J. R. Rice and G. C. Sih, "Plane Problems of Cracks in Dissimilar Media," *Journal of Applied Mechanics,* vol. 32, pp. 418-423, 1965.

[19] F. Erdogan, "Stress distribution in a nonhomogeneous elastic plane with cracks," *Journal of Applied Mechanics,* vol. 30, pp. 232-236, 1963.

[20] A. England, "A crack between dissimilar media," *Journal of Applied Mechanics,* vol. 32, pp. 400-402, 1965.

[21] D. K. Yi, Z. M. Xiao, and S. K. Tan, "On the fracture behaviour of an interface crack with plastic zone corrections," *Mechanics of Materials,* vol. 64, pp. 128-134, 2013.

[22] M. Comninou, "The interface crack in a shear field," *Journal of Applied Mechanics,* vol. 45, pp. 287-290, 1978.

[23] C. Atkinson, "The interface crack with a contact zone," *international Journal of Fracture,* vol. 19, pp. 131-138, 1982.

[24] A. Gautesen and J. Dundurs, "The interface crack in a tension field," *Journal of Applied Mechanics,* vol. 54, pp. 93-98, 1987.

[25] A. Gautesen and J. Dundurs, "The interface crack under combined loading," *Journal of Applied Mechanics,* vol. 55, pp. 580-586, 1988.

[26] K. P. Herrmann and V. V. Loboda, "On interface crack models with contact zones situated in an anisotropic bimaterial," *Archive of Applied Mechanics,* vol. 69, pp. 317-335, Jun 1999.

[27] Z. Xiao, H. Fan, and Y. Suh, "On the contact zone of a subinterfacial Zener-Stroh crack," *Acta mechanica,* vol. 142, pp. 133-148, 2000.

[28] H. Fan, Y. Sun, and Z. Xiao, "Contact zone in an interfacial Zener–Stroh crack," *Mechanics of materials,* vol. 30, pp. 151-159, 1998.

[29] M. Stippes, H. B. Wilson. Jr., and F. N. Krull, "A contact stress problem for a smooth disk in an infinite plate," *Proceedings of the fourth U. S. Congress of Applied Mechanics, ASME,* vol. 2, pp. 799-806, 1962.

[30] J. H. B. Wilson, "Approximate determination of contact stresses in an Infinite plate With a smooth circular insert," *Developments in Theoretical and Applied Mechanics, Pegamon Press, New York, N. Y.,* vol. 2, pp. 147-163, 1964.

[31] A. H. England, "An arc crack around a circular elastic inclusion," *Journal of Applied Mechanics,* vol. 33, pp. 637-640, 1966.

[32] A. B. Perlman and G. C. Sih, "Elastostatic problems of curvilinear cracks in bonded dissimilar materials," *International Journal of Engineering Science,* vol. 5, pp. 845-867, 1967.

[33] M. Toya, "A crack along the interface of a circular inclusion embedded in an infinite solid," *Journal of the Mechanics and Physics of Solids,* vol. 22, pp. 325-348, 1974.

[34] P. Kelly, D. A. Hills, and D. Nowell, "Curved interface cracks between elasticlly dissimlar media, with application to the analysis of circular

inclusions," *International Journal of Mechanical Sciences,* vol. 36, pp. 173-181, Mar 1994.

[35] E. N. Theotokoglou and E. E. Theotokoglou, "The interface crack along a circular inclusion interacting with a crack in the infinite matrix," *International Journal of Fracture,* vol. 116, pp. 1-23, Jul 2002.

[36] P. B. N. Prasad and K. R. Y. Simha, "Interface crack around circular inclusion: SIF, kinking, debonding energetics," *Engineering Fracture Mechanics,* vol. 70, pp. 285-307, 2003.

[37] L. Gorbatikh, S. Lomov, and I. Verpoest, "Elastic compliance of a partially debonded circular inhomogeneity," *International Journal of Fracture,* vol. 131, pp. 211-229, Feb 2005.

[38] F. Paris, E. Correa, and V. MantiC, "Kinking of Transversal Interface Cracks Between Fiber and Matrix," *Journal of Applied Mechanics,* vol. 74, pp. 703-716, 2007.

[39] V. Mantic, "Interface crack onset at a circular cylindrical inclusion under a remote transverse tension. Application of a coupled stress and energy criterion," *International Journal of Solids and Structures,* vol. 46, pp. 1287-1304, Mar 2009.

[40] V. I. Kushch, S. V. Shmegera, and L. Mishnaevsky, "Elastic interaction of partially debonded circular inclusions. I. Theoretical solution," *International Journal of Solids and Structures,* vol. 47, pp. 1961-1971, Jul 2010.

[41] V. I. Kushch, S. V. Shmegera, and L. Mishnaevsky, "Elastic interaction of partially debonded circular inclusions. II. Application to fibrous composite," *International Journal of Solids and Structures,* vol. 48, pp. 2413-2421, Aug 2011.

[42] O. Tamate, "The effect of a circular inclusion on the stresses around a line crack in a sheet under tension," *International Journal of Fracture Mechanics,* vol. 4, pp. 257-266, 1968.

[43] C. Atkinson, "Interaction between a crack and an inclusion," *International Journal of Engineering Science,* vol. 10, pp. 127-136, 1972.

[44] Sendecky.Gp, "Interaction of cracks with rigid inclusion in longitudinal shear deformation," *International Journal of Fracture,* vol. 10, pp. 45-52, 1974.

[45] D. Marshall, B. N. Cox, and A. G. Evans, "The mechanics of matrix cracking in brittle-matrix fiber composites," *Acta Metallurgica,* vol. 33, pp. 2013-2021, 1985.

[46] D. B. Marshall and B. Cox, "Tensile fracture of brittle matrix composites: influence of fiber strength," *Acta Metallurgica,* vol. 35, pp. 2607-2619, 1987.

[47] D. B. Marshall and A. G. Evans, "Failure Mechanisms in Ceramic‐Fiber/Ceramic‐Matrix Composites," *Journal of the American Ceramic Society,* vol. 68, pp. 225-231, 1985.

[48] D. Marshall and A. Evans, "The tensile strength of uniaxially reinforced

ceramic fiber composites," in *Fracture Mechanics of Ceramics*, ed: Springer, 1986, pp. 1-15.

[49] D. B. Marshall and A. G. Evans, "Application of fracture mechanics to fiber composites," in *Proceedings of the 9th Annual Conference on Composites and Advanced Ceramic Materials: Ceramic Engineering and Science Proceedings, Volume 6, Issue 7/8*, 1985, pp. 537-549.

[50] L. McCartney, "Mechanics of matrix cracking in brittle-matrix fibre-reinforced composites," *Proceedings of the Royal Society of London. A. Mathematical and Physical Sciences,* vol. 409, pp. 329-350, 1987.

[51] B. Budiansky, J. W. Hutchinson, and A. G. Evans, "Matrix fracture in fiber-reinforced ceramics," *Journal of the Mechanics and Physics of Solids,* vol. 34, pp. 167-189, 1986.

[52] J. W. Hutchinson and H. M. Jensen, "Models of fiber debonding and pullout in brittle composites with friction," *Mechanics of materials,* vol. 9, pp. 139-163, 1990.

[53] F. Erdogan, G. D. Gupta, and M. Ratwani, "Interaction between a circular inclusion and an arbitrarily oriented crack," *Journal of Applied Mechanics-Transactions of the Asme,* vol. 41, pp. 1007-1013, 1974.

[54] S. Ogin, P. Smith, and P. Beaumont, "Matrix cracking and stiffness reduction during the fatigue of a GFRP laminate," *Composites Science and Technology,* vol. 22, pp. 23-31, 1985.

[55] S. Tan and R. Nuismer, "A theory for progressive matrix cracking in composite laminates," *Journal of Composite Materials,* vol. 23, pp. 1029-1047, 1989.

[56] I. Kunin and B. Gommerstadt, "On elastic crack-inclusion interaction," *International Journal of Solids and Structures,* vol. 21, pp. 757-766, 1985.

[57] L. Walpole, "A coated inclusion in an elastic medium," in *Mathematical Proceedings of the Cambridge Philosophical Society*, pp. 495-506, 1978.

[58] P. Theocaris and C. Demakos, "The coated inclusion effect on the mode of fracture of encapsulated particulates," *Journal of adhesion science and technology,* vol. 2, pp. 427-448, 1988.

[59] M. Cherkaoui, H. Sabar, and M. Berveiller, "Micromechanical of the coated inclusion problem and application to composite materials," *Journal De Physique Iii,* vol. 4, pp. 719-732, Apr 1994.

[60] Y. Benveniste, G. Dvorak, and T. Chen, "Stress fields in composites with coated inclusions," *Mechanics of Materials,* vol. 7, pp. 305-317, 1989.

[61] T. Chen, G. Dvorak, and Y. Benveniste, "Stress fields in composites reinforced by coated cylindrically orthotropic fibers," *Mechanics of Materials,* vol. 9, pp. 17-32, 1990.

[62] Y. Mikata and M. Taya, "Stress field in a coated continuous fiber composite subjected to thermo-mechanical loadings," *Journal of Composite Materials,* vol. 19, pp. 554-578, 1985.

[63] Z. Xiao and B. Chen, "On the interaction between an edge dislocation and a coated inclusion," *International journal of solids and structures,* vol. 38,

pp. 2533-2548, 2001.

[64] Z. Xiao and B. Chen, "A screw dislocation interacting with a coated fiber," *Mechanics of materials,* vol. 32, pp. 485-494, 2000.

[65] Z. Xiao and B. Chen, "Stress intensity factor for a Griffith crack interacting with a coated inclusion," *International journal of fracture,* vol. 108, pp. 193-205, 2001.

[66] N. Bonfoh, V. Hounkpati, and H. Sabar, "New micromechanical approach of the coated inclusion problem: Exact solution and applications," *Computational Materials Science,* vol. 62, pp. 175-183, Sep 2012.

[67] Y. E. Pak, D. Mishra, and S. H. Yoo, "Closed-form solution for a coated circular inclusion under uniaxial tension," *Acta Mechanica,* vol. 223, pp. 937-951, May 2012.

[68] Z. Hashin and B. W. Rosen, "The elastic moduli of fiber-reinforced materials," *Journal of applied mechanics,* vol. 31, pp. 223-232, 1964.

[69] R. Christensen and K. Lo, "Solutions for effective shear properties in three phase sphere and cylinder models," *Journal of the Mechanics and Physics of Solids,* vol. 27, pp. 315-330, 1979.

[70] H. Luo and G. Weng, "On Eshelby's S-tensor in a three-phase cylindrically concentric solid, and the elastic moduli of fiber-reinforced composites," *Mechanics of Materials,* vol. 8, pp. 77-88, 1989.

[71] H. A. Luo and Y. Chen, "An edge dislocation in a 3-phase composite cylinder model," *Journal of Applied Mechanics-Transactions of the Asme,* vol. 58, pp. 75-86, Mar 1991.

[72] H. A. Luo and Y. Chen, "Matrix cracking in fiber-reinforced composite-materials," *Journal of Applied Mechanics-Transactions of the Asme,* vol. 58, pp. 846-848, Sep 1991.

[73] K. Kim and L. Sudak, "Interaction between a radial matrix crack and a three-phase circular inclusion with imperfect interface in plane elasticity," *International journal of fracture,* vol. 131, pp. 155-172, 2005.

[74] Z. Tong, S. Lo, C. Jiang, and Y. Cheung, "An exact solution for the three-phase thermo-electro-magneto-elastic cylinder model and its application to piezoelectric–magnetic fiber composites," *International Journal of Solids and Structures,* vol. 45, pp. 5205-5219, 2008.

[75] A. L. Kalamkarov, I. V. Andrianov, and G. A. Starushenko, "Three-phase model for a composite material with cylindrical circular inclusions. Part I: Application of the boundary shape perturbation method," *International Journal of Engineering Science,* vol. 78, pp. 154-177, May 2014.

[76] A. L. Kalamkarov, I. V. Andrianov, and G. A. Starushenko, "Three-phase model for a composite material with cylindrical circular inclusions. Part II: Application of Pade approximants," *International Journal of Engineering Science,* vol. 78, pp. 178-191, May 2014.

[77] X. Wang, C. Liu, Z. Tang, and Y. Wang, "Analysis on the process of stress transferring and characterization on the property of "interphase" in three-phase single-fiber composites," *Journal of Reinforced Plastics and*

Composites, vol. 33, pp. 1388-1402, Aug 2014.

[78] A. Cherkaev and G. Dzierzanowski, "Three-phase plane composites of minimal elastic stress energy: High-porosity structures," *International Journal of Solids and Structures*, vol. 50, pp. 4145-4160, Dec 2013.

[79] P. J. Lin, "A three-phase constitutive model for estimating the elastic moduli and the strengths of granular composite materials," *Journal of Mechanics*, vol. 29, pp. 675-683, Dec 2013.

[80] F. Erdogan and G. D. Gupta, "Numerical solution of singular integral equation," *Quarterly of Applied Mathematics*, vol. 29, pp. 525-534, 1972.

[81] S. Krenk, "Use of interpolation polynomial for solutions of singualr integral equations," *Quarterly of Applied Mathematics*, vol. 32, pp. 479-484, 1975.

[82] P. F. Arthur and Blackbur.Ws, "Growh of a crack in antiplane strain in an elastic-plastic material," *International Journal of Engineering Science*, vol. 8, pp. 747-752, 1970.

[83] P. F. Arthur and Blackbur.Ws, "Anti-plain strain around 2 equal collinear cracks and a crack containing dislocations in a non-work hardening elastic-plastic material loaded uniformly at infinity," *International Journal of Engineering Science*, vol. 8, pp. 975-988, 1970 1970.

[84] A. D. Chitaley and McClinto.Fa, "Elastic-plastic mechanics of steady crack growth under anti-plane shear," *Journal of the Mechanics and Physics of Solids*, vol. 19, pp. 147-163, 1971.

[85] C. Shih and R. Asaro, "Elastic-plastic analysis of cracks on bimaterial interfaces: part I—small scale yielding," *Journal of Applied Mechanics*, vol. 55, pp. 299-316, 1988.

[86] C. Shih and R. Asaro, "Elastic-plastic analysis of cracks on bimaterial interfaces: Part II—Structure of small-scale yielding fields," *Journal of Applied Mechanics*, vol. 56, pp. 763-779, 1989.

[87] C. Shih, R. Asaro, and N. O'Dowd, "Elastic-plastic analysis of cracks on bimaterial interfaces: Part III—large-scale yielding," *Journal of Applied Mechanics*, vol. 58, pp. 450-463, 1991.

[88] T. Wang, "Elastic-plastic asymptotic fields for cracks on bimaterial interfaces," *Engineering Fracture Mechanics*, vol. 37, pp. 527-538, 1990.

[89] Z. Zhang, M. Hauge, and C. Thaulow, "Two-parameter characterization of the near-tip stress fields for a bi-material elastic-plastic interface crack," *International Journal of Fracture*, vol. 79, pp. 65-83, 1996.

[90] H. Lee and Y.-J. Kim, "Interfacial crack-tip constraints and J-integrals in plastically mismatched bi-materials," *Engineering Fracture Mechanics*, vol. 68, pp. 1013-1031, 2001.

[91] G. R. Irwin, "Linear fracture mechanics, fracture transition, and fracture control," *Engineering Fracture Mechanics*, vol. 1, pp. 241-257, 1968.

[92] D. S. Dugdale, "Yielding of steel sheets containing slits," *Journal of the Mechanics and Physics of Solids*, vol. 8, pp. 100-104, 1960.

[93] G. I. Barenblatt, "The Mathematical Theory of Equilibrium Cracks in

Brittle Fracture," in *Advances in Applied Mechanics*. vol. Volume 7, T. v. K. G. K. F. H. v. d. D. H.L. Dryden and L. Howarth, Eds., ed: Elsevier, 1962, pp. 55-129.

[94] B. Bilby, A. Cottrell, E. Smith, and K. Swinden, "Plastic yielding from sharp notches," *Proceedings of the Royal Society of London. Series A. Mathematical and Physical Sciences,* vol. 279, pp. 1-9, 1964.

[95] D. J. Hayes and J. G. Williams, "Practical method of determining Dugdale model solutions for cracked bodies of arbitrary shape," *International Journal of Fracture Mechanics,* vol. 8, pp. 239-256, 1972.

[96] Theocari.Ps and E. E. Gdoutos, "Modified Dugdale-Barenblatt model adapted to various fracture configurations in metals," *International Journal of Fracture,* vol. 10, pp. 549-564, 1974 1974.

[97] G. V. Galatenko, "Generalized-model of a Dugdale crack," *Soviet Applied Mechanics,* vol. 25, pp. 260-265, Mar 1989.

[98] X. M. Wang and Y. P. Shen, "The Dugdale crack on bimaterial interface," *International Journal of Fracture,* vol. 59, pp. R25-R32, Jan 1993.

[99] D. J. Unger, "Numerical plane stress elastic-perfectly plastic crack analysis under Tresca yield condition with comparison to Dugdale plastic strip model," *Mechanics Research Communications,* vol. 34, pp. 325-330, Jun 2007.

[100] W. Becker and D. Gross, "About the Dugdale crack under mixed mode loading," *International Journal of Fracture,* vol. 37, pp. 163-170, Jul 1988.

[101] A. A. Wells, "Unstable crackpropagation in metals:cleavage and fast fracture," *Proceedings of the Crack Propagation Symposium,* vol. 1, Paper 84, Cranfiedl, UK, 1961.

[102] F. M. Burdekin and D. E. W. Stone, "The crack opening displacement approach to fracture mechanics in yielding materials (Crack opening displacement approach to fracture mechanics in yielding materials)," *JOURNAL OF STRAIN ANALYSIS,* vol. 1, pp. 145-153, 1966.

[103] T. H. Hao, "An exact solution of a crack on a bimaterial curve interface," *Engineering Fracture Mechanics,* vol. 37, pp. 453-456, 1990 1990.

[104] A. Noe and K. P. Herrmann, "Dynamic crack-propagation in a curved interface," *Zeitschrift Fur Angewandte Mathematik Und Mechanik,* vol. 73, pp. T469-T472, 1993 1993.

[105] H. G. Beom, Y. Y. Earmme, and S. Y. Choi, "Energy-release rate for an arbitrarily curved interface crack," *Mechanics of Materials,* vol. 18, pp. 195-204, Aug 1994.

[106] N. I. Muskhelishvili, *Some basic problems of the mathematical theory of elasticity : fundamental equations, plane theory of elasticity, torsion and bending / by N.I. Muskhelishvili ; translated from the Russian by J.R.M. Radok*: Leyden : Noordhoff International, 1977. 4th ed., corr. and augm.

[107] S. Krenk, "Quadature formulas for singular integral-equations of 1st and 2nd kind," *Quarterly of Applied Mathematics,* vol. 33, pp. 225-232, 1975.

[108] D. H. Chen and S. Nakamichi, "Stress intensity factors for an interface crack along an elliptical inclusion," *International Journal of Fracture*, vol. 82, pp. 131-152, 1996.

[109] C. Zener, "The micro-mechanism of fracture," *Fracturing of Metals, American Society of Metals,Cleveland*, pp. 3-31, 1948.

[110] A. N. Stroh, "The formation of cracks as a result of plastic flow," *Proceedings of the Royal Society of London Series a-Mathematical and Physical Sciences*, vol. 223, pp. 404-414, 1954.

[111] A. Stroh, "The formation of cracks in plastic flow. II," *Proceedings of the Royal Society of London. Series A. Mathematical and Physical Sciences*, vol. 232, pp. 548-560, 1955.

[112] J. Weertman, "Zener–Stroh crack, Zener–Hollomon parameter, and other topics," *Journal of Applied Physics*, vol. 60, pp. 1877-1887, 1986.

[113] H. Fan and Z. Xiao, "A Zener-Stroh crack near an interface," *International journal of solids and structures*, vol. 34, pp. 2829-2842, 1997.

[114] Y. Chen, "Multiple Zener-Stroh crack problem in an infinite plate," *Acta mechanica*, vol. 170, pp. 11-23, 2004.

[115] A. H. Cottrell, "Theory of brittle fracture in steel and similar metals," *Trans. Met. Soc. AIME*, vol. 212, 1958.

[116] S. K. Kikuchi M., Weertman J., "Void nucleation in astrology," *Acta Mechanics*, vol. 29, pp. 1747-1758, 1981.

[117] Z. M. Xiao and B. J. Chen, "Stress analysis for a Zener-Stroh crack interacting with a coated inclusion," *International Journal of Solids and Structures*, vol. 38, pp. 5007-5018, Jul 2001.

[118] H. J. Hoh, Z. M. Xiao, and J. Luo, "On the plastic zone size and CTOD study for a Zener-Stroh crack interacting with a circular inclusion," *Acta Mechanica*, vol. 220, pp. 155-165, Aug 2011.

[119] H. J. Hoh, Z. M. Xiao, and J. Luo, "Crack tip opening displacement of a Dugdale crack in a three-phase cylindrical model composite material," *International Journal of Engineering Science*, vol. 49, pp. 523-535, Jun 2011.

[120] H. Luo, "The stress field due to an edge dislocation and some fracture problems for a three-phase composite cylinder model," Thesis (Ph. D.), Rutgers University, 1989.

[121] M. E. Gurtin and A. I. Murdoch, "A continuum theory of elastic material surfaces," *Archive for Rational Mechanics and Analysis*, vol. 57, pp. 291-323, 1975.

[122] M. E. Gurtin and A. Ian Murdoch, "Surface stress in solids," *International Journal of Solids and Structures*, vol. 14, pp. 431-440, 1978.

[123] M. Gurtin, J. Weissmüller, and F. Larche, "A general theory of curved deformable interfaces in solids at equilibrium," *Philosophical Magazine A*, vol. 78, pp. 1093-1109, 1998.

[124] A. P. Sutton and R. W. Balluffi, "Interfaces in crystalline materials," 1995.

[125] Q. Fang and Y. Liu, "Size-dependent interaction between an edge dislocation and a nanoscale inhomogeneity with interface effects," *Acta materialia*, vol. 54, pp. 4213-4220, 2006.

[126] R. E. Miller and V. B. Shenoy, "Size-dependent elastic properties of nanosized structural elements," *Nanotechnology*, vol. 11, p. 139, 2000.

[127] E. W. Wong, P. E. Sheehan, and C. M. Lieber, "Nanobeam mechanics: Elasticity, strength, and toughness of nanorods and nanotubes," *Science*, vol. 277, pp. 1971-1975, 1997.

[128] L. Zhou and H. Huang, "Are surfaces elastically softer or stiffer?," *Applied Physics Letters*, vol. 84, pp. 1940-1942, 2004.

[129] J. P. Clech, L. M. Keer, and J. L. Lewis, "A model of tension and compression cracks with cohesive zone at a bone-cement interface," *Journal of Biomechanical Engineering-Transactions of the Asme*, vol. 107, pp. 175-182, 1985 1985.

[130] M. Ohnaka and T. Yamashita, "A cohesive zone model for dynamic shear faulting based on experimentally inferred constitutive relation and strong motion source parameters," *Journal of Geophysical Research-Solid Earth and Planets*, vol. 94, pp. 4089-4104, Apr 10 1989.

[131] V. Tvergaard and J. W. Hutchinson, "Effect of strain-dependent cohesive zone model on predictions of crack growth resistance," *International Journal of Solids and Structures*, vol. 33, pp. 3297-3308, Aug 1996.

[132] N. Chandra, H. Li, C. Shet, and H. Ghonem, "Some issues in the application of cohesive zone models for metal-ceramic interfaces," *International Journal of Solids and Structures*, vol. 39, pp. 2827-2855, May 2002.

[133] M. Elices, G. V. Guinea, J. Gomez, and J. Planas, "The cohesive zone model: advantages, limitations and challenges," *Engineering Fracture Mechanics*, vol. 69, pp. 137-163, Jan 2002.

[134] J. Williams and H. Hadavinia, "Analytical solutions for cohesive zone models," *Journal of the Mechanics and Physics of Solids*, vol. 50, pp. 809-825, 2002.

[135] R. M. Christensen, *Mechanics of composite materials / R. M. Christensen*: New York : Wiley, 1979.

Appendix

Appendix A Coefficients for crack-coated inclusion interaction problems

Appendix A1

Const ant a_n, a_n', b_n and b_n' are obtained through the following equations:

$$
\begin{aligned}
&\frac{(1-D)C}{1-C}a_n + b_n = -(1-D)\left(\frac{1}{\beta}\right)^{n+1},\\
&(1-D)a_{-n} - Ab_{-n} = 0,\\
&a_n + (n+1)a_{-n} - B\alpha^{2n+2}b_n - A(n+1)\alpha^2 b_{-n} = 0,\\
&-\frac{(1-D)C}{1-C}(n-1)a_n + \left[\frac{(1-C)D}{1-D} - \frac{1-CD}{1-D}\delta_{n0}\right]a_{-n}\\
&-\left[n-1+(1-M)\delta_{n0}\right]\alpha^2 b_n + \left[1-(1-M)\delta_{n0}\right]\alpha^{-2n+2}b_{-n}\\
&= (1-C)\frac{1}{\beta}(2\beta^2-1)\delta_{n0} + (1-C)\delta_{n1} + (n-1)(C-D)\left(\frac{1}{\beta}\right)^{n+1}\\
&+(n-2)(1-C)\left(\frac{1}{\beta}\right)^{n-1}.
\end{aligned}
\tag{A.1}
$$

And

$$
\begin{aligned}
&\frac{(1-D)C}{1-C}a'_n + b'_n = (1-D)\left(\frac{1}{\beta}\right)^{n+1},\\
&(1-D)a'_{-n} - Ab'_{-n} = 0,\\
&-a'_n + (n+1)a'_{-n} - B\alpha^{2n+2}b'_n - A(n+1)\alpha^2 b'_{-n} = 0,\\
&-\frac{(1-D)C}{1-C}(n-1)a'_n - \left[\frac{(1-C)D}{1-D} - \frac{1-CD}{1-D}\delta_{n0}\right]a'_{-n}\\
&-\left[n-1+(1-M)\delta_{n0}\right]\alpha^2 b'_n - \left[1-(1-M)\delta_{n0}\right]\alpha^{-2n+2}b'_{-n}\\
&= (1-C)\frac{1}{\beta}\delta_{n0} + (1-C)\delta_{n1} - (n-1)(C-D)\left(\frac{1}{\beta}\right)^{n+1} + n(1-C)\left(\frac{1}{\beta}\right)^{n-1}.
\end{aligned}
\tag{A.2}
$$

The definitions of A, B, C, D and M are:

$$A=1-\frac{\beta_2}{\eta_2}, B=1-\beta_2, M=\frac{1-\eta_2}{1+\beta_2-\eta_2},$$
$$C=1-\frac{\beta_1}{\eta_1}, D=1-\beta_1, N=\frac{1-\eta_1}{1+\beta_1-\eta_1}, \quad \text{(A.3)}$$

where

$$\eta_1=\frac{\kappa_3\mu_2+\mu_3}{\kappa_2\mu_3+\mu_2}, \eta_2=\frac{\kappa_2\mu_1+\mu_2}{\kappa_1\mu_2+\mu_1}, \beta_0=\frac{\mu_3(\kappa_2+1)}{\kappa_2\mu_3+\mu_2},$$
$$\beta_1=\frac{\mu_2(\kappa_3+1)}{\kappa_2\mu_3+\mu_2}, \beta_2=\frac{\mu_1(\kappa_2+1)}{\kappa_1\mu_2+\mu_1}, \beta=\frac{\xi}{b}, \alpha=\frac{a}{b}. \quad \text{(A.4)}$$

Appendix A2

The coefficients a_4, b_7 and b_8 in Eqs. (4.16) and (4.17) can be obtained by:

$$\begin{aligned}
&a_1 - a_2 - \left(\frac{b}{a}\right)^2 a_3 = 0,\\
&\frac{\lambda_1+\mu_1}{\lambda_2+\mu_2} a_1 - a_2 + \frac{\mu_2}{\lambda_2+\mu_2}\left(\frac{b}{a}\right)^2 a_3 = 0,\\
&a_2 + a_3 - a_4 = 1,\\
&a_2 - \frac{\mu_2}{\lambda_2+\mu_2} a_3 + \frac{\mu_3}{\lambda_2+\mu_2} a_4 = \frac{\lambda_1+\mu_1}{\lambda_2+\mu_2},
\end{aligned} \tag{A.5}$$

$$\begin{aligned}
&b_1 + (\kappa_1 - 3) b_2 - b_3 - (\kappa_2 - 3)\left(\frac{a}{b}\right)^2 b_4 - \left(\frac{b}{a}\right)^4 b_5 - (\kappa_2 + 1)\left(\frac{b}{a}\right)^2 b_6 = 0,\\
&-b_1 + (\kappa_1 + 3) b_2 + b_3 - (\kappa_2 + 3)\left(\frac{a}{b}\right)^2 b_4 - \left(\frac{b}{a}\right)^4 b_5 + (\kappa_2 - 1)\left(\frac{b}{a}\right)^2 b_6 = 0,\\
&\frac{\mu_1}{\mu_2} b_1 - b_3 + 3\left(\frac{b}{a}\right)^4 b_5 + 4\left(\frac{b}{a}\right)^2 b_6 = 0,\\
&-\frac{\mu_1}{\mu_2} b_1 + 6\frac{\mu_1}{\mu_2} b_2 + b_3 - 6\left(\frac{a}{b}\right)^2 b_4 + 3\left(\frac{b}{a}\right)^4 b_5 + 2\left(\frac{b}{a}\right)^2 b_6 = 0,\\
&b_3 + (\kappa_2 - 3) b_4 + b_5 + (\kappa_2 + 1) b_6 - b_7 - (\kappa_3 + 1) b_8 = 1,\\
&-b_3 + (\kappa_2 + 3) b_4 + b_5 - (\kappa_2 - 1) b_6 - b_7 + (\kappa_1 - 1) b_8 = -1,\\
&\frac{\mu_2}{\mu_3} b_3 - 3\frac{\mu_2}{\mu_3} b_5 - 4\frac{\mu_2}{\mu_3} b_6 + 3b_7 + 4b_8 = 1,\\
&-\frac{\mu_2}{\mu_3} b_3 + 6\frac{\mu_2}{\mu_3} b_4 - 3\frac{\mu_2}{\mu_3} b_5 - 2\frac{\mu_2}{\mu_3} b_6 + 3b_7 + 2b_8 = -1.
\end{aligned} \tag{A.6}$$

where $\lambda_i = \dfrac{2\mu_i \nu_i}{1-2\nu_i}$, $i = 1, 2, 3$ for plane. ν_i is Poisson's ratio for material i. Under plane strain condition, we have $\kappa_i = 3 - 4\nu_i$.

Appendix B The three-phase cylindrical model

The transverse shear modulus μ_{12} is solved from Christens [69, 135]:

$$A'\left(\frac{\mu_{12}}{\mu_2}\right)^2+2B'\left(\frac{\mu_{12}}{\mu_2}\right)+C'=0. \tag{B.1}$$

Here, the coefficients A', B' and C' are given as:

$$\begin{aligned}
A' &= \left[\frac{\mu_1}{\mu_2}\kappa_2+\kappa_2\kappa_1-\left(\frac{\mu_1}{\mu_2}\kappa_2-\kappa_1\right)c^3\right]\left[c\kappa_2\left(\frac{\mu_1}{\mu_2}-1\right)-\left(\frac{\mu_1}{\mu_2}\kappa_2+1\right)\right] \\
&\quad +3c(1-c)^2\left(\frac{\mu_1}{\mu_2}-1\right)\left(\frac{\mu_1}{\mu_2}+\kappa_1\right), \\
B' &= \frac{1}{2}\left[\frac{\mu_1}{\mu_2}\kappa_2+\left(\frac{\mu_1}{\mu_2}\kappa_2-1\right)c+1\right]\left[(\kappa_2-1)\left(\frac{\mu_1}{\mu_2}+\kappa_1\right)-2\left(\frac{\mu_1}{\mu_2}\kappa_2-\kappa_1\right)c^3\right] \\
&\quad +\frac{c}{2}(\kappa_2+1)\left(\frac{\mu_1}{\mu_2}-1\right)\left[\frac{\mu_1}{\mu_2}+\kappa_1+\left(\frac{\mu_1}{\mu_2}\kappa_2-\kappa_1\right)c^3\right]-3c(1-c)^2\left(\frac{\mu_1}{\mu_2}-1\right)\left(\frac{\mu_1}{\mu_2}+\kappa_1\right), \\
C' &= \left[\frac{\mu_1}{\mu_2}\kappa_2+\left(\frac{\mu_1}{\mu_2}\kappa_2-1\right)c+1\right]\left[\frac{\mu_1}{\mu_2}+\kappa_1+\left(\frac{\mu_1}{\mu_2}\kappa_2-\kappa_1\right)c^3\right] \\
&\quad +3c(1-c)^2\left(\frac{\mu_1}{\mu_2}-1\right)\left(\frac{\mu_1}{\mu_2}+\kappa_1\right).
\end{aligned} \tag{B.2}$$

Publication list

1. **Fan, M.**, Yi, D., Xiao, Z., [2014a]. "Elastic-Plastic Fracture Behavior Analysis on a Griffith Crack in the Cylindrical Three-Phase Composites with Generalized Irwin Model". *International Journal of Applied Mechanics* 6.
2. **Fan, M.**, Yi, D., Xiao, Z., [2014b]. "Elastic–plastic stress investigation for an arc-shaped interface crack in composite material". *International Journal of Mechanical Sciences* 83, 104-111.
3. **Fan, M**., Yi, D., Xiao, Z., [2014c]. "Generalized Irwin plastic zone correction for a Griffith crack near a coated-circular inclusion". *International Journal of Damage Mechanics*, 1056789514544229.
4. **Fan, M.**, Yi, D., Xiao, Z., [2014d]. "An interfacial arc-shaped Zener–Stroh crack due to inclusion–matrix debonding in composites". *Acta Mechanica* 225, 909-918.
5. **Fan, M.**, Yi, D., Xiao, Z., [2014e]. "A Zener–Stroh crack in fiber-reinforced composites with generalized Irwin plastic zone correction". *International Journal of Mechanical Sciences* 82, 81-89.
6. **Fan, M.**, Yi, D., Xiao, Z., [2014f]. "A Zener–Stroh crack interacting with a coated inclusion with generalized Irwin plastic zone correction". *International Journal of Solids and Structures* 51, 3399-3409.
7. Yi, D., Xiao, Z., Tan, S., **Fan, M.**, [2014]. "On elastic–plastic fracture behavior of a bi-layered composite plate with a sub-interface crack under mixed mode loading". *Composites Part B: Engineering* 60, 60-73.
8. **Fan, M.**, Yi, D., Xiao, Z., [2014]. "Fracture behavior investigation for a pileup of edge dislocations interacting with a nanoscale inhomogeneity with interface effects". *International Journal of Damage Mechanics 24, 891-914*
9. **Fan, M.**, Yi, D., Xiao, Z., [2014]. "Fracture Behavior Investigation on an Arbitrarily Oriented Sub-interface Zener-Stroh Crack". *Acta Mechanica 226, 1951-1603.*